

**Characterization and engineering of photoreceptors with
improved properties for optogenetic application**



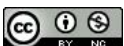
Dissertation zur Erlangung des
naturwissenschaftlichen Doktorgrades
der Julius-Maximilians-Universität Würzburg

vorgelegt von

Shang Yang

From Shandong, China

Würzburg, 2020



Charakterisierung und Entwicklung von Photorezeptoren mit verbesserten Eigenschaften für die optogenetische Anwendung

Eingereicht am:

Mitglieder der Promotionskommission:

Vorsitzender: Prof. Dr. Charlotte Förster

Gutachter: Prof. Dr. Georg Nagel

Gutachter: Prof. Dr. Tobias Langenhan

Tag des Promotionskolloquiums:

Doktorurkunde ausgehändigt am:

Contents	
Summary	1
Zusammenfassung	3
1. Introduction	5
1.1 Optogenetics: a revolutionary biotechnology driven by molecular tools	5
1.2 Light-driven pump rhodopsins	6
1.2.1. Light-driven proton pumps	6
1.2.2 Light-driven chloride pumps	8
1.2.3 Light-driven sodium pumps	11
1.3. Light-gated ion channels	11
1.3.1 Discovery of ChR	11
1.3.2 Molecular architecture of ChR2	13
1.3.3 Photocurrent properties and the photocycle of ChR2	15
1.3.4 Ion selectivity	17
1.3.5 Spectrum properties	17
1.3.6 Perfecting ChRs	18
1.4. Enzymatic photoreceptor toolbox	20
1.4.1 Optogenetic manipulation of cAMP	21
1.4.2 Optogenetic tools for cGMP manipulation	24
1.5 Two-component ion channels for optogenetic activation and inhibition	25
1.6 Strategies for expanding the optogenetic toolbox	27
1.7 Research purpose	28
2 Methods	29
2.1 Chemicals and reagents	29
2.2 Molecular biology	29
2.2.1 DNA cloning	29
2.2.2 Site-directed mutagenesis	30
2.2.3 E. coli transformation	30
2.2.4 Colony PCR	30
2.2.5 Cracking of <i>E. coli</i> cells	30
2.2.6 Plasmids extraction and verification	31
2.2.7 cRNA generation	31
2.3 Oocytes preparation	31
2.4 Microinjection and maintenance of oocytes	32
2.5 Oocytes electrophysiology	32
2.5.1 Two-electrode voltage-clamp (TEVC)	32
2.5.2 Solution used for oocytes electrophysiology	33
2.5.3 Electrodes and capillaries for TEVC	34
2.5.4 Softwares for TEVC	34
2.5.5 Mathematical fitting of the electrophysiology data	34
2.5.6 Light source	34
2.6 cAMP/cGMP ELISA assay from whole oocyte lysates	35
2.7 Oocytes crude membrane protein extracts preparation	35
2.8 Oocyte membrane extract <i>in-vitro</i> reaction	35

2.9 Oocytes crude soluble protein extracts preparation and <i>in-vitro</i> assay	36
2.10 Protein quantification by fluorescence	36
2.11 Fluorescence imaging.....	36
2.12 Experimental design and statistical analysis	36
2.13 Bioinformatics.....	37
3. Results.....	38
3.1 Engineering of high-performance ChR2 variants with altered ion selectivity	38
3.1.1 Template selection for engineering	38
3.1.2 Engineering ChR2 variant with improved Na ⁺ /K ⁺ and Ca ²⁺ conductance.....	39
3.1.3 Generation of ChR2 variant with high photocurrent amplitude and high Na ⁺ /K ⁺ selectivity	41
3.1.4 Generation of high Na ⁺ /K ⁺ and low Ca ²⁺ conducted ChR2 variant.....	44
3.2 Optimized photo-stimulation of <i>NpHR</i> -TYE for long-term inhibition	47
3.2.1 Wavelength-dependent inactivation of <i>NpHR</i> -TYE.....	47
3.2.2 Short-wavelength light rescues <i>NpHR</i> -TYE from inactivation.....	48
3.2.3 Mechanism insight into the inactivation of <i>NpHR</i> -TYE.....	50
3.2.4 Proposed photocycle of <i>NpHR</i>	51
3.2.5 Blue-light induced photo-stimulation of <i>NpHR</i> -TYE enables efficient long-term hyperpolarization and inhibition in brain slices.....	52
3.3 Optogenetic tools for cAMP manipulation	54
3.3.1 Engineering photoactivated adenylyl cyclase for cAMP manipulation.....	54
3.3.2 New photoactivated adenylyl cyclase, biPAC	63
3.3.3 Engineering rhodopsin-adenylyl cyclases (RhAC)	64
3.4. Dual-color bi-directional control of cell activity.....	69
3.4.1 Generation and selection of optogenetic actuator for activation	69
3.4.2 Comparison of light-gated potassium channels.....	71
3.4.3 Selection of the ideal light stimuli.....	72
3.4.4 Implementation of dual-color optogenetics in <i>Xenopus</i> oocytes.....	73
4. Discussions	77
4.1 Discussion for ChR2 project	77
4.1.1 Improved ChR2 variants expand the optogenetic application	77
4.1.2. Structural determinants of the photocurrent properties of ChR2 variants	78
4.1.3 Next step in ChR engineering.....	79
4.2 Discussion for <i>NpHR</i> project.....	81
4.2.1 Biophysical mechanism of <i>NpHR</i> -TYE inactivation and recovery.....	81
4.2.2 Short-wavelength light enables optimized spatiotemporal control of <i>NpHR</i> -TYE.....	82
4.3 Discussion for optogenetic tools for cAMP manipulation project	85
4.3.1 Oocyte-based <i>in-vitro</i> assay allows reliable characterization of PACs.....	85
4.3.2 Molecular mechanism of reducing the dark activity of bPAC.....	85
4.3.3 Dark activity-reduced soluble and membrane-anchored PACs expand the optogenetic application.....	86
4.3.4 N-terminal YFP-tagged RhAC for fast control of cAMP in cell.....	87
4.4 Discussion for dual-color optogenetics project.....	88
4.4.1 Different kinetic properties of vF-Chrimson upon blue and red light stimulation..	88

4.4.2 Two-component system for optogenetic silencing	88
4.4.3 Minimalization of the crosstalk.....	89
5. References:.....	91
6. Appendix.....	101
6.1 List of primers used in this study	101
6.2 Abbreviation.....	104
Acknowledgement	107
Affidavit.....	108
Curriculum Vitae.....	109

Summary

Optogenetics became successful in neuroscience with Channelrhodopsin-2 (ChR2), a light-gated cation channel from the green alga *Chlamydomonas reinhardtii*, as an easy applicable tool. The success of ChR2 inspired the development of various photosensory proteins as powerful actuators for optogenetic manipulation of biological activity. However, the current optogenetic toolbox is still not perfect and further improvements are desirable. In my thesis, I engineered and characterized several different optogenetic tools with new features.

(i) Although ChR2 is the most often used optogenetic actuator, its single-channel conductance and its Ca^{2+} permeability are relatively low. ChR2 variants with increased Ca^{2+} conductance were described recently but a further increase seemed possible. In addition, the H^+ conductance of ChR2 may lead to cellular acidification and unintended pH-related side effects upon prolonged illumination. Through rational design, I developed several improved ChR2 variants with larger photocurrent, higher cation selectivity, and lower H^+ conductance.

(ii) The light-activated inward chloride pump *NpHR* is a widely used optogenetic tool for neural silencing. However, pronounced inactivation upon long time illumination constrains its application for long-lasting neural inhibition. I found that the deprotonation of the Schiff base underlies the inactivation of *NpHR*. Through systematically exploring optimized illumination schemes, I found illumination with blue light alone could profoundly increase the temporal stability of the *NpHR*-mediated photocurrent. A combination of green and violet light eliminates the inactivation effect, similar to blue light, but leading to a higher photocurrent and therefore better light-induced inhibition.

(iii) Photoactivated adenylyl cyclases (PACs) were shown to be useful for light-manipulation of cellular cAMP levels. I developed a convenient *in-vitro* assay for soluble PACs that allows their reliable characterization. Comparison of different PACs revealed that bPAC from *Beggiatoa* is the best optogenetic tool for cAMP manipulation, due to its high efficiency and small size. However, a residual activity of bPAC in the dark is unwanted and the cytosolic localization prevents subcellular precise cAMP manipulation. I therefore introduced point mutations into bPAC to reduce its dark activity. Interestingly, I found that membrane targeting of bPAC with different linkers can remarkably alter its activity, in addition to its localization. Taken together, a set of

PACs with different activity and subcellular localization were engineered for selection based on the intended usage. The membrane-bound PM-bPAC 2.0 with reduced dark activity is well-tolerated by hippocampal neurons and reliably evokes a transient photocurrent, when co-expression with a CNG channel.

(iv) Bidirectional manipulation of cell activity with light of different wavelengths is of great importance in dissecting neural networks in the brain. Selection of optimal tool pairs is the first and most important step for dual-color optogenetics. Through N- and C-terminal modifications, an improved ChR variant (i.e. vf-Chrimson 2.0) was engineered and selected as the red light-controlled actuator for excitation. Detailed comparison of three two-component potassium channels, composed of bPAC and the cAMP-activated potassium channel SthK, revealed the superior properties of SthK-bP. Combining vf-Chrimson 2.0 and improved SthK-bP “SthK(TV418)-bP” could reliably induce depolarization by red light and hyperpolarization by blue light. A residual tiny crosstalk between vf-Chrimson 2.0 and SthK(TV418)-bP, when applying blue light, can be minimized to a negligible level by applying light pulses or simply lowering the blue light intensity.

Zusammenfassung

Die Optogenetik wurde in den Neurowissenschaften mit Channelrhodopsin-2 (ChR2), einem lichtgesteuerten Kationenkanal aus der Grünalge *Chlamydomonas reinhardtii*, als leicht anwendbares Werkzeug erfolgreich. Der Erfolg von ChR2 inspirierte die Entwicklung verschiedener photosensorischer Proteine als leistungsstarke Aktuatoren für die optogenetische Manipulation der biologischen Aktivität. Die derzeitige optogenetische Toolbox ist jedoch immer noch nicht perfekt und weitere Verbesserungen sind wünschenswert. In meiner Arbeit habe ich verschiedene optogenetische Werkzeuge mit neuen Funktionen entwickelt und charakterisiert.

(i) Obwohl ChR2 der am häufigsten verwendete optogenetische Aktuator ist, sind seine Einzelkanal-Leitfähigkeit und seine Ca^{2+} -Permeabilität relativ gering. Kürzlich wurden ChR2-Varianten mit erhöhter Ca^{2+} -Leitfähigkeit beschrieben, eine weitere Verbesserung schien jedoch möglich. Darüber hinaus kann die H^+ -Leitfähigkeit von ChR2 bei längerer Beleuchtung zu einer Ansäuerung der Zellen und zu unbeabsichtigten Nebenwirkungen im Zusammenhang mit dem pH-Wert führen. Durch rationales Design entwickelte ich mehrere verbesserte ChR2-Varianten mit größerem Photostrom, höherer Kationenselektivität und geringerer H^+ -Leitfähigkeit.

(ii) Die lichtaktivierte Chloridpumpe NpHR ist ein weit verbreitetes optogenetisches Werkzeug für die neuronale Inhibierung. Eine ausgeprägte Inaktivierung bei längerer Beleuchtung schränkt jedoch die Anwendung für eine lang anhaltende neuronale Hemmung ein. Ich konnte zeigen, dass die Deprotonierung der Schiffischen Base der Inaktivierung von NpHR zugrunde liegt. Durch die systematische Untersuchung optimierter Beleuchtungsschemata fand ich heraus, dass die Beleuchtung mit blauem Licht allein die zeitliche Stabilität des NpHR-vermittelten Photostroms erheblich verbessern kann. Eine Kombination aus grünem und violetterem Licht eliminiert den Inaktivierungseffekt, ähnlich wie blaues Licht, führt jedoch zu einem höheren Photostrom und deswegen effektiverer Licht-induzierter Inhibierung.

(iii) Photoaktivierte Adenylylcyclasen (PACs) erwiesen sich als nützlich für die Lichtmanipulation der zellulären cAMP-Spiegel. Ich habe einen praktischen *in-vitro*-Test für lösliche PACs entwickelt, der deren zuverlässige Charakterisierung ermöglicht. Ein Vergleich verschiedener PACs ergab, dass bPAC von *Beggiatoa* aufgrund seiner hohen Effizienz und geringen Größe das beste optogenetische Werkzeug für die cAMP-

Manipulation ist. Eine Restaktivität von bPAC im Dunkeln ist jedoch unerwünscht und die cytosolische Lokalisierung verhindert eine subzellulär präzise cAMP-Manipulation. Ich habe daher Punktmutationen in bPAC eingeführt, um dessen Dunkelaktivität zu reduzieren. Interessanterweise fanden Ich heraus, dass das Membrantargeting von bPAC mit verschiedenen „Linkern“ zusätzlich zu seiner Lokalisierung seine Aktivität erheblich verändern kann. Zusammengenommen wurde eine Reihe von PACs mit unterschiedlicher Aktivität und subzellulärer Lokalisation für unterschiedliche Anwendungen konstruiert. Das membrangebundene PM-bPAC 2.0 mit reduzierter Dunkelaktivität wird von Hippocampus-Neuronen gut vertragen und erlaubt, bei gleichzeitiger Expression mit einem CNG-Kanal, zuverlässig einen Licht-induzierten Strom auszulösen.

(iv) Die bidirektionale Manipulation der Zellaktivität mit Licht unterschiedlicher Wellenlänge ist für die Dissektion neuronaler Netze im Gehirn von großer Bedeutung. Die Auswahl der optimalen Werkzeugpaare ist der erste und wichtigste Schritt für die zweifarbige Optogenetik. Durch N- und C-terminale Modifikationen wurde eine verbesserte ChR-Variante (d. h. Vf-Chrimson 2.0) entwickelt und als Rotlicht-gesteuerter Aktuator zur Anregung ausgewählt. Ein detaillierter Vergleich von drei Zweikomponenten-Kaliumkanälen, bestehend aus bPAC und dem cAMP-aktivierten Kaliumkanal SthK, ergab die überlegenen Eigenschaften von SthK-bP. Die Kombination von vf-Chrimson 2.0 und verbessertem SthK-bP „SthK(TV418)-bP“ konnte zuverlässig eine Depolarisation durch rotes Licht und eine Hyperpolarisation durch blaues Licht induzieren. Ein restliches, kleines Übersprechen zwischen vf-Chrimson 2.0 und SthK(TV418)-bP kann beim Anlegen von blauem Licht durch Anlegen von Lichtimpulsen oder durch einfaches Verringern der Intensität von blauem Licht auf ein vernachlässigbares Maß minimiert werden.

1. Introduction

1.1 Optogenetics: a revolutionary biotechnology driven by molecular tools

Optogenetics is a recently emerged biological technique that combines genetic engineering of light sensitive protein into the targeted host cells and light stimulation for manipulation of the targeted cell activity [1]. The beauty of optogenetics is not just for its revolutionizing role in neuroscience research, but also as a vivid example of transformative biotechnology that grows out of interdisciplinary basic research of microbial rhodopsin, including photobiology, photochemistry and photophysics [2]. Despite originated from the neuroscience field, the impacts of optogenetics have already been far beyond the scope of neuroscience and extended into a variety of biological fields, such as cellular signaling study and cardiovascular study.

The concept of optogenetics firstly appeared in 2006 [1]. However, the idea of using light to control cell activity is not new. In 1979, Nobel laureate Francis Crick proposed the need of a tool in neural research for selectively control of only one specific neuron type while leaving others unaltered [3]. In 1999, he further foresaw using light to control cell activity, writing “*One of the next requirements is to be able to turn the firing of one or more types of neuron on or off in the alert animal in a rapid manner. The ideal signal would be light, probably at an infrared wavelength to allow the light to penetrate far enough. This seems rather far-fetched but it is conceivable that molecular biologists could engineer a particular cell type to be sensitive to light in this way.*” [4]. However, at that time no knowledge or techniques are available to make neurons light-sensitive. Clearly, as a stimulus, light has unique advantages for cell activity manipulation: non-invasive, high spatiotemporal resolution etc. Pioneering efforts in making neurons respond to light starts in 2002. Miesenböck’s group described that co-expression of three proteins allows one to control specific neuronal populations by light [5]. In 2004, a chemical optogenetic approach is invented to silence neurons [6]. In addition, manipulation of animal behavior via optogenetic activation of specific neuronal circuits was also firstly reported by in 2005 [7]. However, these approaches are relatively tricky and difficult to handle.

Discovery of Channelrhodopsins (ChRs), especially ChR2 [8, 9] remarks the true

transformation in this field. In the seminal paper of ChR2 [9], Nagel et al. showed large light-induced membrane depolarization in *Xenopus* oocytes and human embryonic kidney 293 (HEK293) cells after expression of ChR2, and proposed that ChR2 could be used as a powerful tool to depolarize animal cells by light illumination. Following this suggestion, a serial of landmarking papers appears in 2005 and 2006, in which, ChR2 was expressed in various host systems, like hippocampal neurons [10], PC12 cells [11], intact vertebrate spinal cords [12], mice retina [13], as well as living animals *Caenorhabditis elegans* [14] and *Drosophila* larvae [15]. The usage of ChR2 spreads rapidly throughout neuroscience and other fields for its simplicity, efficiency, and ease of use. The success of ChR2 as a depolarization tool further encouraged neuroscientists to test chloride pump, halorhodopsin (HR) for hyperpolarization of membrane potential [16, 17]. Aside from neural control, optical control of well-defined biochemical events was also achieved by introducing natural or engineered photoreceptors as optogenetic actuators, such as photoactivated adenylyl cyclases (PAC) [18] and optoXRs [19]. To conclude, efforts in mining and engineering of novel photoreceptors as optogenetic tools continuously drive the development of optogenetics.

In turn, the success of optogenetics also boosted the interest of photoreceptors study. Identification and mechanism study of novel photoreceptors will not just deepen the understanding of their functions in photobiology, but also benefits the optogenetic tools engineering. In the following, I will give brief introductions about some optogenetic tools, mainly focusing on the ionotropic photoreceptors and enzymatic photoreceptors.

1.2 Light-driven pump rhodopsins

1.2.1. Light-driven proton pumps

Bacteriorhodopsin (BR) was first identified in the purple membrane of *Halobacterium salinarum* by Oesterhelt et al. in 1971 [20] and later was proven to be a light-driven unidirectionally outward proton pump [21]. In *Halobacterium salinarum*, BR pumps protons out of the cell after light irradiation, creating a transmembrane (TM) proton gradient, which could serve as the force for ATP synthesis or be coupled to other

transport processes [22, 23]. Extensive biophysical and structural studies of BR have revealed its ion transport mechanism in great detail, making BR a paradigm for membrane transporters. Like all microbial rhodopsins, the *all-trans* retinal (ATR) molecule is covalently bound to a conserved lysine (K216 in BR) via a Schiff base on the last TM helix. At rest state, the Schiff base is protonated and stabilized by ionized counterion residue D85 (Fig. 1.1A). Light illumination converts ATR into *13-cis* configuration at ultrafast speed and leads to the formation of J₆₂₅ and K₅₉₀ intermediates. Then the K₅₉₀ will be transformed to the L₅₅₀ intermediate within 2 μs. After several microseconds, M₄₁₀ will be reached. Importantly, this step involves the transfer of a proton from the Schiff base to D85 in the extracellular part (early M₄₁₀). Then one proton is released into periplasm from E194/E204 complex (late M₄₁₀) (Fig. 1.1A-B). To ensure vectorial proton transport, the reprotonation of Schiff base must occur at cytoplasm. This accessibility switch occurs at M₄₁₀: early M₄₁₀ towards the extracellular side and late M₄₁₀ towards the cytoplasmic side. Transient deprotonation of D96 moves its proton to Schiff base and then receives a new proton from the intracellular side (N₅₆₀). Thermal isomerization of retinal from *13-cis* to *all-trans* leads to the formation of O₆₄₀ state. Following proton transfer from protonated D85 to extracellular E194/E204 cluster completes the photocycle and restores BR to the initial state (Fig. 1.1A-B) [24].

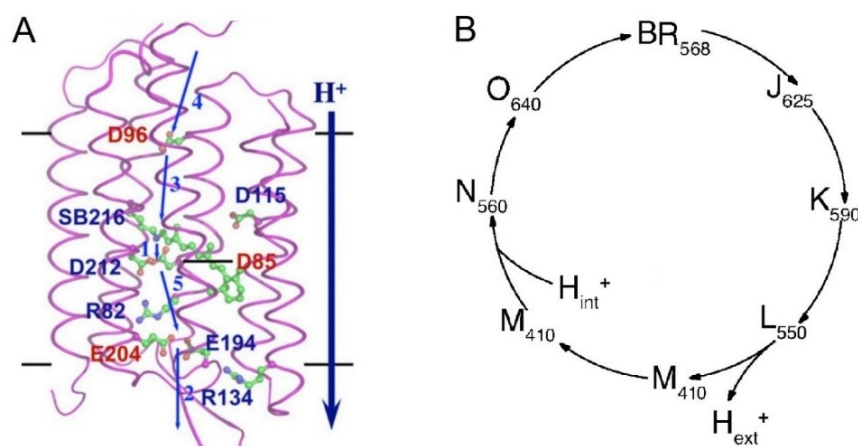


Figure 1.1 Proton transport mechanism of BR.

(A) Scheme of proton transport in BR. Blue numbered arrows indicate the sequence of the proton transfer step. (B) Photocycle of BR. Light illumination starts the photocycle containing a sequential intermediates J, K, L, M, N, and O with different absorbances. Proton release and uptake are indicated in the branched arrow. Modified from [24, 25].

BR as an outward proton pump, in principle, could be used as an optogenetic

actuator for hyperpolarization. As early in 1995, Nagel et al. firstly heterogenous expressed BR in *Xenopus* oocyte and demonstrated light-induced membrane currents. This, as a matter of fact, could be regarded as the beginning of optogenetics [26]. However, the small photocurrent amplitude of BR severely restricted its application. Later discovered high-performance proton pump archaerhodopsin-3 (Arch) from the archaeon *Halorubrum sodomense* is now widely used for the silencing of neural activity [27].

1.2.2 Light-driven chloride pumps

After a couple of years after the discovery of BR, a new rhodopsin was identified in a *Halobacterium salinarum* strain lacking BR and subsequently named Halorhodopsin (*HsHR*) [28, 29]. In the beginning, HR was described as a sodium pump but was later proven to be an inward-directed chloride pump, with the undisputedly proof from *in-vitro* reconstituted HR-containing black lipid membranes assay from Bamberg and colleagues [30-33]. Later discovered HR from an alkalophilic bacterium *Natronomonas pharaonic* (*NpHR*) [34, 35] displays superior properties in comparison with *HsHR*. *NpHR* is easy to express and purify. More importantly, *NpHR* shows much better photostability than *HsHR* upon light illumination [16], which makes *NpHR* one of the most popular neural inhibition tools in optogenetics. In the following, I will introduce the functional and structural characteristics of *NpHR*.

1.2.2.1 Structure of *NpHR*

Although *NpHR* shares 65.7% amino acid (aa) sequence identity with *HsHR* [36, 37] and exhibits superior properties in expression and purification. The crystal structure of *NpHR* was solved 10 years later than the first high-resolution *HsHR* structure [38, 39]. *NpHR* shows typical 7 TM architecture with ATR bound to the conserved lysine residue at the 7th TM helix (Fig. 1.2A). Besides the 7 TM helices, a unique short helix A' locates at the N-terminal and forms a hydrophobic cap together with the helices B and C for separation of the active site and extracellular medium. In the retinal binding site, the Schiff base interacts with D252 and forms the primary binding site for chloride ions with the help of two polar groups of T126 and S130 (Fig. 1.2B). How light drives

chloride transport in *NpHR* will be detailed in the following.

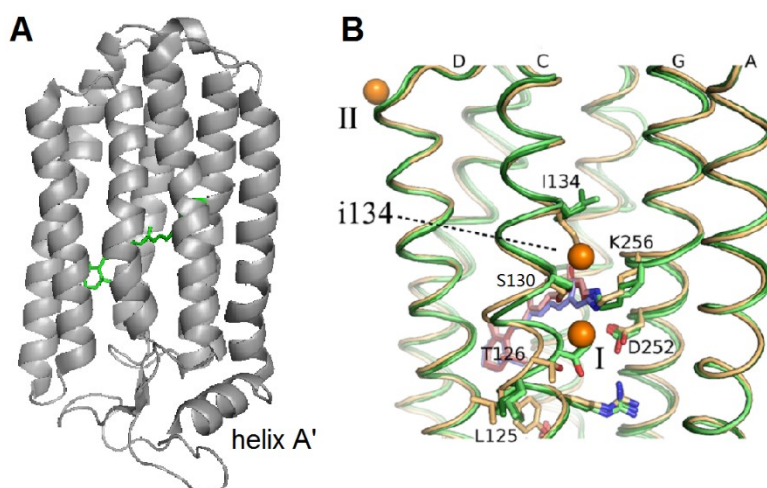


Figure 1.2. Structure and substrate binding site of *NpHR*.

(A) Overall structure of *NpHR* (grey) with highlighted N-terminal short helix A' (grey) and retinal chromophore (green), modified from PDB 3A7K [39]. (B) Br⁻ binding sites in *NpHR*, adapted from [40]. Structures are shown in the superimposed form of resting (yellow, subunit B), N (light yellow, subunit B) and O state (dark green, subunit C) of *NpHR* structure (PDB 4QRY) [41]. Br⁻ is bound at Site I near to T126 at resting state. Rotation of T126 and I134 moves Br⁻ to transient binding site i134 in L² and N state. O state shows similar structure with N state, but Br⁻ ion is bound at binding site II.

1.2.2.2 Photocycle and chloride pump mechanism of *NpHR*

Extensive photocycle studies and structural determinations of photo-intermediates of *NpHR* led to well understanding of the chloride transport mechanism of *NpHR*. At resting state, a chloride ion is bound to the primary binding site (site I) of *NpHR* near the Schiff base (Fig. 1.2B & 1.3B). Light illumination triggers a photocycle involving spectroscopically distinguishable intermediates starting with isomerization of retinal from *all-trans* to *13-cis* form. Chloride ion translocation from binding site I to binding site II occurs at the decay from L² to L³ (also named as N in 4QRY). Simultaneously, inward movement of helix C causes shrinkage of chloride binding site I, and then forms a cytoplasmic interhelical channel with the help of deform of helix F (Fig. 1.3A-B). Chloride ion is subsequently released to the cytoplasm during the transition of L³ to O state. From O state, reisomerization of retinal will close the intracellular space and open the extracellular channel and re-uptake the chloride ion. The following thermal relaxation fully recovers *NpHR* to ground state through the last intermediate *NpHR*'. Under continuous light illumination condition, this step and the transition from ground state to K state could be bypassed (Fig. 1.3A) [42, 43]. The accelerated turnover rate

through the “bypass” photocycle enables relative high photocurrent amplitude of *NpHR* under continuous illumination, in turn, makes *NpHR* the first optogenetic silencer.

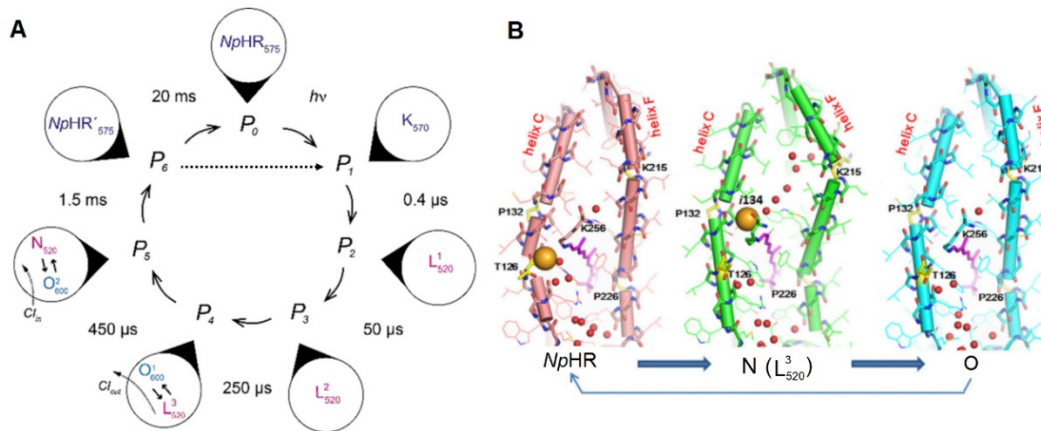


Figure 1.3. Photocycle and intermediates of *NpHR*.

(A) Photocycle of *NpHR* with kinetic properties. Straight dash line with arrow indicates “bypass” photocycle under continuous light illumination. Modified from [40]. (B) Structures of photo-intermediates of *NpHR*, modified from [41].

1.2.2.3 Modifying *NpHR* for improved neural silencing

To effectively inhibit neuron firing, *NpHR* is required to be highly expressed in the target cell. However, the original version of *NpHR* forms toxic aggregates accumulated in the endoplasmic reticulum (ER) when the expression level is high. To overcome this subcellular localization problem, an ER export signal peptide (E) was grafted to the *NpHR* sequence. The modified *NpHR* (called *eNpHR2.0*) displays increased peak photocurrent and eliminated aggregations [44, 45]. Nevertheless, *eNpHR2.0* still fails to counter strong excitation of neurons. Further modification by addition of the C-terminal trafficking signal (T) from the potassium ion channel Kir2.1 generated *NpHR-TYE* (alternative name: *eNpHR3.0*). This modified version showed tremendous increased plasma membrane targeting efficiency and substantially enhanced inhibitory capacity [46], rendering *NpHR-TYE* one of the most popular neural inhibitory tools. However, a decline in photocurrents (referred as inactivation) during continuous illumination at seconds time-scale constrains its efficiency for sustained silencing. Here in this thesis, I investigated the inactivation of *NpHR-TYE* and provided optimized photo-stimulation protocols that enable prolonged suppression of action potential (AP) on a time-scale of minutes.

1.2.3 Light-driven sodium pumps

For more than 40 years after the discovery of BR, no light-driven non-proton cation pump was reported. This absence seems to be reasonable from the chemical point of view. Almost all microbial rhodopsins are covalently bound to ATR via the protonated Schiff base in the resting state. The positive charge of the Schiff base exists on the ion conductive pathway and prevents cation transport. For proton pumps, the Schiff base proton itself works as the substrate. However, for other cations, electrostatic repulsion from the protonated Schiff base inhibits the transport. Till 2013, Inoue et al. reported the first sodium pump KR2 from the marine flavobacterium *Krokinobacter eikastus* [47]. Structural analysis of KR2 revealed two slightly different Na⁺-pumping mechanisms. But they both proposed that the proton of the Schiff base could be transiently sequestered by D116, generating neutralized Schiff base in the M state to allow the transport of Na⁺ [48-50]. Like HR or Arch, KR2 is also expected to function as an inhibitory optogenetic actuator. However, poor plasma membrane targeting constrains its application. Through N- and C- terminal modification, Grimm et al. reported enhanced KR2 (eKR2), which shows enhanced membrane targeting and higher photocurrents, as well as improved performance in silencing neuronal activity in cultured mouse hippocampal neurons [51].

1.3. Light-gated ion channels

1.3.1 Discovery of ChR

Although ChR2 is the first introduced optogenetic tool in the microbial rhodopsins. Its discovery is decades later than BR and HR. The discovery of ChR is from the study of the swimming behavior of green algae and biophysical investigation of microbial rhodopsin. Starting from the 1980s, Kenneth Foster firstly postulated that the photoreceptor for phototactic movement of green algae is rhodopsin by re-analyzing published action spectra [52, 53]. Importantly, Foster provided the first experimental evidence of his argument by restoring phototaxis in “blind” *Chlamydomonas* cells through addition of retinal [54]. Later on, Hegemann’s group reported the photocurrent and action spectrum from cell wall deficient *Chlamydomonas* and showed that this photoreceptor is also responsible for phototaxis and phobic behaviors. The extremely

fast rise of photocurrent suggested the ion channel and the rhodopsin are either intimately linked or within one single protein [55, 56]. Large-scale EST sequencing of *Chlamydomonas reinhardtii* finally uncovered the nucleotide sequence of the rhodopsins now called ChR1 and ChR2, which were independently reported by the groups of Hegemann, Spudich and Takahashi [57, 58]. However, biochemical purification of these photoreceptors turned out to be difficult. In 2002 and 2003, functional expressions and characterizations of ChR1 and ChR2 were finally achieved in *Xenopus* oocytes by Nagel et al. [8, 9]. These experiments revealed a completely new class of rhodopsins with no “pump” activity but functioned as a “channel” (Fig. 1.4A-C). More importantly, functional expression of ChR2 in *Xenopus* oocytes and HEK293 cells showed tens of millivolts membrane potential depolarization upon light stimulation, suggesting that ChR2 could be a powerful tool to depolarize the cell membrane (Fig. 1.4D) [9]. This remarkable protein paved the way for optogenetic manipulation of cell activity. Inspired by its success, considerable efforts were drawn into engineering and identification of new tools for optogenetic application. In the following, the molecular architecture, the photocurrent propriety, the photocycle, the ion selectivity, the spectrum properties as well as the engineering efforts of ChRs will be detailed.

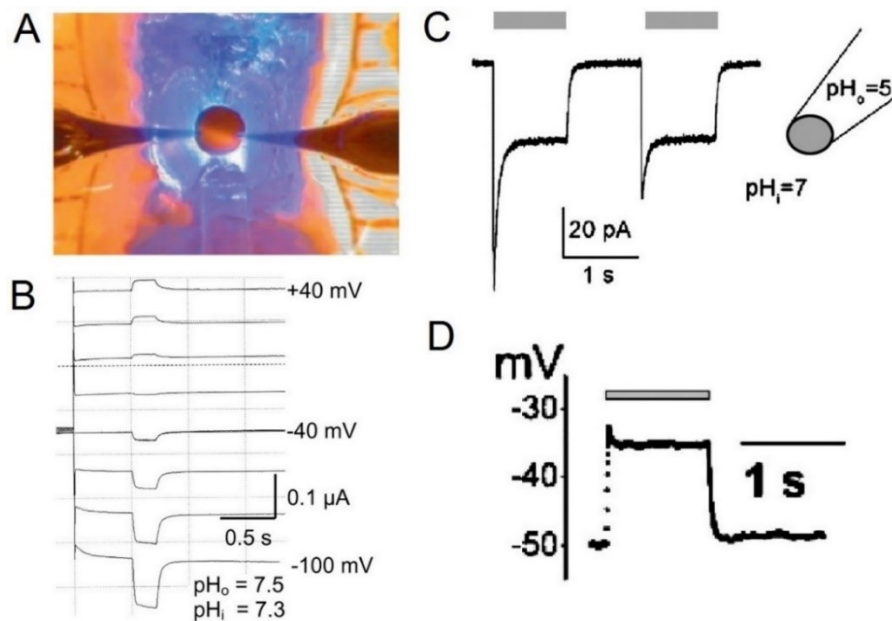


Figure 1.4. Functional discovery of ChRs.

(A) Electrophysiological recording from oocytes expressing ChRs for studying light-induced

current. (B) Bidirectional photocurrents of ChR1 under potential from -100 mV to $+40$ mV indicate the channel function of ChR1. (C) Light-induced currents from ChR2. (D) Blue light induced depolarization of ChR2 expressing HEK293 cell. Taken from [8, 9, 59].

1.3.2 Molecular architecture of ChR2

Full-length ChR2 consists of a 7 TM helices domain that forms ion channel and a long C-terminal cytosolic domain with unknown function. Truncation of the cytosol extension doesn't affect the channel function of ChR2 [9]. To make it trackable in optogenetic application, a fluorescent protein is normally fused at the C-terminal of the channel without affecting the protein function. Seeing is believing. The first structural information of ChR2 was obtained by a low-resolution (6 Å) projection map of cryogenic electron microscopy (cryo-EM) of two-dimensional crystals, from which, a dimerized form of ChR2 could be observed [60]. In 2012, Kato et al. solved the first high resolution (2.3 Å) crystal structure of the chimera protein C1C2, consisting of the first five TM helices of ChR1 and the last two TM helices from ChR2 [61]. This chimera structure reveals, for the first time, the fundamentals of ChRs architecture: the very hydrophobic retinal-binding pocket and cation conduction pathway formed by TM helices 1, 2, 3, and 7 within a monomer molecule. This structure greatly advanced the understanding of the mechanism of ChR2 and fostered the molecular design of ChRs. However, C1C2 and ChR2 show certain differences regarding channel properties [62]. As ChR2 and its derivatives are the most popular tools in optogenetics, a native structure of ChR2 is of great importance in revealing its functional mechanism and in guiding molecular engineering. In 2017, the structures of wild-type (wt) ChR2 and ChR2-C128T were reported by Volkov et al. [63]. Indeed, considerable differences in structure geometry were observed between ChR2 and C1C2, including hydrogen-bond patterns, intra- and interhelical interactions as well as residue conformations (Fig. 1.5). The most predominant difference is the molecular gates: three (intracellular, central and extracellular) gates were identified in ChR2, whereas C1C2 only contains two gates. Another significant difference is the "DC" pair in two molecules. A water molecule is found in the "DC" (D156-C128) pair of ChR2, but absent in that of C1C2 (Fig. 1.5).

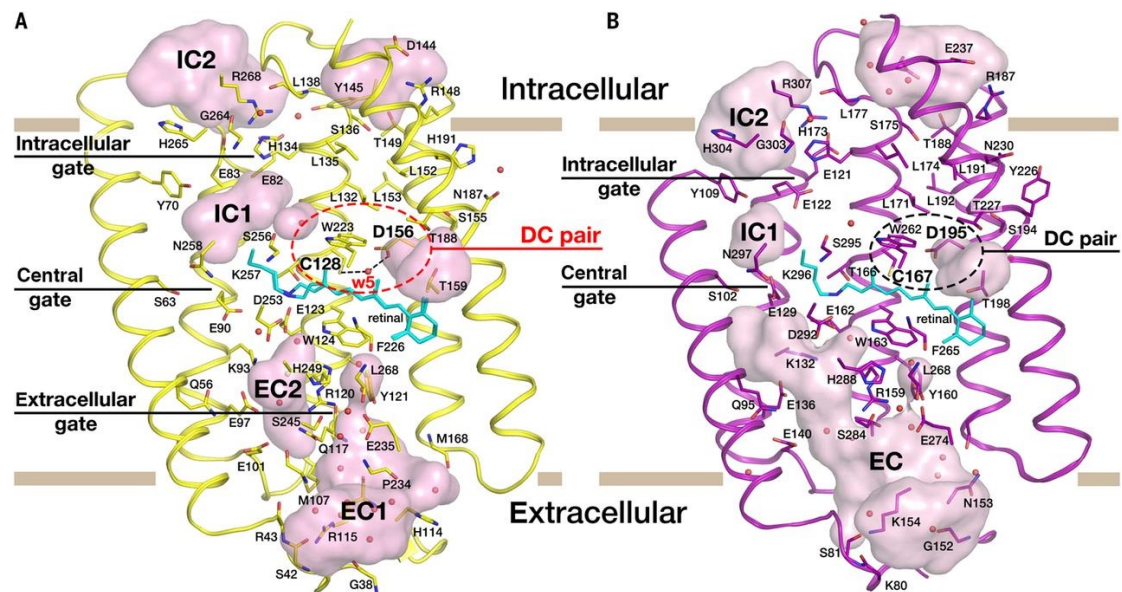


Figure 1.5 Crystal structure of ChR2 (A) and C1C2 (B).

Channel cavities and gates of wt-ChR2 and C1C2 were highlighted. Wt-ChR2 contains three (intracellular, central and extracellular) gates (A), while only two gates in C1C2 (B). DC pairs are shown in red and black ellipse for ChR2 (A) and C1C2 (B), respectively. The gray lines indicate the hydrophobic membrane core boundaries. abbreviations for the aa residues used here are the single-letter form. The retinal molecule is shown in cyan. Taken from [63].

In ChR2, the retinal chromophore is covalently bound to a conserved lysine residue at the 7th helix (K257) via a protonated Schiff base (Fig. 1.5A & 1.6A). The protonated Schiff base directly contacts with its counterion complex E123 and D253. Moreover, the Schiff base, D253 and E90 form the central gate together with residues S63 and N258 (Fig. 1.6 A). Along with water molecules, extensive hydrogen networks are formed (Figure 1.6A). Notably, water molecules w2, w3 and w4 build up the interactions between the protonated Schiff base counterions complex with Q117, R120 and W124 which are involved in the constitution of the extracellular gate of ChR2. Therefore, retinal isomerization could directly trigger rearrangements of the hydrogen-bonded networks stabilizing the extracellular gates and central gates, resulting in simultaneously opening of the extracellular gates and central gates. Meanwhile, this hydrogen network re-arrangement further re-orientates helix 2 via its inter-helical hydrogen-bond connection. Additional changes of helices 6 and 7 induced by retinal isomerization jointly open the intracellular gate with the re-orientated helix 2. Collectively, extensive interactions network between three gates ensures reliably relay

of the light-induced change from the retinal binding pocket and synchronically opens three gates [63]. In addition, the “DC” pair near the Schiff base in ChR2, despite not positioned in the putative ion pore, also has a strong effect on the open channel lifetime and photocurrent properties [46, 64-68].

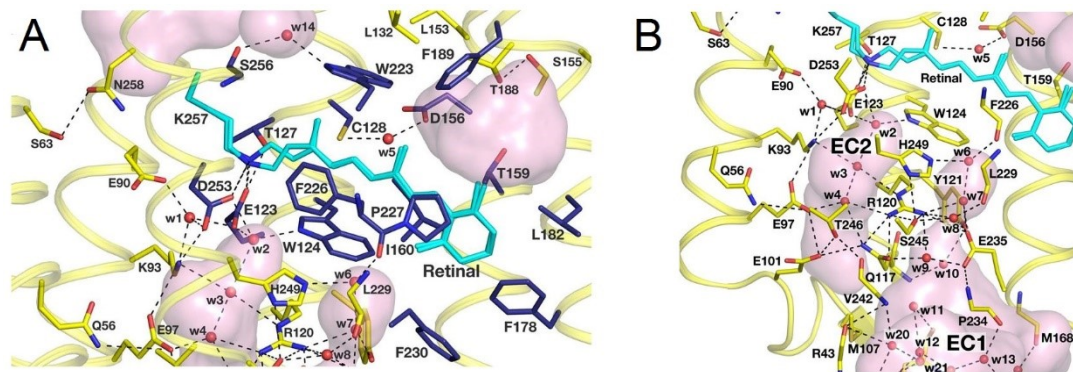


Figure 1.6 Retinal binding pocket of ChR2 (A) and its interaction with extracellular gate (B). The retinal molecule is shown in cyan. Residues that involves the formation of retinal binding pocket are shown in dark blue. The extracellular gate of ChR2 comprises M107, Q117, Y121, W124, S245, H249, and R120 (B). Taken from [63].

1.3.3 Photocurrent properties and the photocycle of ChR2

Upon light stimulation, the initial peak current (I_p) of ChR2 fast decays to a lower stationary level (I_s), which is referred as inactivation (or desensitization, Fig. 1.7A). A second pulse after a certain time delay generates a smaller I_p , but unchanged I_s (light adaptation, Fig. 1.7A). This initial I_p can be recovered only after many seconds in darkness (dark adaptation) [9]. In addition, photocurrents recording of ChR2 showed typical inward rectification (Fig. 1.7B). Near the reversal potential, I_p and I_s displayed different cation flow directions (Fig. 1.7B). This difference in reversal potential of I_p and I_s indicates different cation selectivity of I_p and I_s [69]. Several photocycle models have been proposed to explain the inactivation, the light adaptation and the ion selectivity alteration of ChR2 [9, 70-72]. However, these models failed to explain the controversies between recording from single-turnover experiments and under continuous illumination. Until very recently, a unifying photocycle of ChR2 is proposed based on results from single-turnover electrophysiology, time-resolved step-scan FTIR and Raman spectroscopy of fully dark-adapted ChR2 [73]. This model consists of two closed states (C_1 and C_2) and two open states (O_1 and O_2) distributed in two photocycle pathways (Fig. 1.7C). For fully dark-adapted ChR2, the retinal chromophore almost

100% exists in all-*trans*, C=N-*anti* form (C_1). Upon light illumination, two photocycle pathways are initiated. For the *anti*-cycle (retinal in 13-*cis*, C=N-*anti* form), classic K, M and N intermediates are sequentially generated. The M intermediate is divided into two subsequent steps with the same absorbance. The late M state is assigned as $O_{1\text{-early}}$ with almost exclusive proton conductance. While N intermediate which absorbs at 520 nm, is also carried by cations ($O_{1\text{-late}}$). In the other pathway, high frequencies light flash or continuous illumination directly converts initial D_{470} to nonconducting accumulative P_{480} (C_2) with deprotonated E90, which remains deprotonated during the whole photocycle. The photoproduct of P_{480} is the relative long-lived conducting O_2 state, which is highly selective for proton and shows lower conductance than O_1 . Due to its relatively long decay time, O_2 tends to accumulate during continuous illumination. This *syn*-cycle explains the inactivation of ChR2 and the relative high proton selectivity for the steady photocurrent [73]. The light-adapted ChR2 represents a mixture of C_1 and C_2 . While the dark adaptation process means fully restoring all the photo-intermediates to the initial C_1 state.

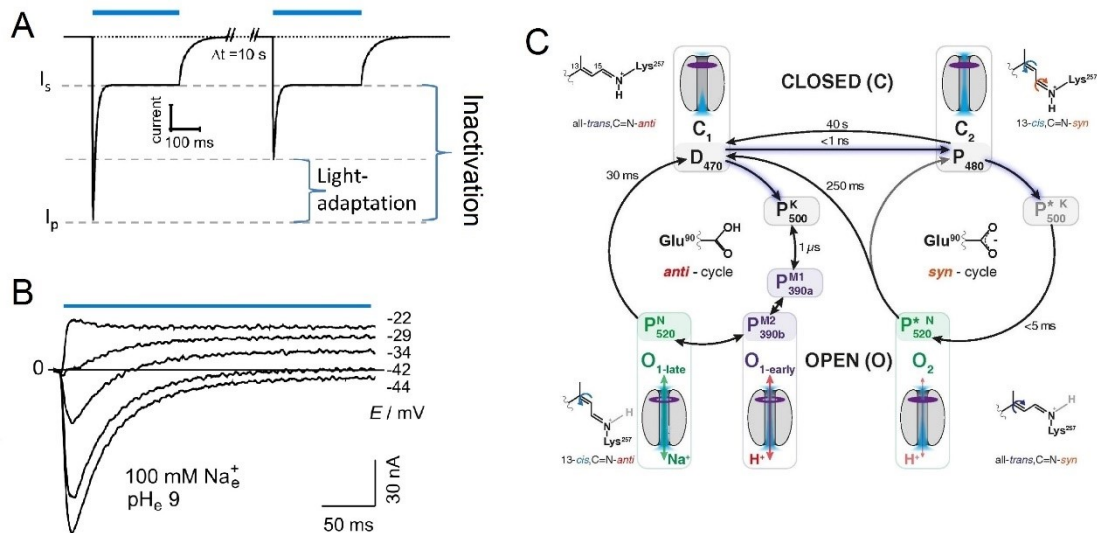


Figure 1.7 Photocurrent properties and photocycle model of ChR2

(A) ChR2 exhibits a fast decline from initial I_p to I_s , naming inactivation. After a certain time delay (Δt), a second light pulse induces smaller I_p but unchanged I_s , which is referred as light adaption. Modified from [74]. (B) Photocurrent records of ChR2 in *Xenopus* oocytes at different holding voltages in the extracellular solution with 100 mM Na_e^+ , pH 9. When holding at -34 mV, the I_p and I_s showed different ion influx directions. Modified from [75]. (C) Photocycle of ChR2. D_{470} and P_{480} represent the closed states C_1 and C_2 . Light illumination triggers the retinal isomerized into either 13-*cis*, C=N *anti* or 13-*cis*, C=N *syn* form. High conducting O_1 state is generated in the *anti*-cycle,

while low conducting O_2 is from the *syn*-cycle E90 remains protonated during the *anti*-cycle and deprotonated during the *syn*-cycle. Taken from [73].

1.3.4 Ion selectivity

Besides the three gates in the putative cation permeable pathway, no signature ion selective filter was found in ChR2 (Fig. 1.5A). Lacking the selective filter perfectly underlies the non-selective properties of ChR2. ChR2 shows the highest conductance for H^+ , while other monovalent (like Li^+ , Na^+ , K^+) and divalent (like Ca^{2+}) cations are also permeable for ChR2 [9]. The conductance of ChR2 for different cations displays a strong inverse relationship with the size of the cation, i.e. smaller atomic radius ion has higher permeability [9]. Moreover, all the cations are competing with each other for binding and transport in a voltage- and pH-dependent manner [76]. As discussed above, different photo-intermediates of ChR2 also exhibit altered ion selectivity [75]. Under physiological condition, ChR2-mediated photocurrents are mainly carried by H^+ and Na^+ [76]. The H^+ conductance of ChR2 may lead to cellular acidification upon prolonged illumination. To overcome this potential side effect and study the ion-selective mechanism, numerous amino acid substitutions were conducted and identified several key residues that influence the ion selectivity [68, 77-84] (see details in Table 1.1). Here in this thesis, further efforts were applied to modify the ion selectivity of ChR2. Beyond ChR2, other ChRs with altered ion selectivity were also discovered, such as high H^+ selected Chrimson [85, 86] or high Na^+ conducted *PsChR* [87].

1.3.5 Spectrum properties

Although all the ChRs share the same chromophore, their absorbance and action spectrums exhibit extremely wide range. The maximum action spectrum spans from 436 nm to 590 nm [69, 88]. Still, all ChRs retain robust responsivity in the blue light range (Fig. 1.8). The first discovered ChR1 and ChR2 are peaking activated at around 486 and 460 nm [8, 9]. *PsChR* and *TsChR* exhibit slightly blue-shifted spectrum [85, 87]. vChR1 from is the first identified ChR with substantially red-shifted spectrum. However, its photocurrent is small [89]. Chimerization with ChR1 fragments produced C1V1 enables the first red light induces spiking [90]. Later engineered and discovered ensemble of orange- and red-light activated ChRs including ReaChR and Chrimson

empower ChRs for intact tissue activation [85, 91]. Among these bathochromically shifted ChRs, Chrimson shows the most red-shifted action spectrum with peaking at 590 nm. Structural analysis revealed the determinants of the red-shifted absorption of Chrimson: (1) the unique protonation state of the counterion residues, (2) the highly biased distribution of the polar residues toward the β -ionone ring and (3) the structural rigidity of the retinal binding pocket [88]. Rational introducing point mutation S169A could further red-shift the spectrum of Chrimson, but unfortunately at the cost of largely reduced photocurrent amplitude [88]. Besides one-photon excitation, engineered C1V1 variants bearing two additional mutants (E122T/E162T) confers improved two-photon excitability [92], greatly broadening the utility of ChRs for *in-vivo* application. In addition, engineered upconversion nanoparticles that absorb near-infrared light and emit wavelength-specific visible light provided alternative ways for the *in-vivo* application of ChRs [93].

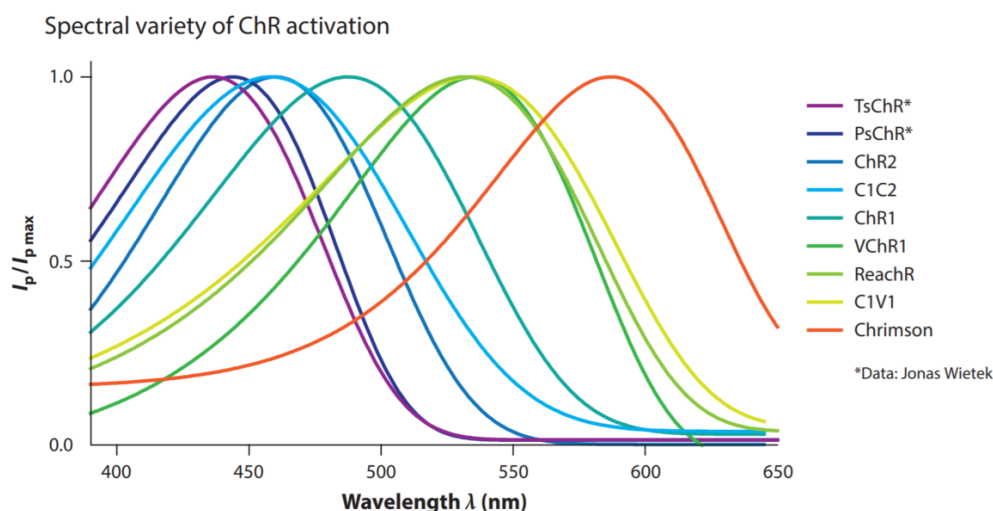


Figure 1.8 Action spectra of ChRs. Taken from [69].

1.3.6 Perfecting ChRs

Although ChR2 shows many exceptional properties as an optogenetic tool. It still contains some unfavorable characters, for example, strong inactivation, moderate expression level and photocurrent amplitude. In turn, considerable efforts have been taken into perfecting ChRs.

The first endeavor of improving ChR2 can be tracked to its discovery. Nagel et al.

found that truncation of the cytosol part of ChR2 did not affect its channel function [9]. Normally, the C-terminal domain is replaced by fluorescent proteins for monitoring expression in target cells or tissues. Later on, Nagel et al. reported the first *in-vivo* manipulation of animal behavior by using ChR2-H134R. It's the first ChR2 mutant, showing increased photocurrent with improved Na⁺ conductivity and reduced inactivation as well as improved retinal binding affinity in *Caenorhabditis elegans* [14]. Since then, the journey of ChRs engineering was launched. ChRs are such flexible proteins that endures extensive modifications for increasing expression and photocurrent amplitude [14, 81, 90, 94], shifting action spectrum [85, 87, 90-92, 95], accelerating or slowing photocycle [64-66, 81, 90, 94, 96, 97], reducing inactivation [66, 67, 95, 96, 98], and alternation of ion-selectivity [14, 68, 77-84]. The below Table 1.1 summarized the useful and improved ChR variants.

Table 1.1 Improved ChR variants

Constructs	Specific properties	Refs
ChR2-H134R	Improved photocurrent, sodium selectivity, and retinal binding affinity in <i>Caenorhabditis elegans</i> .	[14]
ChIEF	Fast photocycle and low inactivation	[96]
ChRGR	Green light activation, fast kinetics and low inactivation	[95]
Chronons	Large photocurrent with peaking absorbance at 500 nm Fast kinetics	[85]
ChR2-E123T/A/C	Improved kinetics and reduced voltage dependency of channel closing kinetics, but reduced photocurrent amplitude	[97]
ChR2-T159C	Large photocurrents but slightly reduced kinetics, improved retinal binding affinity	[94]
ChR2-E123T/T159C	Large photocurrent with fast photocycle, less voltage dependence of channel closing kinetics.	[94]
ChR2-C128T/A/S, ChR2-D156A/N, ChR2-C128S/D156A	slow photocycle and extended open-state lifetimes, improved light sensitivity, Yellow/red and UV light to close the channel.	[64, 65, 90]
ChR2-XXL (D156C)	Very high light sensitivity, Very high retinal binding affinity, Very high expression level and photocurrent amplitude, very slow photocycle,	[64, 66]
ChR2-XXM (D156H)	High light sensitivity, High retinal binding affinity, Very High expression level and photocurrent amplitude, Improved Ca ²⁺ conductance, Improved Na ⁺ /K ⁺ conductance (found in this thesis)	[67, 68]

ChR2-L132C	Large photocurrent amplitude, improved Ca ²⁺ permeability, High light sensitivity	[81]
<i>PsChR</i>	Blue shifted action spectrum, larger single-channel conductance and high Na ⁺ permeability	[87]
ChromeQ (ChR2- A71S/ E90A/H114G/R115S)	Improved photocurrent, order-of-magnitude reductions in calcium and proton conductance, high fidelity in driving repetitive APs in neurons	[99]
ChloC, iC1C2, iChloC, iC++	Chloride conducting ChR engineered from ChR2 Chloride conducting ChR engineered from C1C2 Improved ChloC with reduced cation conductance and improved current amplitude Improved iC1C2 with reduced cation conductance and improved current amplitude	[77-80, 100]
<i>GtACR1</i> , <i>GtACR2</i>	Natural chloride conducting ChR and large photocurrent amplitude	[101]
FLASH(<i>GtACR1</i> - R83Q/N239Q)	Fast kinetic <i>GtACR1</i>	[102]
ReaChR	Red-shifted spectrum, improved membrane trafficking, higher photocurrents and faster kinetics	[91]
C1V1- E122T/E162T	Large photocurrent, Peak absorption 540 nm, Moderate apparent off kinetics ~40 ms, Ideal for two-photon stimulation	[90]
(<i>Cs</i>)Chrimson	Activation peaking at 590 nm, Improved membrane targeting by use of the <i>CsChR</i> (ChR87) N- terminus	[85]
vf-Chrimson	Accelerated kinetics upon red-light stimulation and reduced photocurrent amplitude, significantly slowed photocycle upon blue/UV light stimulation (found in this thesis)	[103]
Chrimson-S169A	Red-shifted action spectrum, Accelerated kinetics upon red-light stimulation, reduced photocurrent amplitude significantly slowed photocycle upon blue/UV light stimulation (found in this thesis)	[88]
ChRmine	Large photocurrents with millisecond spike-timing fidelity, Robust Na ⁺ /K ⁺ permeability, Red shifted spectrum with high light sensitivity	[104]
ChRger2	High photocurrent amplitude, very high light sensitivity, Enables transcranial optogenetics	[105]

1.4. Enzymatic photoreceptor toolbox

The success of microbial rhodopsins in optogenetics further stimulates introducing

the non-rhodopsin photoreceptors as optogenetic actuators. One of the most successful application is the optogenetic control of the fundamental second messenger (cAMP or cGMP) signaling pathway. Compared with previous pharmacological methods, optogenetic control of cAMP/cGMP shows unprecedented spatiotemporal precision and becomes increasingly popular. The main actuators will be detailed in the following.

1.4.1 Optogenetic manipulation of cAMP

1.4.1.1 EuPAC

The first success for optogenetic control of cAMP was achieved by Nagel's lab in 2007. They heterologously expressed the photoactivated adenylyl cyclase from a unicellular flagellate, *Euglena gracilis* (EuPAC) in *Xenopus* oocytes (Fig. 1.9A-B), HEK293 cells and in *Drosophila melanogaster*, where neuronal expression yielded light-induced behavior changes [18]. EuPAC was discovered in 2002 from studying the photophobic responses of *Euglena gracilis* and was proven to be able to catalyze cAMP synthesis after blue light illumination [106]. EuPAC consists of two chains, PAC α and PAC β (Fig. 1.9A). PAC α forms antiparallel intermolecular dimer and exhibits hundreds-times higher activity than PAC β (Fig. 1.9C-D) [18, 107]. Therefore, only PAC α was used as the molecular tool for optical cAMP manipulation. After the initial trial, PAC α was further applied in other systems, including *Aplysia* neurons [108] and in *Caenorhabditis elegans* cholinergic neurons where it was used to manipulate neurotransmitter release [109]. However, several shortcomings of PAC α hinders its wide application, such as large molecular mass (>1000 aa), low solubility, and significant dark activity.

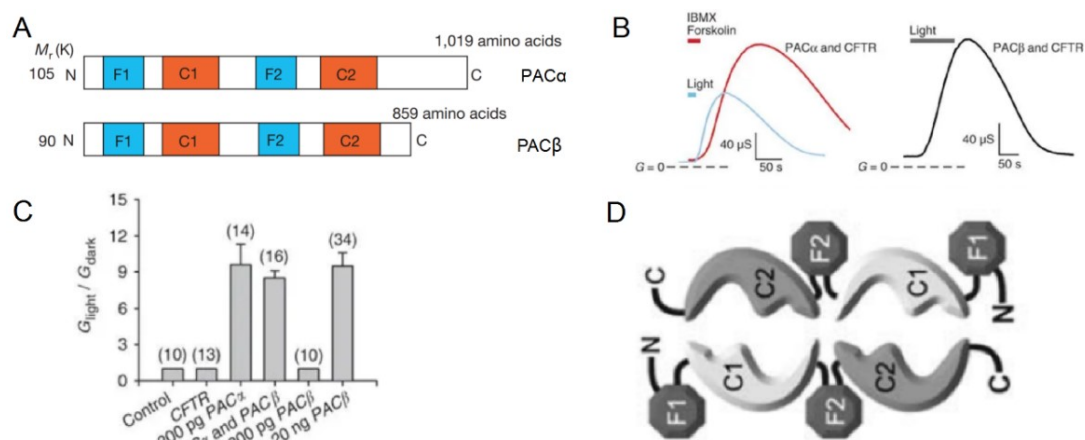


Figure 1.9 EuPAC, the first optogenetic tool for cAMP manipulation.

(A) Structural features of the PAC α and PAC β . (B) Conductance changes of oocytes expressing cystic fibrosis transmembrane conductance regulator (CFTR) and PAC α (200 pg cRNA, left) or PAC β (20 ng cRNA, right). (C) Comparison of light-induced conductance changes in oocytes

expressing PACs with CFTR. (D) Model of catalytic center formed by intermolecular C1-C2 dimer. Taken from [18, 106, 107].

1.4.1.2 bPAC

bPAC from the soil bacterium *Beggiatoa*, composed of a blue light receptor using flavin (BLUF) domain and an adenylyl cyclase domain (AC), shows superior features in comparison with PAC α . The small size (350 aa), low dark activity and high light activity make bPAC the most popular tool for cAMP manipulation [110, 111]. Co-expression of bPAC with either CFTR or olfactory cyclic nucleotide-gated ion channel (CNG-channel) in *Xenopus* oocytes evoked reliable transient photocurrent upon blue light illumination. In addition, bPAC is also applicable in neurons. Expression of bPAC in conjunction with CNG channels (CNG-A2) in CA1 pyramidal cells induces rapid and highly reproducible photocurrent when applying blue light irradiation. More importantly, bPAC outperforms both EuPAC α and forskolin/IBMX pharmacological cocktail in evoking CNG currents (Fig. 1.10). Besides neural application, bPAC was further introduced in various studies including sperm fertilization [112], neuronal repair [113], neurotransmission [114], mechanosensitive GPCR [67] and insulin secretion [115]. bPAC is not just a versatile tool for optogenetic application, but also a perfect object for studying the general sensor/effector communication principle and intramolecular signal transduction of the photoreceptor. Mechanism study of bPAC signal transduction not just facilitates the study of blue light receptor, but also benefits the photoactivated enzyme engineering.

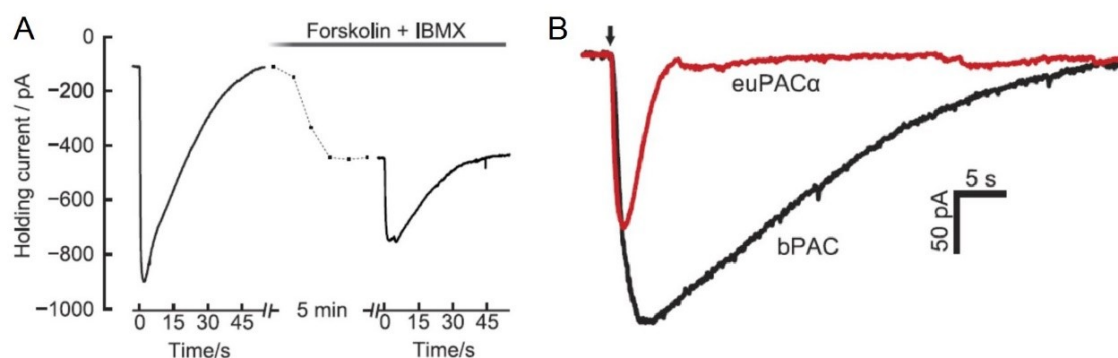


Figure 1.10 Comparison of bPAC, Forskolin/IBMX and EuPAC α induced currents in neurons. (A) Light induced cAMP-gated current in CA1 pyramidal cell expressing bPAC and CNG-A2 before and after forskolin/IBMX (100 μ M each) wash-in. Applying Forskolin/IBMX cocktail only partially obturated light-induced currents. (B) Photocurrent evoked by 100 ms blue light application

in neurons expressing CNG-A2 and EuPAC α (red) or CNG-A2 and bPAC (black). Taken from [110].

1.4.1.3 Molecular mechanism of photoactivation of bPAC

The AC domain of bPAC belongs to type III ACs, which are only functional in a homodimer form. However, the isolate AC domain of bPAC shows very low, if any, activity compared with the full-length protein, suggesting that the BLUF domain may mediate the dimerization of AC domain and/or reconfigure the AC into an active state upon photoactivation [116]. The later solved high-resolution crystal structure of bPAC clearly demonstrated that the dimerization of bPAC is mainly contributed by the helix α_3 in the BLUF domain (Fig. 1.11A). Extensive hydrophobic interactions between the $\alpha_{3\text{BLUF}}$ of each chain maintain the dimerization of bPAC, similar to its homologue OaPAC [117, 118]. Comparison of the dark state, illuminated state, and pseudo-lit state (constitutively active Y7F mutant) bPAC structures revealed the light activation pathway from within the BLUF domain to the AC domain. Light absorbance triggers conformational change of Y7 in BLUF domain, which could directly transmit to the kink in $\beta_{4\text{BLUF}}$. The adjacent residue L8 forms direct interaction with $\alpha_{3\text{BLUF}}$. Meanwhile, H120 and E124 in $\alpha_{3\text{BLUF}}$ are in van der Waals contact with L75 and L77 in $\beta_{4\text{BLUF}}$. These interaction networks synergistically propagate the change of the photoactive residue to $\alpha_{3\text{BLUF}}$ and the C-terminal capping of BLUF domain. In addition, $\beta_{4\text{BLUF}}$ - $\beta_{5\text{BLUF}}$ tongue in the AC domain also directly contact with $\alpha_{3\text{BLUF}}$. Collectively, changes in $\alpha_{3\text{BLUF}}$ then relay to the AC domain for allosterically activation via opening the active site cleft for accommodation of ATP and repositions of catalytic residues (Fig. 1.11B) [117].

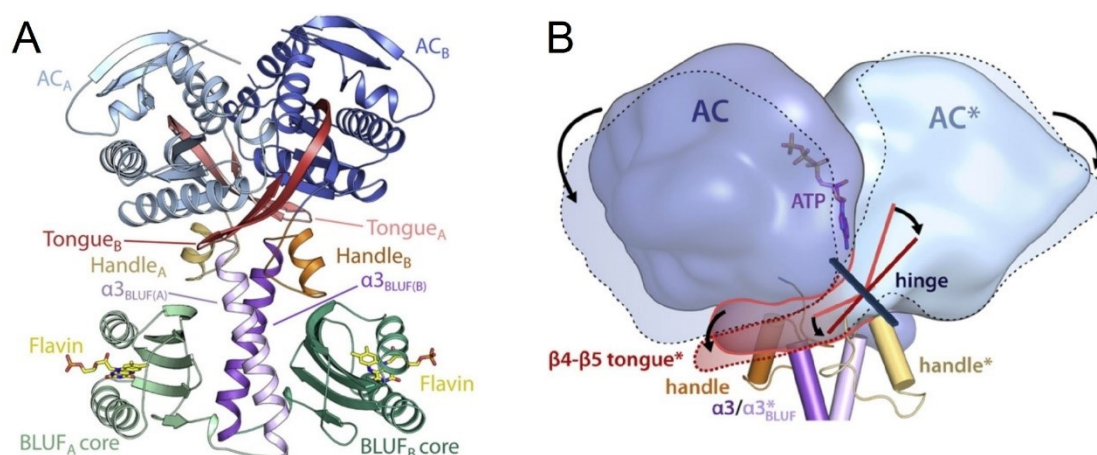


Figure 1.11 Structure and photoactivation mechanism of bPAC.

(A) The overall structure of bPAC in the $\alpha_{3\text{BLUF}}$ mediated homodimer form. (B) The structural

changes from the excited chromophore to a tongue-like extrusion of the AC domain through a conserved kink of the BLUF β -sheet regulates active site opening and repositions catalytic residues. Taken from [117].

1.4.1.4 Other PACs

Besides bPAC and EuPAC, a variety of PACs including nPAC [119], TpPAC [120], mPAC [121], OaPAC [118], cPAC [122] DdPAC [123] were identified or engineered and potentially can be introduced as the optogenetic tools for cAMP manipulation. Unfortunately, they either showed very high dark activity (e.g. mPAC), or the enzymatic activity is not determined unambiguously. In this thesis, I developed a fast convenient *in-vitro* assay allowing reliably quantification of the activity of these soluble PACs. Further engineering efforts were then applied to the best PAC candidate for cAMP manipulation.

1.4.2 Optogenetic tools for cGMP manipulation

The first light regulated guanylyl cyclase (bPGC or BlgC) was engineered by Ryu et al. through rational introduction of triple mutations (K197E/D265K/T267G) to bPAC [111]. However, it still contains unfavored residual AC activity, and no *in-vivo* application of this tool was reported yet. In 2014, a novel gene fusion named BeGC1 consisting of microbial rhodopsin domain and GC domain was identified in fungus *Blastocladiella emersonii*. This gene was suggested that involves the phototaxis behavior of the fungus [124]. Very soon in 2015, functional characterization of this protein was independently conducted by Gao et al. and Scheib et al. and named BeCyclOp (Cyclase Opsin) and BeRhGC (rhodopsin-guanylyl cyclase), respectively [125, 126]. Interestingly, BeCyclOp shows novel 8 TM helices topologies. Its long cytosolic N terminus is suggested to play roles in the regulation of GC activity (Fig. 1.12A). BeCyclOp shows superior properties in optogenetic cGMP manipulation. It is a tightly regulated cGMP specific cyclase with a very high photodynamic range (the ratio of light activity to dark activity is around 5000). Co-expression of BeCyclOp with CNG channel (TAX-2/4) in *Caenorhabditis elegans* muscle induced body contraction upon light illumination [125]. Contrary to light activated cGMP production, light activated cGMP degrading rhodopsin phosphodiesterase (RhoPDE) was also recently identified from *Salpingoeca rosetta* (Fig. 1.12B) [127]. At beginning, the light regulation of RhoPDE was under debated [128] but was later strongly proven to be photoactivable with light-enhanced substrate affinity. In addition, RhoPDE shows 100 times higher activity in the degradation of cGMP over cAMP [129]. Moreover, a group

of new RhoPDEs was identified in multicellular choanoflagellate and shown to be involved in light-regulated collective contractility [130]. Nature never stops surprising us. Light-inhibited GCs called “two-component cyclase opsins” (2c-CyclOps) were recently discovered in green algae *Chlamydomonas reinhardtii* and *Volvox carteri*. cGMP synthesis keeps sustaining in dark via ongoing phosphorylation and phosphoryl group transfer from histidine kinase domain to response regulator domain in 2c-CyclOps. Light illumination inhibits the phosphoryl transfer, resulting in decreased GC activity (Fig. 1.12C) [131]. Interestingly, all these cGMP related enzyme rhodopsins share a common 8 TM helices topologies (Fig. 1.12).

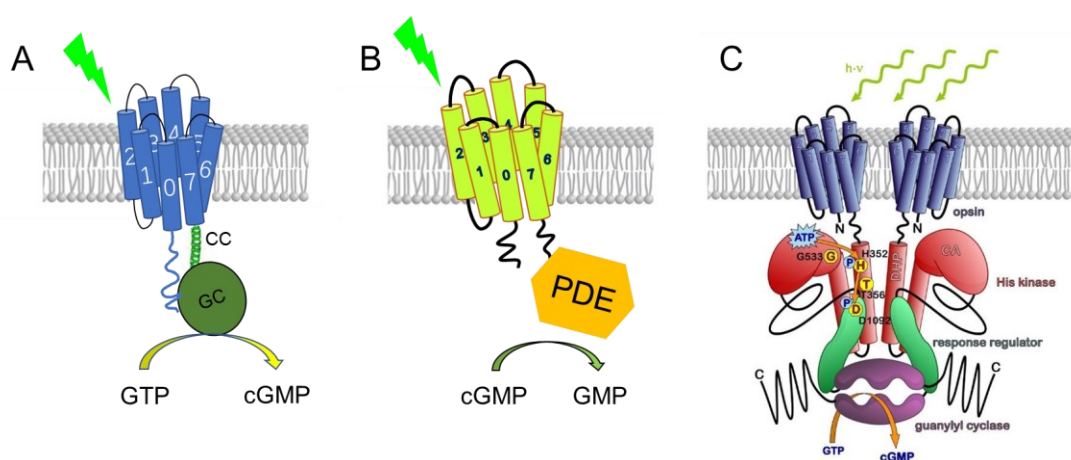


Figure 1.12 Light regulated cGMP related rhodopsin toolbox.

Models of the light activated GC, BeCycloP (A), the light activated PDE, RhoPDE (B), and the light inhibited GC, 2c-CyclOp (C). Modified from [125, 129, 131].

1.5 Two-component ion channels for optogenetic activation and inhibition

Rhodopsin-based ion channels toolbox offers various options for neural excitation and inhibition. However, ion channel like ChR2 is non-selective and low conductive for Ca^{2+} [9, 81]. To effectively manipulate the calcium signal, a more conductive light-gated channel with high Ca^{2+} permeability is of interest. In addition, high-efficient neural inhibitory tools are still lacking in the rhodopsin toolbox. Outward proton or inward chloride pumps need high-intensity illumination. Engineered or natural chloride channels depend on the TM electrochemical gradient of chloride [77, 78, 101]. These tools may either lead to altered ion distributions and/or produce contradictory results from the unintended change of ion contribution [132-136]. Therefore, light-gated potassium channel is highly desired. Existing potassium channel Blink1 poorly expressed on the plasma membrane [137]. Generation of two-component optogenetic

actuator by combining the light activated nucleotide cyclase and high conductive ion-selective CNG channel could in principle solve these two problems. Already in 2011, co-expression of bPAC with CNG-A2 in hippocampal pyramidal neurons showed reliable photocurrent production upon light illumination (Fig. 1.10) [110]. Similarly, light-gated Ca^{2+} permeant channel (OLF-bP) and K^+ selective channels (SthK-bP and PAC-K) were generated by the combination of bPAC with OLF channel and SthK channel, respectively [138, 139] (Fig. 1.13A-C). Expression of OLF-bP or SthK-bP in motoneurons of *Drosophila melanogaster* larvae enables controlling the mobility of larvae by light (Fig. 1.13D) [138]. Both SthK-bP and PAC-K robustly silence the neuronal firing in brain slices in a reversible manner (Fig. 1.13E- F). However, different strategies in combining bPAC and SthK may confer the synthetic constructs different characters. In this work, I systematically compared the photocurrent amplitudes, the kinetics and the cAMP productions of different bPAC-SthK constructs. Moreover, the relative narrow blue range action spectrum of bPAC allows independent bidirectional control of cell activity by two wavelengths light when combining with red-light activated ChRs. In this thesis, the improved SthK-bP and vf-Chrimson variants were demonstrated to be a promising toolset for dual-color optogenetics.

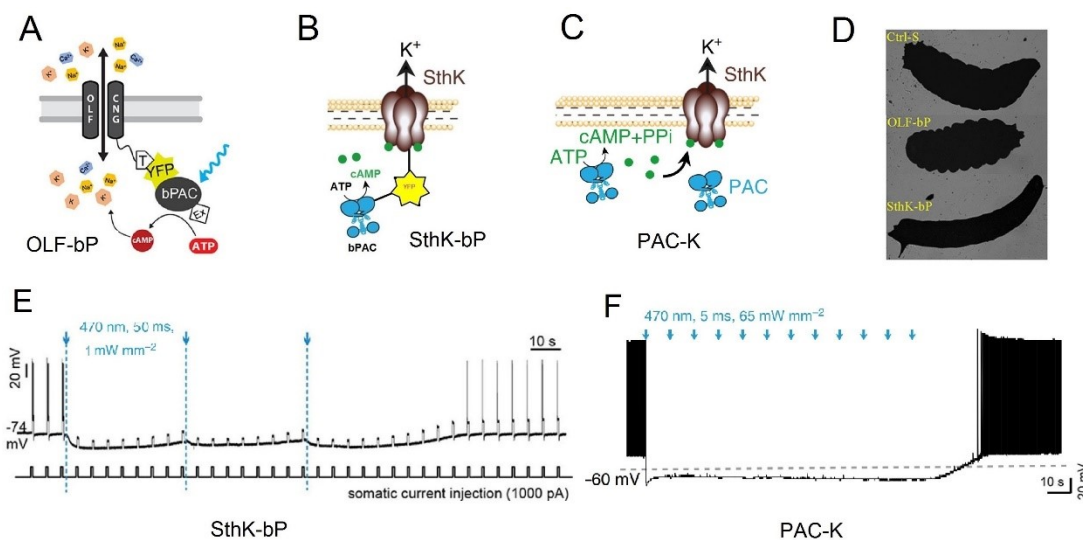


Figure 1.13. Two-component ion channels for optogenetic activation and inhibition.

Schemes of fused constructs of OLF channel and bPAC (A), fused SthK and bPAC constructs (B), and split bPAC and SthK construct (C). (D) Continuous blue light illumination induced body contraction or extension in OLF-bP or SthK-bP expressing larvae, respectively. Both SthK-bP (E) and PAC-K (F) could inhibit constant current-elicited spiking when applying blue light illumination

in hippocampal slices. Modified from [138, 139].

1.6 Strategies for expanding the optogenetic toolbox

To fulfill the application needs, extensive efforts were actively applied to expand the toolbox. Here I summarize these approaches into 7 categories: (1) *Searching new tools from nature*. Exploring natural photoreceptor diversity may be the best way to obtain novel optogenetic tools. (2) *Mutagenesis*. Expansion of the optogenetic toolbox via point mutations has proven to be challenging but highly productive. Till now, most of the widely used ChR variants were obtained from mutagenesis (Table. 1.1). Information for point mutation normally either comes from homology-based sequences alignment or structure analysis. In addition, a knowledge-based small scale mutation screen (like cysteine scanning mutagenesis) was also applied in examining the cation permeability pathway of ChR2 and generating improved mutants [82]. (3) *Large scale screen assay*. Developing a robust assay for rapid phenotyping rhodopsin variants is the first and most important step. In 2015, Cosentino et al. performed a screening of potassium channel with improved photodynamic range by using potassium transport-deficient yeasts [137]. Very recently, Cho et al. developed an automatic automated, time-resolved screening method for rapidly phenotyping ChR2 variants [99]. (4) *Protein chimerization*. Protein chimerization enables creating novel proteins that assemble the advantages of the original proteins or even previous inexistent characters. Classic examples include C1V1 [90], ChIEF [96], and LAPD [140] etc. (5) *Machine-learning-guided protein design*. Nobel laureate Frances Arnold pioneered applying machine-learning-guided directed evolution into opsin engineering and obtained fruitful optogenetic actuators [105, 141]. (6) *Adopting molecular and cellular approaches to expand the optogenetic repertoire*. Precise optical manipulation of cell activity requires the optogenetic actuators are accurately expressed at the correct position of the cell. For example, to effectivity depolarization or hyperpolarization of membrane potential, the ion channel or pumps must be well expressed on the plasma membrane. However, many microbial rhodopsins suffer poor plasma membrane targeting problems. Therefore, applying the molecular trafficking principle to improve the membrane targeting efficiency will be very crucial, best exemplified by *NpHR*

engineering [44-46]. Moreover, subcellular compartmentalization of optogenetic tools, for example mitochondria [142] or soma localization [143], could also be achieved by proper modification. (7) *Protein topological inversion*. In 2018, Brown et al. showed that the transmembrane proteins can be inverted by recombination with N-terminal domains. Through topological inversion of rhodopsins, they obtained new variants with unique properties and claims that topologically inverting opsin proteins may double the existing opsin-based toolkit [144].

1.7 Research purpose

Optogenetics became successful in neuroscience with ChR2 as an easy applicable tool. Existing depolarization tools like ChR2 have certain limitations due to their relatively low signal-channel conductance and poor ion specificity, especially for the low Ca^{2+} permeability. Here I engineered several improved ChRs with larger charge transfer per molecule and improved ion selection specificity. For neural silencing, one of the most widely used hyperpolarizing tools *NpHR-TYE* suffers from its prominent inactivation, resulting in incapability for long-lasting inhibition. Here I systematically explored and biophysically characterized optimized photo-stimulation protocols as a novel approach for long-term optogenetic silencing. Besides neural manipulation, optogenetic intervention of cAMP signaling also became increasingly popular. However, existing PACs all contain obvious dark activity and the cytosolic localization prevents subcellular precise cAMP manipulation. Here I generated a set of engineered PACs with different reduced dark activity and subcellular localization. Moreover, fusion bPAC with cAMP-gated potassium channel SthK enables robust blue-light mediated hyperpolarization. When coupling with improved red-light activated *vf-Chrimson* variant, dual-color mediated bi-directional control of cell activity could be achieved. Taken together, this study expanded the optogenetic toolbox and will further facilitate the optogenetic application in bioscience.

2 Methods

2.1 Chemicals and reagents

All the chemicals including antibiotics were obtained from Sigma unless otherwise stated. Kits for plasmid extraction, PCR purification and Gel extraction were obtained from QIAGEN. Phusion® High-Fidelity DNA Polymerase was used here for PCR. Restriction enzymes and Ligase enzyme for cloning were purchased from Thermo Fisher Scientific. All the primers were ordered from Sigma.

2.2 Molecular biology

2.2.1 DNA cloning

Genes used here including ChR2, *NpHR*, PACs, CycOps, Chrimson, and SthK were synthesized by GeneArt Strings DNA fragments (Life Technologies, Thermo Fisher Scientific). DNA fragments amplification was achieved by PCR (See the recipe of PCR mix in Table 2.1). PCR program parameters were adjusted according to the individual primer pair. The PCR products were analyzed by DNA electrophoresis. Afterwards, PCR products with correct size on the agarose gel were extracted using the Gel extraction kit from QIAGEN. After restriction enzyme digestion, purified DNA fragments were inserted into pGEMHE 22.

Table 2.1 The recipe of PCR mix

PCR reaction system	Total 20µL
DNA template	1 µL (about 20 ng)
HGD buffer	4.6 µL
Forward primer (10µM)	0.8 µL
Reverse primer (10µM)	0.8 µL
Phusion DNA Polymerase	0.2 µL
dNTP (10mM)	0.8 µL
BSA (100 mg/ml)	0.2 µL
ddH ₂ O	11.6 µL

2.2.2 Site-directed mutagenesis

Point mutations were introduced by QuikChange PCR. To remove the original plasmid, the PCR mix after amplification was incubated with DpnI enzyme for 3 hours at 37 °C.

2.2.3 *E. coli* transformation

The above obtained products were transformed into *E. coli* MRF strain by heat-shock method. The transformed *E. coli* MRFs were then plated on the LB agar plates with intended antibiotics and incubated at 37 °C overnight. Growing colonies were then selected either by colony PCR or cracking methods.

2.2.4 Colony PCR

Colony PCR is a rapid method for screening positive colonies of yeast or bacteria that carrying the desired genetic construct. Colonies were picked up and pipetted with 10 µL sterile water in a tube. After incubated at 98 °C for 10 min, this 10 µL mixture was then centrifuged down at 16,000g for 10 min. The obtained supernatant was used as PCR template. The rest steps of colony PCR follow standard PCR procedure. Positive colonies were then selected and cultured in 5 mL LB medium with antibiotics overnight.

2.2.5 Cracking of *E. coli* cells

After picking up the colonies and pipetting with 5-10 µL sterile water in a tube, an equal volume of 2x cracking buffer (Table 2.2) was then added into the tube and incubated for 10 min at room temperature. After adding the loading buffer, the mix was centrifuged at 16,000g for 2 min, and loaded in 1% DNA agarose gel to check the size of supercoiled plasmids. 2-4 colonies with correct band size were picked for overnight culture in 5 mL LB medium with antibiotics.

Table 2.2 Cracking buffer (2x)

0.2 N NaOH
0.5% SDS
20% Sucrose

2.2.6 Plasmids extraction and verification

Plasmids were extracted by using the Qiaprep spin miniprep kit (Qiagen, Hilden, Germany). The obtained plasmids were then verified first by restriction endonuclease digestion and then sent to GATC Biotech for sequencing (GATC Biotech, Constance, Germany). Correct constructs were stored at -20 °C for future use.

2.2.7 cRNA generation

Linearized plasmid DNA (with final concentration about 250 ng/μL) was obtained via NheI digestion for the *in vitro* generation of cRNA with the AmpliCap-MaxT7 High Yield Message Maker Kit (Epicentre Biotechnologies), as depicted in Table 2.3. The 10 μL mixture was then incubated at 37 °C for ~3 h. Equal volume 5 M Ammonium acetate (CH₃COONH₄) was added and mixed thoroughly with the reaction mixture after incubation. After frozen at -20 °C for at least 30 min, the mixture was then centrifuged at 4 °C, ~30,000 ×g for 1 h. The pellet was then washed with 50 μL 70% ethanol and dried in a fuming hood. After the white pellet became transparent, add 10-15 μL RNase-free H₂O to dissolve the pellet. The obtained cRNA were then stored at -20 °C.

Table 2.3 *In-vitro* transcription

AmpliCap-Max Cap/NTP PreMix	4 μL
100 mM Dithiothreitol (DTT)	1 μL
10×AmpliCap-Max TM T7Transcription Buffer	1 μL
AmpliCap-Max TM T7 Enzyme (5 U/μL)	1 μL
RNase Inhibitor (20 U/μL)	1 μL
Add Linear DNA (~600 ng) to final 10 μL	

2.3 Oocytes preparation

Xenopus laevis surgery for oocytes was under License #70/14 from Landratsamt Würzburg Veterinaeramt. The oocytes from *Xenopus laevis* were first washed twice in Ca²⁺-free ND96 buffer (Table 2.4), and digested with 5 mg/mL collagenase for ~1.5 h. After digestion, the oocytes were washed three times by ND96 solution with 1 mM CaCl₂ and 50 μg/mL Gentamycin. The obtained oocytes were then transferred into a petri dish at 16 °C incubator for culture.

Table 2.4 ND96 solution

NaCl	96 mM
KCl	2 mM
MgCl ₂	1 mM
CaCl ₂	1 mM
HEPES	5 mM
Adjust pH to 7.4	

2.4 Microinjection and maintenance of oocytes

The cRNAs were injected into the oocytes by the nano injection machine (Nanoject, Drummond Scientific Company). The injection capillary (3.511 Drummond #3-000-203- G/X; Drummond Scientific Company) was made by a vertical Puller (PP-83; Narishige). The injected oocytes were cultured in ND96 buffer at 16 °C with (for rhodopsin constructs) or without (for non-rhodopsin constructs) additional 10 μM ATR. Culture solutions were changed daily to keep the oocytes in good condition.

2.5 Oocytes electrophysiology

2.5.1 Two-electrode voltage-clamp (TEVC)

The voltage-clamp technique is one of the most powerful electrophysiological methods, which developed since 1939 [145]. The method allows artificially controlling the membrane potential (V_m) of large cells to analyze the currents across cell membrane, which was normally mediate by ion channels or carriers. It contains two electrodes a voltage electrode as V_m sensor and a current electrode for current injection to maintain the membrane potential at a fixed value. As shown in Fig. 2.1, the oocyte is put in a small chamber with constantly flowing buffer in the bath. The voltage electrode (electrode 1) and current electrode (electrode 2) were injected into the oocyte. The current injected to the oocyte by the setup to maintain the command potential V_c corresponds to the current across the oocyte membrane (Fig. 2.1). TURBO TEC-05 system from npj (npj electronic GmbH, Tamm, Germany) is used in this study.

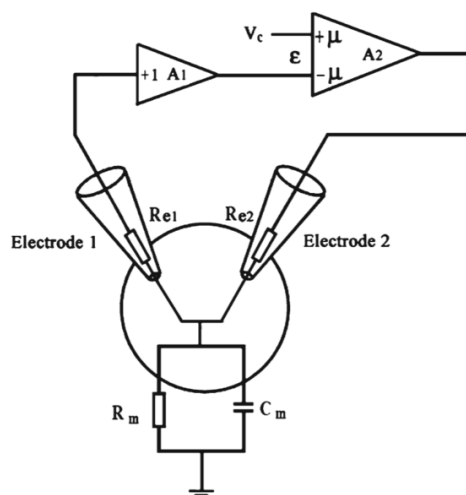


Figure 2.1 Conventional two-electrode voltage clamp (TEVC) on an oocyte.

V_m is monitored by connecting the voltage electrode (electrode 1) to the input of a voltage follower (A1) with high input impedance. The output potential of A1 is therefore approximately equal to V_m . The clamping amplifier (A2) ensures V_m to approach the voltage command signal (V_c) very closely. The current injected by electrode 2 is measured as the membrane current. Taken from [146].

2.5.2 Solution used for oocytes electrophysiology

The solutions used in this dissertation are listed in the following.

Table 2.5 Solutions for TEVC recording

	NaCl	NMG	KCl	CaCl ₂	BaCl ₂	MgCl ₂	MES	HEPES	CAPSO	pH adjustment
Ori-standard, pH 5.6	110	-	5	2	-	1	5	-	-	NaOH
Ori-standard, pH 7.6	110	-	5	2	-	1	-	5	-	NaOH
Ori-standard, pH 9.6	110	-	5	2	-	1	-	-	10	NaOH
NMG-Asp, pH 7.6	-	115	-	2	-	1	-	5	-	Aspartate
Ori-Ba ²⁺ , pH 7.6	110	-	5	-	2	1	-	5	-	NaOH
Ori-Ba ²⁺ , pH 9.6	110	-	5	-	2	1	-	-	10	NaOH
Ori-NMG(Ba ²⁺), pH 7.6	-	115	-	-	2	1	-	5	-	HCl
Ori-20Ca ²⁺ , pH 7.6	110	-	5	20	-	1	-	5	-	NaOH
Ori-30Ca ²⁺ , pH 7.6	110	-	5	30	-	1	-	5	-	NaOH
Ori-40Ca ²⁺ , pH 7.6	110	-	5	40	-	1	-	5	-	NaOH
High-Na ⁺ , pH 7.6	120	-	-	-	2	-	-	5	-	NMG
High-K ⁺ , pH 7.6	-	-	120	-	2	-	-	5	-	NMG

High-Ba ²⁺ , pH 7.6	-	-	-	-	80	--	-	5	-	NMG
Low-Na ⁺ , pH 7.6	1	119	-	-	2	-	-	5	-	HCl
Low-K ⁺ , pH 7.6	-	119	1	-	2	-	-	5	-	HCl
Low-Ba ²⁺ , pH 7.6	-	119	-	-	0.8	-	-	5	-	HCl
High-Ca ²⁺ , pH 9	0.3	-	3	80	-	-	-	-	10	NMG

Note: 1. The unit in the table is mM.

2. Solutions with different chloride concentrations at pH 7.6 used in the *NpHR*-TYE project were prepared by mixing the Ori-standard with the NMG-Asp solution at different ratios.

2.5.3 Electrodes and capillaries for TEVC

The silver electrodes used for TEVC are chlorinated to generate the AgCl layer on the surfaces. Potential and current electrodes are inserted into the capillaries ($\Phi=1.5$ mm, Wall thickness 0.178 mm, Hilgenberg). The capillaries were made by a vertical puller (PC-10, Narishige) and filled with 3 M KCl.

2.5.4 Softwares for TEVC

The software used for TEVC includes WinWCP (University of Strathclyde) and WinEDR (University of Strathclyde).

2.5.5 Mathematical fitting of the electrophysiology data

The current decay kinetics of Chr2 variants and SthK-bPAC variants were fitted to obtain the τ_{off} values, either by mono-exponential or bi-exponentially function. The recovery from inactivation of *NpHR*-TYE-mediated currents was fitted, separately for each cell, by a bi-exponential function of the following form:

$$\text{recovery} = a1 \times e^{\frac{-\Delta t}{\tau1}} + a2 \times e^{\frac{-\Delta t}{\tau2}} + c$$

where Δt is the latency of the test pulse onset. The offset c was constrained to 100%.

The weighted time constant τ_w was computed as follows:

$$\tau_w = \tau1 \times \frac{a1}{a1 + a2} + \tau2 \times \frac{a2}{a1 + a2}$$

2.5.6 Light source

For oocyte electrophysiology recording, a 635 nm, a 532 nm laser, a 473 nm laser, a 450 nm laser (Changchun New Industries Optoelectronics Tech), a 400 nm LED (ProLight Opto Technology) and a 590 nm LED (WINGER) were used as light sources.

The light intensities at different wavelengths were measured with a Laser Check optical power meter (Coherent Inc.).

2.6 cAMP/cGMP ELISA assay from whole oocyte lysates

Oocytes injected with indicated amount cRNA of PACs, bPGC or CyclOps variants were incubated at 18 °C for 3 days in Ringer solution. Oocytes were either kept in the dark or illuminated for 30 s with 473nm blue light at 0.3 mW/mm². Five oocytes for each injected construct were pooled and homogenized by pipetting in 0.1 N HCl (Arbor Assays). Cell debris was removed by centrifugation at 30,000g for 10 min at room temperature. cAMP in oocyte was quantified by using DetectX High Sensitivity Direct Cyclic AMP Chemiluminescent Immunoassay Kit (Arbor Assays).

2.7 Oocytes crude membrane protein extracts preparation

15 control oocytes (without cRNA injection) or oocytes expressing membrane-anchored proteins were pooled and washed 3 times in solution A (75 mM Tris-HCl, 300 mM NaCl, 2 mM MgCl₂, 5 mM DTT, 1x Protease Inhibitor Cocktail (Roche), pH 7.4). After gently homogenized in 450 µL solution A by pipettes on ice, the yolk and cellular debris were sedimented by 500 × g centrifugation at 4 °C for 15 min. The supernatant was transferred to a new tube and centrifugated at 30,000 × g at 4 °C for 20 min for separation of membrane pellets and soluble fraction. The supernatant was discarded. The membrane pellets were gently washed twice with 500 µL solution A and re-suspended with solution A at a ratio of 1 oocyte to 4 µL. The resuspended fraction was again centrifugated with a final 500 × g at 4 °C for 5 min to remove possible residual big cellular debris. The rest membrane suspension was collected as the membrane extracts for *in-vitro* reaction.

2.8 Oocyte membrane extract *in-vitro* reaction

To start the enzymatic reaction, 4 µL membrane extract was mixed with 36 µL reaction buffer mix (75 mM Tris-HCl, pH 7.4, 100 mM NaCl, 5 mM DTT, 5 mM MgCl₂, 1 mM ATP, 0.2 mM GTP) either in black tubes (dark activity) or under illumination (473 nm, 0.3 mW/mm²). Aliquots of 10 µL were taken from the *in-vitro* reaction mix and stopped by adding 190 µL Sample Diluent (containing 0.1N HCl, Arbor Assays) at 3 different time points in the light (1, 4, and 7 min) and in the dark (5, 25, and 45 min). cAMP concentration was quantified by using the above described ELISA Kit. For cGMP assay, the reaction buffer mix contains 75 mM Tris-HCl, pH 7.4, 100 mM NaCl,

5 mM DTT, 5 mM MgCl₂, 0.1 mM ATP, 0.1 mM GTP. cGMP concentration was also quantified by using Elisa Kit. Turnover numbers were normalized to the amount of membranes protein, which was quantified through eYFP-tag emission.

2.9 Oocytes crude soluble protein extracts preparation and *in-vitro* assay

15 control oocytes (without cRNA injection) or oocytes expressing soluble proteins were pooled and washed 3 times in solution B (75 mM Tris-HCl, 100 mM NaCl, 2 mM MgCl₂, 5 mM DTT, 1x Protease Inhibitor Cocktail (Roche), pH 7.4). After gently homogenized in 450 μ L solution A by pipettes on ice, the yolk and cellular debris were sedimented by 30,000 \times g centrifugation at 4 °C for 20 min. Discard the pellet and gently remove the lipid layer on the surface of the supernatant. The supernatant was transferred to a new tube and centrifugated at 30,000 \times g at 4 °C for another 20 min to remove the residual lipid layer. The supernatant was collected as the oocyte soluble extracts. The collected supernatant was then performed dialysis by an ultra-centrifugal filter tube for removing the small proteins, endogenous ATP/GTP, cAMP/cGMP and other small molecules. After dialysis, the obtained crude soluble extracts were then used for the *in-vitro* reaction. To start the reaction, ATP (final concentration at 1 mM) and GTP (final concentration at 0.2 mM) were added into the crude soluble extracts. Aliquots were taken from the *in-vitro* reaction mix and stopped by adding Sample Diluent at fixed time points in the light and in the dark. cAMP/cGMP Elisa kits were used for concentration quantification.

2.10 Protein quantification by fluorescence.

The Fluorescence emission of eYFP standard (Evrogen JSC; 1 mg/ml) of known concentration (dilution to 0, 5, 10, 20, 40, 80, and 160 ng with solution A, three repeats) was measured at 538 nm by using a Fluoroskan Ascent microplate fluorometer with 485 nm excitation. The protein levels in *Xenopus* oocyte membranes and soluble extracts were obtained by fitting into the standard curve.

2.11 Fluorescence imaging

After 2 or 3 days expression, fluorescence pictures of *Xenopus* oocytes were obtained either by a Leica DMI8 fluorescence microscope or by confocal laser scanning microscope (LSM 5 Pascal, Carl Zeiss) equipped with a Zeiss Plan-Neofluar 10 \times /0.5 objective.

2.12 Experimental design and statistical analysis

Data were analyzed using pClamp 10, WinWCP, Microsoft Excel. Statistical analyses were performed using OriginPro 2018, Prism 7. Data were reported as mean \pm standard deviation (SD) or mean \pm standard error of the mean (SEM). The Kolmogorov–Smirnov test was used to test for the normality of data. Parametric testing procedures were applied for normally distributed data; otherwise non-parametric tests were used. In case of two-sample *t*-tests and unequal group variances, Welch’s correction was applied. In case of multiple comparisons, analysis of variance (ANOVA) was used (*post hoc* tests indicated in Results). P values (two-tailed tests) < 0.05 were considered statistically significant.

2.13 Bioinformatics

The Benchling Life Sciences R&D Cloud is used for DNA and protein sequences editing and normal alignments.

Multiple sequence alignments were done by the online portal of Clustal Omega.

Protein structure analysis was conducted by using PyMOL Or UCSF Chimera.

3. Results

3.1 Engineering of high-performance ChR2 variants with altered ion selectivity

ChRs are the most used optogenetic tools for depolarizing the membrane potentials of excitable cells. However, the current ChR toolbox remains inadequate for some tailored applications. As a matter of fact, different ChR variants should be selected for activation of different cell types. Fruitful results have been obtained in modifying the photocurrent amplitudes [14, 81, 90, 94], the action spectrums [85, 87, 90-92, 95] and the kinetic properties of ChRs [64-66, 81, 90, 94, 96, 97]. However, significantly altering the ion selectivity of ChRs remains very challenging. Almost all ChRs predominately permeable for H^+ , which may cause cellular acidification upon prolonged illumination [147]. On the contrary, Ca^{2+} conductance is very low in ChRs. Existing calcium translocating ChR mutant (CatCh) only slightly increases the Ca^{2+} conductance with a factor of 1.4 [81]. Moreover, the unitary conductance of ChRs is low. Through rational design, here I developed improved ChR2 variants with larger charge transfer per molecule and higher ion-permeable specificity (i.e. higher Na^+/K^+ , or Ca^{2+} permeability).

3.1.1 Template selection for engineering

To engineer an ion channel with high ion-permeable specificity and high photocurrent amplitude, I first tested different ion channels to select the ideal template for further engineering. ChR2 variants from *Chlamydomonas reinhardtii* were selected for the following reasons. First, unlike high H^+ selective channel Chrimson and Chronos [68, 85, 86], ChR2 contains intrinsic Na^+/K^+ and Ca^{2+} conductance. Second, ChR2 shows superior expression properties in various organisms. Third, as the best-studied ion channel, the wealth of biochemical and biophysical data and available structure information provide directions for ChR2 engineering. Recent engineered ChR2-XXM displays very high expression and photocurrent amplitude [67], rendering a better candidate than wt-ChR2 for engineering. To compare the ion selectivity between ChR2 and ChR2-XXM, TEVC recordings in different solutions were performed. Both constructs showed decreased photocurrent amplitude after changing extracellular solution from Ori- Ba^{2+} to Ori-NMG solution at pH 7.6, indicating that both H^+ and Na^+ ions contribute to photocurrent (Fig. 3.1A-B). Changing the

extracellular solution from Ori-Ba²⁺ at pH 7.6 to Ori-Ba²⁺ at pH 9.6 led to reduced photocurrent amplitude for ChR2 but increased photocurrent for XXM. As all the cations compete with each other for passing the channel [76], this result suggested increased Na⁺ permeability of XXM in comparison with ChR2. I therefore measured the current-voltage relationships and calculated the shifts of the reversal voltages (V_r) of ChR2 and XXM upon changing of the extracellular Na⁺ concentrations. The elevated V_r shift confirmed the increased Na⁺ conductance of XXM (Fig. 3.1C).

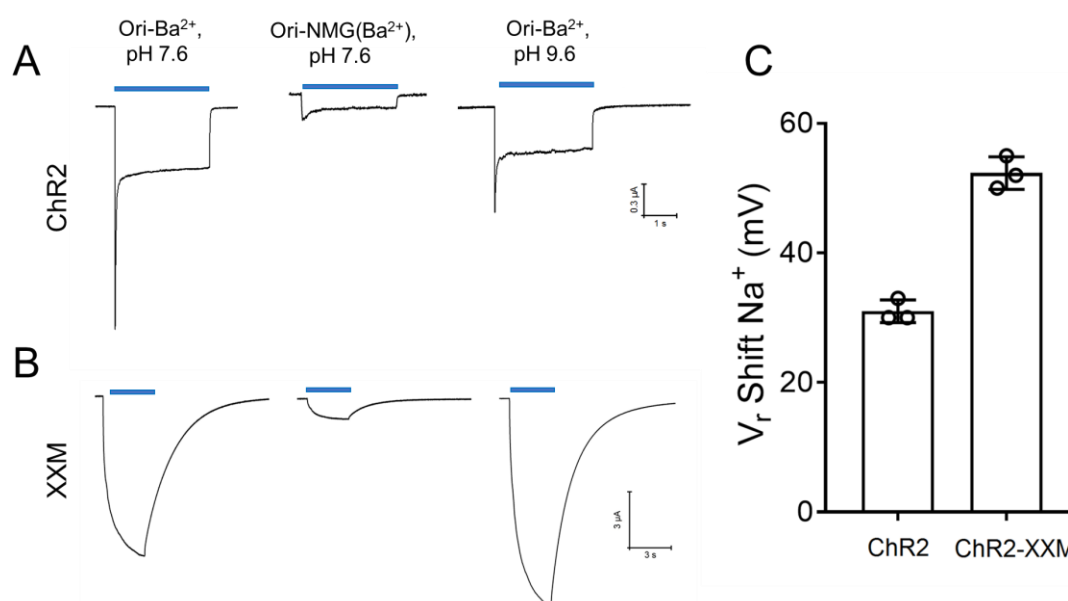


Figure 3.1 Comparison of ChR2 and ChR2-XXM.

Photocurrent sample traces of ChR2 (A) and ChR2-XXM (B) in different indicated extracellular solutions. Holding at -100 mV. 473 nm at 3 mW/mm² was used here. (C) Reversal potential (V_r) shift of ChR2 and ChR2-XXM upon changing the Na⁺ concentration from 120 mM to 1 mM at pH 7.6. Data are presented as Mean \pm SD. n = 3.

3.1.2 Engineering ChR2 variant with improved Na⁺/K⁺ and Ca²⁺ conductance

Structure analysis of ChR2 revealed three molecular gates that exist in the ion-permeable pathway but without specific ion selective filter [63], suggesting that these three molecular gates may partially contribute to the ion-permeable specificity. Accordingly, modifying the gates of ChR2 will influence the ion selectivity of ChR2. Indeed, reported ChR2 variants with altered ion selectivity are nearly all generated by mutating the residues that form the three molecular gates [14, 68, 77-84]. For example, H134 involves the formation of the intracellular gate and the H134R mutant shows slightly enhanced Na⁺ selectivity [14, 63, 96]. Here I introduced a new point mutation

H134Q into XXM to obtain the double mutant ChR2-H134Q/D156H. Sequence comparison of ChR2 with light-driven sodium pumps revealed that the homologue of H134 in the sodium pumps is a very conserved glutamine (Fig. 3.2A), which is also confirmed by structure alignment of ChR2 and KR2 (Fig. 3.2B). The H134Q/D156H mutant displayed a comparable expression level with XXM in *Xenopus* oocytes (Fig. 3.2C) and retained similar favorable kinetic properties like XXM. When illumination with short light pulse (10 ms), H134Q/D156H could fast ($\tau_{\text{off1}} = 11.6 \pm 2.2$ ms, $\tau_{\text{off2}} = 0.7 \pm 0.1$ s, Fig. 3.2D) recovered to the initial state. At pH 7.6, H134Q/D156H showed higher V_r shift than XXM when changing the extracellular Na^+ concentration, indicating the improved Na^+ conductance of H134Q/D156H. In addition, the K^+ conductance of H134Q/D156H is also increased compared to XXM, (Fig. 3.2E, Table 3.1). More importantly, H134Q/D156H displays about 2 times higher photocurrent amplitude than XXM aside from the enhanced Na^+/K^+ specificity (Fig. 3.2F). Considering the similar expression levels, it's conceivable that H134Q/D156H has a higher single-channel conductance than XXM. XXM has been reported with high Ca^{2+} conductance, I next compared the Ca^{2+} permeability between XXM and H134Q/D156H [68]. Higher V_r shift from changing extracellular Ba^{2+} concentrations of H134Q/D156H suggested its enhanced Ca^{2+} conductance (Fig. 3. 2E). To directly measure the calcium current, BAPTA (1,2-bis(o-aminophenoxy)ethane-N,N,N',N'-tetraacetic acid) at a final concentration of 10 mM was injected into the oocyte to avoid the activation of the calcium-activated chloride channel (CaCC). H134Q/D156H exhibited about 4-fold higher inward current than XXM at -90 mV and 80 mM Ca^{2+} (Fig. 3.2F-G), confirming its improved Ca^{2+} conductance. In sum, H134Q/D156H outperformed XXM at almost all aspects, could serve as a promising tool for manipulation of Ca^{2+} influx in cell.

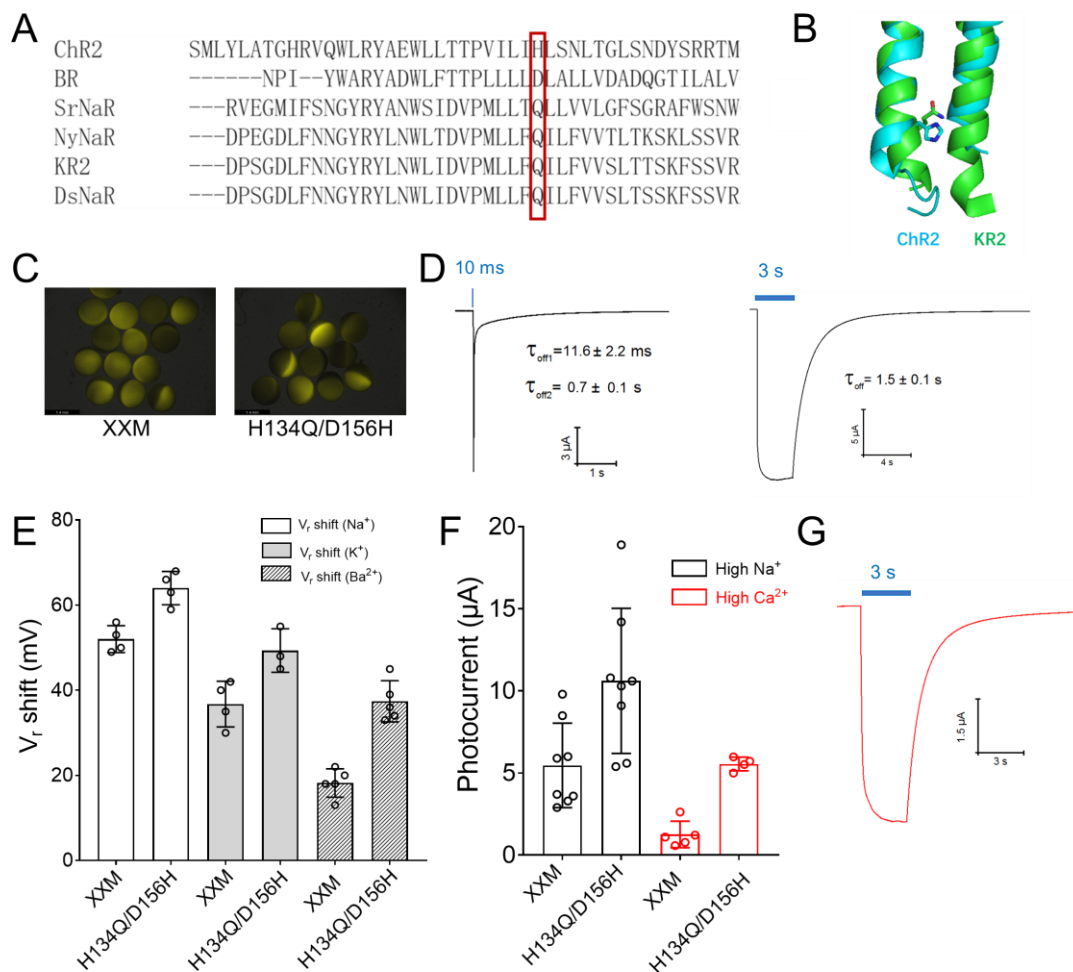


Figure 3.2 Generation and characterization of ChR2 double mutant H134Q/D156H with improved Na⁺/K⁺ and Ca²⁺ conductance.

(A) Sequence comparison of ChR2 with proton pump and sodium pump rhodopsins. (B) Structure alignment of ChR2 and KR2. (C) XXM and H134Q/D156H show similar expression levels in *Xenopus* oocytes. Both were injected with 30 ng cRNAs and incubated for 3 days with additional 10 μ M ATR. (D) Sample traces of H134Q/D156H upon short light pulse (10 ms) illumination (left) and prolonged (3 s) illumination (right) with indicated kinetic properties. Holding at -70 mV, measured in Ori-Ba²⁺ solution at pH 7.6. (E) V_r shift of XXM and H134Q/D156H upon changing extracellular Na⁺ or K⁺ concentration from 120 mM to 1 mM, or Ba²⁺ concentration from 80 mM to 0.8 mM. (F) Photocurrent amplitude comparison of XXM and H134Q/D156H. High Na⁺ solution is Ori-Ba²⁺, pH 7.6, in which the photocurrent is mainly contributed by Na⁺. Holding at -70 mV. High Ca²⁺ solution contains 80 mM CaCl₂, pH 9. Calcium currents were measured at -90 mV at 1.5 hours after BAPTA injection with final concentration at 10 mM. See sample calcium photocurrent trace in (G). For all measurements, 473 nm laser light at 5 mW/mm² is applied.

3.1.3 Generation of ChR2 variant with high photocurrent amplitude and high Na⁺/K⁺ selectivity

To further improve the photocurrent magnitude and the Na⁺/K⁺ permeable

specificity of ChR2, three additional residues E83, E101 and H114 were selected to mutate into H134Q/D156H. E83 participates in the assembly of the intracellular gate and forms a salt bridge with the core residue R268 in the intracellular gate. Moreover, its charged carboxylate group is extended to the putative ion-conducting pore, possibly involving proton transport [63]. Mutation of E83 to non-titratable Q has been shown to reduce the residual proton conductance in the chloride conducting ChR ChloC [79]. E101 locates near the extracellular gate and has been shown to influence the cation influx of ChR2 [63, 79, 148]. E83 and E101 here were either mutated to the negative charged residues with smaller side chain (E83D, E101D), or to the polar but uncharged residues (E83N, E83S, E101N and E101S). H114 is positioned at the extracellular loop of ChR2. This extracellular loop may affect the accessibility of cations to the channel cavity, although no functional significance has been reported yet. Mutating the titratable residue H114 might affect the photocurrent properties of ChR2. A concurrent study from Boyden's group reported that H114G reduces the proton influx of ChR2 [99]. Therefore, H114G mutation was further introduced into the double mutant H134Q/D156H. As expected, all engineered triple mutants displayed increased Na^+/K^+ conductance in comparison with H134Q/D156H (Table 3.1). I next checked their expression levels and photocurrent amplitudes. E83N/H134Q/D156H showed much reduced expression level, whereas the other triple mutants expressed similarly in oocytes (Fig. 3.3A). For the photocurrent amplitude, two mutations (E83D and H114G) showed enhanced effects, while the rest five (E83N/S and E101D/N/S) displayed either unchanged or even attenuated effects. To obtain an improved ChR variant with further enhanced current magnitude, mutations E83D and H114G were combined into H134Q/D156H. Interestingly, the quadruple mutant (E83D/H114G/H134Q/D156H) showed the highest photocurrent among all constructs, about 2.5 folds higher than H134Q/D156H, indicating these mutations are synergistically additive. In addition, a slightly slowed channel closure of the quadruple mutant was observed (Fig. 3.3C). The slowed channel closure increases the charge transfer through the channel during a single photocycle, suggesting improved light sensitivity.

Table 3.1 Na⁺/K⁺ selectivity of ChR2 mutants.

	V _r shift (mV)	
	V _r shift (Na ⁺)	V _r shift (K ⁺)
H134Q/D156H	64 ± 3.9	49.3 ± 5.1
E83D/H134Q/D156H	87.8 ± 9.6	84.5 ± 4
E83N/H134Q/D156H	81 ± 1.8	72.7 ± 3.1
E83S/H134Q/D156H	78.5 ± 2.1	64.3 ± 6.6
E101D/H134Q/D156H	74.3 ± 4.2	60 ± 2.6
E101N/H134Q/D156H	95 ± 2.2	85.5 ± 7.8
E101S/H134Q/D156H	92.8 ± 3.9	78 ± 8.9
H114G/H134Q/D156H	74.7 ± 5.5	61.7 ± 1.2
E83D/H114G/H134Q/D156H	82 ± 4.2	73 ± 1.7
E83N/E101D/H114G/H134Q/D156H	91.5 ± 3.4	81 ± 4.4

V_r shift was calculated by the reversal potential differences in two extracellular solutions containing 120 mM NaCl (KCl) pH 7.6 and 1 mM NaCl (KCl) pH 7.6. Values represent mean ± SD, n = 3 - 5.

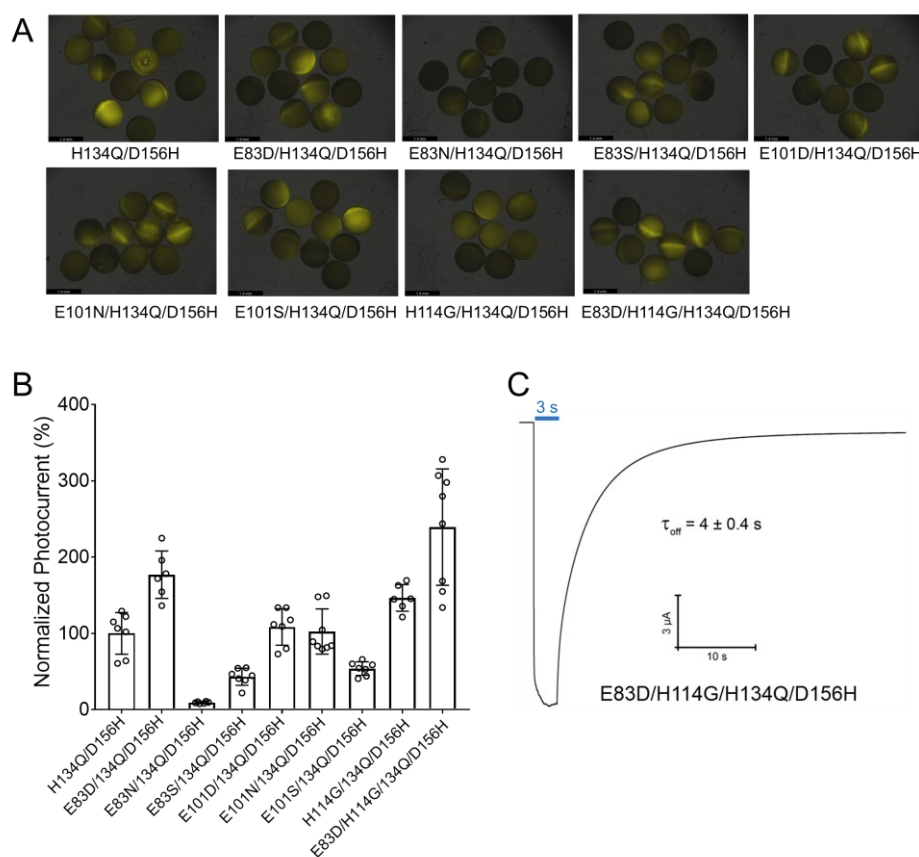


Figure 3.3 Generation of ChR2 variant with high photocurrent amplitude and high Na⁺/K⁺ conductance.

Expression levels (A) and photocurrent amplitudes comparison (B) of different ChR2 variants in

Xenopus oocyte. For all constructs, 30 ng cRNA was injected into each oocyte. (C) Representative photocurrent traces of ChR2-E83D/H114G/H134Q/D156H. Holding at -70 mV, measured in Ori-Ba²⁺ solution at pH 7.6. For all measurements, 473 nm laser at 5 mW/mm².

3.1.4 Generation of high Na⁺/K⁺ and low Ca²⁺ conducted ChR2 variant

ChR with robust Na⁺/K⁺ permeability is ideal for driving spikes in neurons under physiological ion distribution conditions. However, the intrinsic Ca²⁺ conductance may cause release of Ca²⁺ from intracellular stores [149, 150]. Here I aim to design a high Na⁺/K⁺ conducted ChR with much reduced Ca²⁺ permeability. Three additional mutations (E83N, E101D and H114G) were found to increase the Na⁺/K⁺ influx (Table 3.1) and reduce the Ca²⁺ conductance of H134Q/D156H (Fig. 3.4A). Interestingly, all these mutations could be combined in a synergistic fashion. The obtained quintuple mutant ChR2-5x (E83N/E101D/H114G/H134Q/D156H) showed three times higher photocurrent than E83N/H134Q/D156H, but even lower Ca²⁺ influx (Fig. 3.4B-C). I further compared the Ca²⁺ current between the quintuple mutant and the widely used H134R mutant [14]. At -90 mV and 80 mM Ca²⁺, H134R showed a smaller Ca²⁺ current amplitude than ChR2-5x. However, the small Ca²⁺ influx of H134R might be caused by its relatively low expression level. Moreover, it should be noted that this Ca²⁺ current is measured under a very unphysiological condition. Considering the ion competition effects in ChR2 [76], the physiological abundant Na⁺ and K⁺ will impair the Ca²⁺ influx significantly. Therefore, the high Na⁺/K⁺ conducted ChR2-5x mutant may display a smaller Ca²⁺ influx than H134R under physiology condition. To compare the Ca²⁺ influx of ChR2 variants in oocytes, activation of the oocyte endogenous CaCC was adopted here as an indirect probe (Fig. 3.5D-E). In physiological mimic solution (Ori-standard solution, 2 mM Ca²⁺, pH 7.6), nearly 100% oocytes expressing XXM or H134Q/D156H show activation of CaCC at -70 mV after light illumination. Due to relative low expression and photocurrent amplitude, very few activations of CaCC channel could be observed in H134R expressing oocytes at -70 mV. However, when holding at more negative potentials, clear CaCC activation could be observed from -80 mV and reaches nearly 100% when holding at -120 mV (Fig. 3.4D&F). On the contrary, nearly no activation of CaCC was observed in oocytes expressing ChR2-5x at -120 mV (Fig. 3.4E-F). On the other hand, keeping the holding potential at the physiological level (-70 mV), increasing the Ca²⁺ concentrations in the Ori solution also leads to the enhanced possibility of activating the CaCC. ChR2-5x again shows a smaller Ca²⁺ influx than H134R, as probed by the less activation of CaCC (Fig. 3.4G). Taken together,

I concluded that under physiological condition, ChR2-5x displays much higher photocurrent while with much reduced Ca^{2+} influx than H134R. Considering the relatively low Ca^{2+} concentration under physiological condition (up to 2 mM), ChR2-5x will not induce any non-negligible Ca^{2+} influx. In conclusion, ChR2-5x could be used for faithful depolarization of the cell with negligible Ca^{2+} influx.

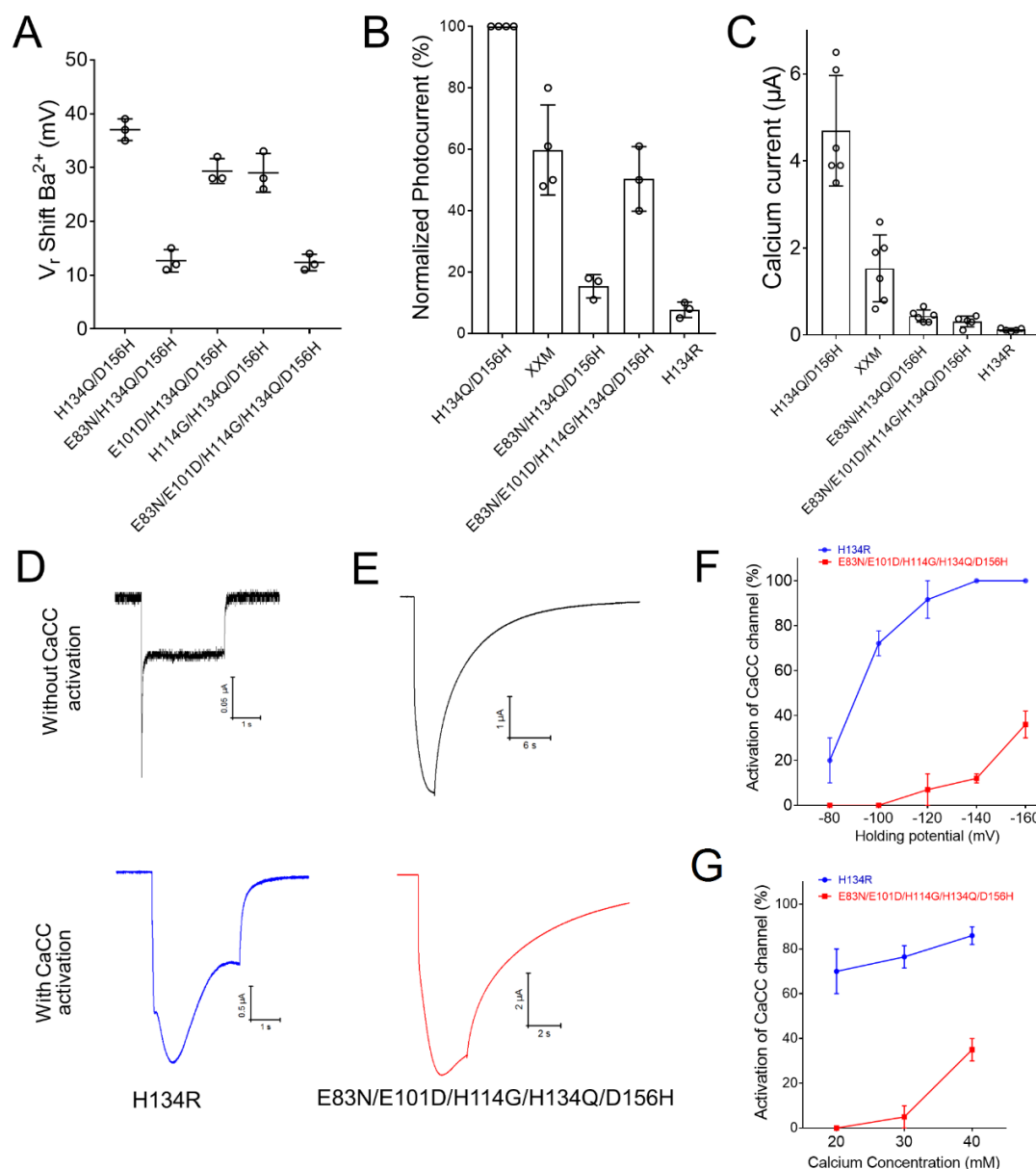


Figure 3.4 Generation of high Na^+/K^+ and low Ca^{2+} conducted ChR2 mutant.

(A) V_r shifts of ChR2 variants showed reduced Ba^{2+} conductance. (B) Photocurrent amplitude comparison of different ChR2 constructs. Holding at -70 mV. Measured in Ori- Ba^{2+} solution at pH 7.6. (C) Calcium current amplitude comparison of different ChR2 constructs. Currents were measured as Fig. 3.1G. (D) Sample photocurrent trace of H134R without (up, black) and with (down, blue) activation of CaCC in oocytes. (E) Sample photocurrent trace of ChR2-5x without (up, black) and with (down, red) activation of CaCC in oocytes. (F) Comparison of CaCC activation in oocytes expressing H134R and ChR2-5x at different holding potential in Ori-standard solution, pH 7.6. (G)

Comparison of CACC activation in oocytes expressing H134R and ChR2-5x at solutions with different Ca^{2+} concentrations. Holding at -70 mV. For (A)-(C), data are presented in Mean \pm SD, n = 3-7. Data in (F) and (G) are shown in Mean \pm SEM, n = 2.

3.2 Optimized photo-stimulation of *NpHR-TYE* for long-term inhibition

Optogenetic reversible silencing of neurons is of great importance in dissecting neural circuits of the brain. Till now, a variety of molecular actuators for neuronal inhibition has been engineered, including light gated chloride channel [79, 80, 101], synthetic two-component potassium channel [138, 139], G-protein coupled receptors [151, 152], and ion pumps [16, 17, 27, 46, 153]. All these silencers have specific biophysical constraints for application. For example, chloride distribution differs in different parts of the cell or different development statuses. Consequently, chloride channels may sometimes lead to cell depolarization instead of hyperpolarization [154, 155]. Light-activated G protein-coupled receptors or synthetic potassium channels exhibit relatively slow kinetic properties. On the contrary, the ion pumps transport ions independent of electrochemical gradients and possess millisecond-range on and off kinetics. The chloride pump *NpHR-TYE* is one of the most popular optogenetic inhibitory tools. One of the main constraints of *NpHR-TYE* is its inactivation upon long-time light illumination. This inactivation refers to photocurrent amplitude decline, probably due to the accumulation of a non-functional intermediate with a deprotonated Schiff base [16, 17, 156]. Few published data suggest that blue light illumination could accelerate the recovery from inactivation of *NpHR-TYE* [16, 17]. Here I systematically studied the inactivation and underlying mechanism of *NpHR-TYE* caused by long time illumination and explored optimized photo-stimulation protocol for long-term inhibition in *Xenopus* Oocyte.

3.2.1 Wavelength-dependent inactivation of *NpHR-TYE*

To quantify the wavelength dependency of *NpHR-TYE*, I performed TEVC recordings from *Xenopus* oocytes expressing *NpHR-TYE*. I first compared *NpHR-TYE* inactivation during long-term (60 s) illumination with light of three different wavelengths: 590 nm, 532 nm and 473 nm. As shown in Fig. 3.5A-C, 590 nm light could induce the highest initial photocurrent amplitudes, but also showed the strongest inactivation when compared to 532 nm or 473 nm light of the same intensity (2.6 mW/mm²). This inactivation of *NpHR-TYE* is also light dose-dependent. Photocurrent inactivation became more prominent with increasing power at 590 nm or 532 nm (Fig. 3.5D). However, no obvious inactivation was observed for 473 nm light at powers up to 6.6 mW/mm² (Fig. 3.5D). After 60 s illumination at 590 nm, *NpHR-TYE* slowly

recovered from inactivation with a weighted time constant of 200 ± 45 s in the dark (Fig. 3.5E-G).

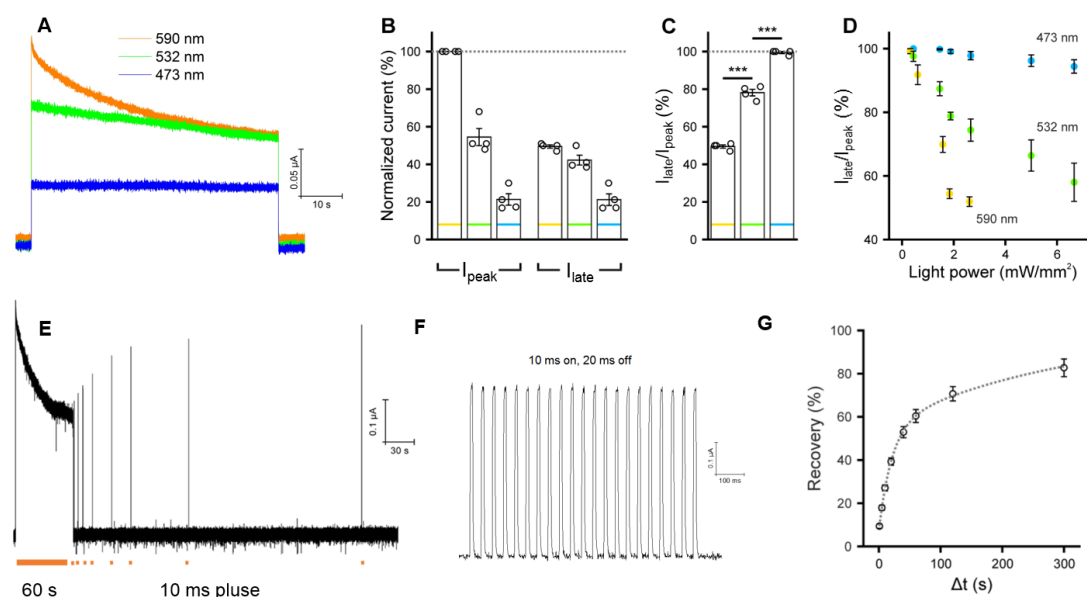


Figure 3.5 Wavelength-dependent inactivation of *NpHR*-TYE in *Xenopus* oocytes. (A) Sample photocurrent traces of *NpHR*-TYE upon stimulation for 60 s at 590 nm, 532 nm or 473 nm at constant intensity (2.6 mW/mm^2). (B–C), Quantification of the initial peak current (I_{peak}), the remaining current at the end of illumination (I_{late}) and the ratio $I_{\text{late}}/I_{\text{peak}}$. (D) $I_{\text{late}}/I_{\text{peak}}$ upon 60 s long illumination at 590 nm, 532 nm or 473 nm at different light intensities ($n = 5$ cells). (E) Sample photocurrent trace of *NpHR*-TYE. Inactivation was induced by a 60 s light pulse at 590 nm (2.6 mW/mm^2). Recovery was probed by 10 ms light pulses (590 nm, 2.6 mW/mm^2) at 1, 5, 10, 20, 40, 60, 120, and 300 s after the initial 60-s illumination. (F) Fast recovery of *NpHR*-TYE from 10 ms irradiation. The photocurrent of *NpHR*-TYE can be fully restored the photocurrent within 20 ms after 10 ms illumination. (G) Quantification of *NpHR*-TYE recovery ($n = 8$ cells). All measurements were performed in Ori-standard solution (pH 7.6) at a holding potential of -40 mV . Data are presented as mean \pm SEM. ***, $P < 0.001$. Asterisks indicate significance levels of *post hoc* t-tests with Bonferroni correction following one-way repeated-measures ANOVA in (C).

3.2.2 Short-wavelength light rescues *NpHR*-TYE from inactivation

I next checked whether recovery can be accelerated by short-wavelength light. Applying light pulses (2 s , 1 mW/mm^2) at either 473 nm or 400 nm could accelerate recovery from inactivation, violet light was found to be significantly more effective (Fig. 3.6A-B). I next examined if short-wavelength light could alleviate *NpHR*-TYE inactivation when co-applied with yellow light. Combination of 590 nm light (2.6 mW/mm^2) with either violet (400 nm , 1 mW/mm^2) or blue (473 nm , 1 mW/mm^2) light shows significant rescue effect (i.e. increase of the $I_{\text{late}}/I_{\text{peak}}$ ratio) and violet light turned out to be more effective (Fig. 3.6C-D). Violet light *per se* evoked very small, if any,

photocurrent ($I_{400}/I_{473} = 6.5 \pm 1.6\%$, $n = 4$ cells). To achieve the optimal function of the *NpHR*-TYE, I next explored the possibility to further increase the amplitude of stable photocurrent via combining green and violet light. Here, the power of 532 nm light was set to 6.6 mW/mm^2 , which led to a similar inactivation as compared to 590 nm light at 2.6 mW/mm^2 when applied separately (Fig. 3.6D). Interestingly, co-application of 1 mW/mm^2 400 nm light and 6.6 mW/mm^2 532 nm light clearly outperformed the combination of 1 mW/mm^2 400 nm and 2.6 mW/mm^2 590 nm for its higher photocurrent amplitudes and the eliminated inactivation effect (Fig. 3.6E–G). In addition, 473 nm light at 6.6 mW/mm^2 alone also evoked stable photocurrents with negligible inactivation during 60 s illumination (Fig. 3.6E–G). However, its photocurrent amplitude was only about 1/3 of the green-violet combination (Fig. 3.6E–G).

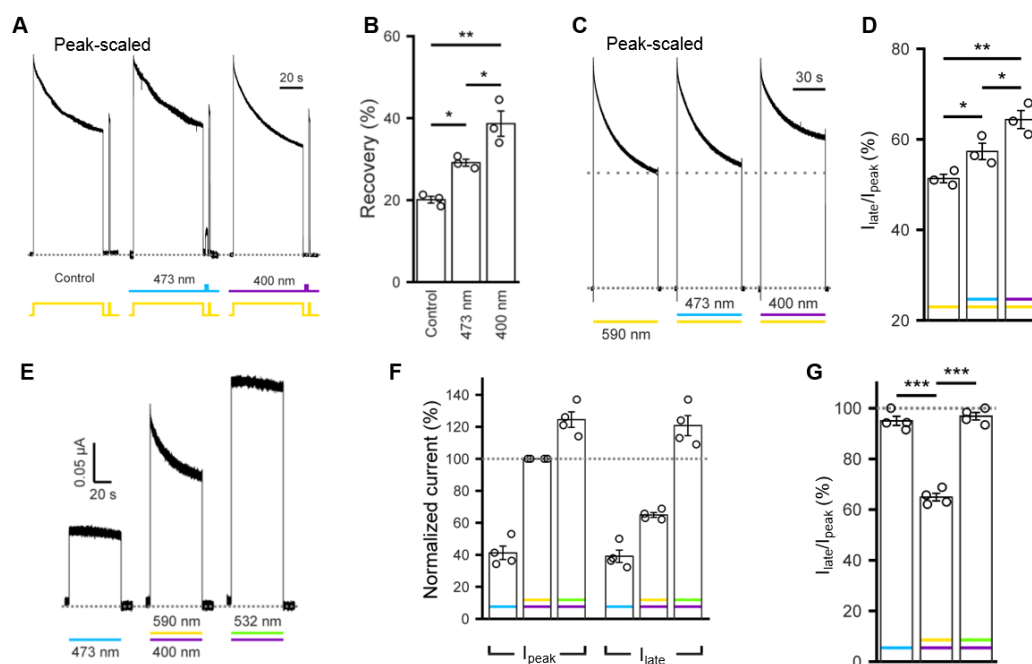


Figure 3.6 Short-wavelength light rescues *NpHR*-TYE from inactivation.

(A) Peak-scaled sample traces from three different cells demonstrating that blue (473 nm) or violet (400 nm) light (2 s, 1 mW/mm^2) accelerates the recovery from inactivation (at 5 s). Note the outward current induced by blue light. (B) Quantification of recovery as in (A). (C) Peak-scaled sample traces from one oocyte illustrating *NpHR*-TYE photocurrents induced by illumination at 590 nm alone (2.6 mW/mm^2) or by co-illumination with either 473 nm (1 mW/mm^2) or 400 nm (1 mW/mm^2). (D) Quantification of $I_{\text{late}}/I_{\text{peak}}$ as in (C). (E) Sample traces from one oocyte illustrating *NpHR*-TYE photocurrents induced by illumination at 473 nm alone (6.6 mW/mm^2), by co-illumination at 590 nm (2.6 mW/mm^2) and 400 nm (1 mW/mm^2) or by co-illumination at 532 nm (6.6 mW/mm^2) and

400 nm (1 mW/mm²). (F–G), Quantification of I_{peak} , I_{late} and $I_{\text{late}}/I_{\text{peak}}$ as in (E). All measurements were performed in Ori-standard (pH 7.6) at a holding potential of -40 mV. Data are presented as mean \pm SEM. * $P < 0.05$, ** $P < 0.01$, *** $P < 0.001$. Asterisks indicate significance levels of *post hoc* t-tests with Bonferroni correction following one-way ANOVA (B) or one-way repeated-measures ANOVA (D) and (G).

3.2.3 Mechanism insight into the inactivation of *NpHR*-TYE

Deprotonation of the Schiff base was suggested to be the reason for the inactivation of *NpHR*, but without any experimental evidence [16, 17, 156]. I therefore first investigated the effect of extracellular pH (pH_{out}) on *NpHR*-TYE inactivation. At higher pH_{out} , the Schiff base can lose the proton more easily. Indeed, increased inactivation was observed when pH_{out} was increased (Fig. 3.7A). Moreover, as the pKa of the Schiff base is strongly dependent on the occupancy of the chloride ion at binding site I of *NpHR* [157], chloride binding to *NpHR* could stabilize the protonated Schiff base. In agreement with this, lower extracellular chloride concentration ($[\text{Cl}^-]_{\text{out}}$) caused stronger inactivation of *NpHR*-TYE (Fig. 3.7B). To gain mechanistic insight into the recovery of *NpHR*-TYE from inactivation (i.e. reprotonation of the Schiff base), I systematically investigated the effects of pH_{out} , $[\text{Cl}^-]_{\text{out}}$ as well as membrane potential on the recovery time constant of *NpHR*-TYE in the dark. The recovery of *NpHR*-TYE from inactivation could be accelerated by either a decrease of pH_{out} (Fig. 3.7C) or an increase of $[\text{Cl}^-]_{\text{out}}$ (Fig. 3.7D). This indicates that the proton for reprotonation of the Schiff base comes from the extracellular space. Interestingly, no significant difference of the recovery time of *NpHR*-TYE at different membrane potentials was observed when $[\text{Cl}^-]_{\text{out}}$ was 121 mM at pH 7.6 (Fig. 3.7E), as membrane potential always has opposite effects on proton and chloride. i.e. a more negative potential will facilitate the proton uptake, however, repulse chloride uptake. Taken together, the data suggest that the proton for the reprotonation of the Schiff base originates from the extracellular side, and its uptake is always facilitated by the binding of chloride, and vice versa.

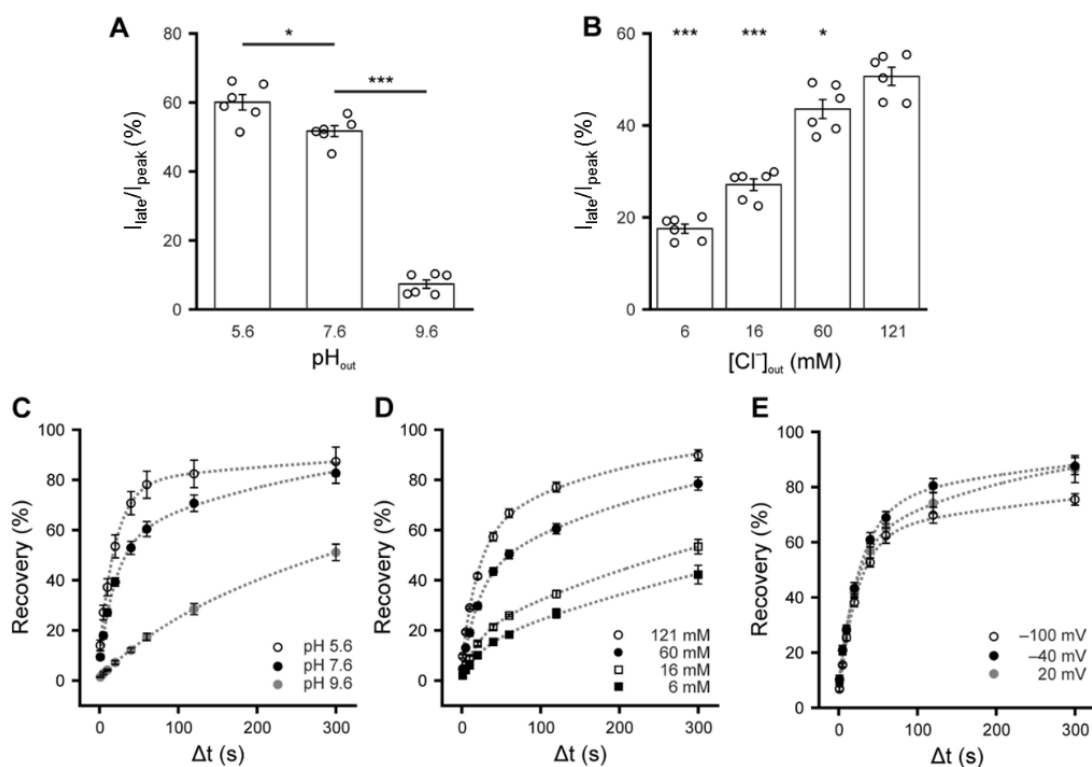


Figure 3.7 Mechanistic insight into the inactivation and recovery of *NpHR*-TYE.

(A) Decreasing extracellular proton concentration enhances inactivation of *NpHR*-TYE. Currents were measured in the same oocyte in Ori-standard solutions at pH 5.6, pH 7.6 or pH 9.6. (B) Increasing extracellular chloride concentration reduces inactivation of *NpHR*-TYE. Currents were measured in the same oocyte at different chloride concentrations. Buffers with different chloride concentrations were achieved by mixing Ori-standard solutions (pH 7.6) and NMG-Asp solution (pH 7.6) at different ratios. (C) Recovery of *NpHR*-TYE-mediated photocurrent in Ori-standard solutions at pH 5.6 ($n = 4$ cells), pH 7.6 ($n = 8$ cells) or pH 9.6 ($n = 4$ cells) at a holding potential of -40 mV. (D) Recovery of *NpHR*-TYE-mediated photocurrents at an extracellular chloride concentration of 6 mM ($n = 5$ cells), 16 mM ($n = 6$ cells), 60 mM ($n = 6$ cells) or 121 mM ($n = 5$ cells). pH was set to 7.6 and holding potential to -40 mV. Dotted lines in (C) and (D) represent bi-exponential fits to population data. (E) Recovery of *NpHR*-TYE (pH 7.6) at holding potentials of -100 mV ($n = 7$ cells), -40 mV ($n = 5$ cells), or $+20$ mV ($n = 5$ cells). 590 nm light at intensity of 2.6 mW/mm² was applied for 60s in (A) and (B); while in (C)-(E), additional of 10 ms 590 nm light pluses at same intensity were delivered at 1, 5, 10, 20, 40, 60, 120, and 300 s after the initial 60 s illumination, as in Fig. 3.7E. Data are presented as mean \pm SEM. * $P < 0.05$, *** $P < 0.001$. (A) and (B), Asterisks indicate significance levels of *post hoc* t-tests with Bonferroni correction following one-way repeated-measures ANOVA.

3.2.4 Proposed photocycle of *NpHR*

Based on the above data, here we proposed the photocycle model of *NpHR*. At rest state, an extracellular chloride ion is bound to the Schiff base with $K_m = 16$ mM [16]. The normal chloride pumping photocycle triggered by photon absorbance of ATR. After light illumination, retinal isomerization starts the photocycle containing a

sequential intermediates K, L, N and O with different absorbances. The chloride ion is released into the cytosol during the transition between N to O and re-uptake from the extracellular half in the recovery from O to initial state (Fig. 3.8). In parallel, *Np*HR without bound chloride ion may undergo a branched photocycle. Without chloride binding, the Schiff base is prone to deprotonated, leads to formation of M intermediate. This M intermediate is stable and absorbs similar to H₄₁₀ in *Hs*HR or M₄₁₂ in BR. Protons for reprotonation of the M intermediate comes from the extracellular side but its uptake in dark is very slow. Blue light absorbance could significantly accelerate this turnover (Fig. 3.8).

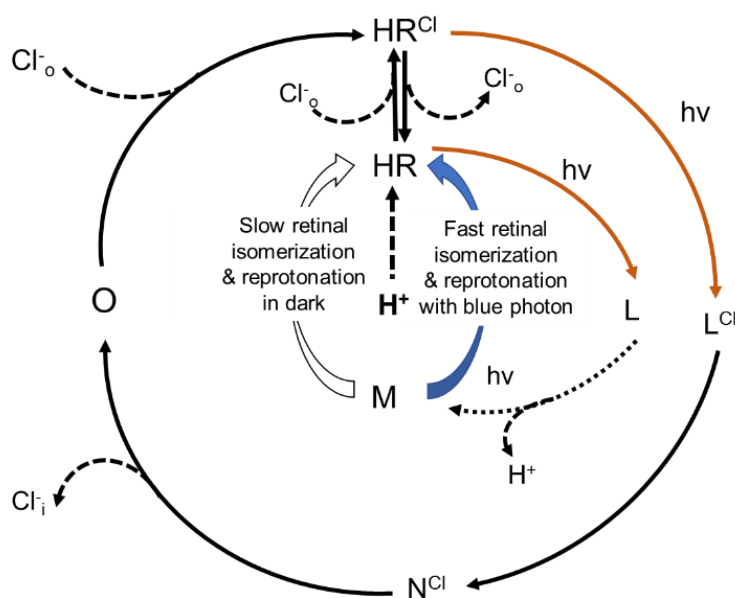


Figure 3.8 Proposed Photocycle of *Np*HR.

An extracellular chloride ion is bound to the Schiff base lysine of *Np*HR at resting state, with $K_m = 16$ mM [16]. Photon absorption (with maximum at 580 nm) triggers the isomerization of retinal and starts the photocycle, containing intermediates K (omitted here), L, N, and O. The chloride ion is released into the cytosol during the transition from N to O and uptake of a chloride ion from the extracellular side takes place in the recovery from O to the initial state. HR without a bound chloride ion is prone to deprotonation of the Schiff base in the L state (indicated by the dashed line), leading to formation of M. This intermediate is long-lived and absorbs similarly as HR₄₁₀ (or M₄₁₂ in BR) from *Halobacterium salinarum*. The uptake of the proton for reprotonation of the M intermediate is very slow in dark (open arrow) but fast after absorption of a blue photon (blue arrow). Our data support deprotonation of the chloride-free L state (indicated by broken line).

3.2.5 Blue-light induced photo-stimulation of *Np*HR-TYE enables efficient long-term hyperpolarization and inhibition in brain slices

Chuanqiang Zhang (from Uni-Jena) further tested whether the superior properties of photo-stimulation scheme using short-wavelength light found in voltage-clamp

experiments could be translated into a higher efficiency of long-term neuronal inhibition. Blue light illumination was selected over the green-violet combination as the optimized photo-stimulation protocol, as using multiple wavelengths might be a potentially complicating factor in in-vivo applications (see details in Discussion 4.2.2). Current-clamp measurements from CA1 pyramidal cells in acute brain slices of mice were performed. Repetitive 1 s current injections via the patch pipette were used to trigger AP firing in the presence of ionotropic glutamate and GABA receptor antagonists (Fig. 3.9A). Photo-stimulation of NpHR-TYE with yellow light (594 nm) for 1 min rapidly suppressed the AP firing in the first test pulse but failed to inhibit the rest AP firing during prolonged photo-stimulation periods (Fig. 3.9B). In contrast, irradiation by blue light (488 nm) reliably inhibited AP discharge during the entire 1 min illumination period (Fig. 3.9C). In conclusion, illumination with yellow light resulted in a pronounced, but transient hyperpolarization, whereas blue light stimulation induced a highly stable hyperpolarizing response in both tested cells (oocytes and neurons).

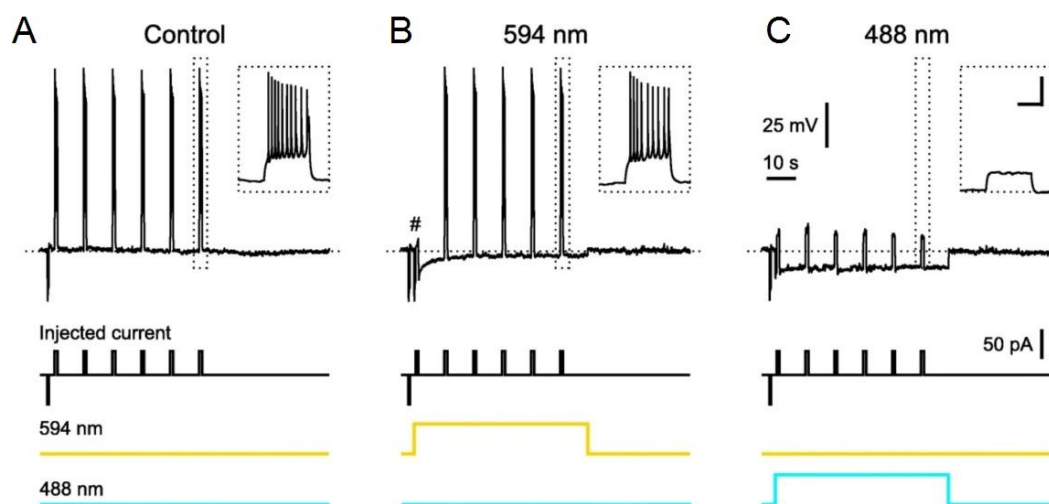


Figure 3.9 Optimized photo-stimulation (blue) scheme of *NpHR-TYE* enables long-term neuronal inhibition.

Sample current-clamp measurements from a single cell (biased to about -65 mV at rest) repetitively challenged with an inward current of constant amplitude either without (A) or with illumination by 594 nm (B) or 488 nm (C), respectively. Note that 594 nm stimulation initially abolished AP firing (#), which recovered during prolonged illumination periods. Blue-light irradiation suppressed AP firing for the entire 1 min period on the background of a stable hyperpolarization. Insets: current responses to the last test pulse at higher temporal magnification. Experiments were performed by Chuanqiang Zhang from Uni-Jena. Figures are modified from [158].

3.3 Optogenetic tools for cAMP manipulation

3.3.1 Engineering photoactivated adenylyl cyclase for cAMP manipulation

As an important second messenger, cAMP plays vital roles in cells by activating certain types of ion channels, cAMP-dependent protein kinase A (PKA), exchange protein activated by cAMP (Epac) [159] or cAMP response element-binding protein (CREB) [160]. cAMP signaling is proven to be precisely regulated in a confined microscale, by the help of specific subcellular localized PDEs and ACs [161]. Accordingly, to study the role of cAMP in a specific physiology event, high subcellular spatial and temporal precision of cAMP manipulation is needed. The optogenetic intervention of cAMP signaling is therefore increasingly popular. Continuously expanding optogenetic toolbox offers multiple choices for cAMP manipulation. Selecting the optimum tool is a crucial first step for every optogenetic study. In this study, I developed a fast and reliable *in-vitro* method to quantify the enzymatic activity of different PACs after expression in *Xenopus* oocyte. Among, bPAC remains the best tool for cAMP manipulation for its high light activity and high dynamic range. However, a residual activity in the dark is unwanted and the cytosolic localization prevents subcellular precise cAMP manipulation. Point mutations were therefore introduced into bPAC to reduce its dark activity. In addition, I found that membrane targeting of bPAC via different linkers can remarkably alter its activity, in addition to its localization. Engineered membrane-bound bPAC with reduced dark activity is well-tolerated by hippocampal neurons and reliably evokes a transient photocurrent when a CNG channel is co-expressed.

3.3.1.1 Development of an *in-vitro* assay for characterization of PACs

Xenopus oocyte has been successfully used for characterizing photoactivated enzymatic membrane proteins BeCyclOp [125], RhopDE [129] and 2c-CyclOp [131]. With the help of a fluorescence emission-based protein quantification method, the *Xenopus* oocyte system allows us to characterize the enzyme activity fast and accurately without time-consuming protein purification process.

For soluble proteins, reliable quantification of the enzymatic activity (especially the dark activity) requires elimination of the possible influences from other components in the crude soluble protein extracts. I therefore performed dialysis by using an ultra-centrifugal filter tube, which allows removing the small proteins, the nucleotidyl cyclase substrates ATP/GTP, the accumulated cAMP/cGMP and other small molecules

(such as some metal ions) that might influence the nucleotidyl cyclase activity. However, due to the relatively high molecular weight, the endogenous PDEs cannot be removed from the crude soluble extracts by ultra-centrifugal filters. To quantify the possible endogenous PDEs activity, cAMP was added into the soluble extracts and measured at different time points in the presence and absence of 1 mM IBMX. cAMP degradation was fully blocked in control oocyte soluble extracts by 1 mM IBMX (Fig. 3.10A). Clear differences of cAMP production from eYFP-bPAC in dark were also observed between with and without adding IBMX (Fig. 3.10B), which is equivalent to the PDEs activity detected in Fig. 3.10A. Therefore, the PDEs activity in the soluble bPAC extracts was fully blocked by IBMX, ensuring reliable measurement of bPAC dark activity. Under light illuminated condition, no difference of cAMP level can be detected between with and without IBMX (Fig. 3.10C), as the light activity of bPAC is way stronger than the endogenous PDEs activity.

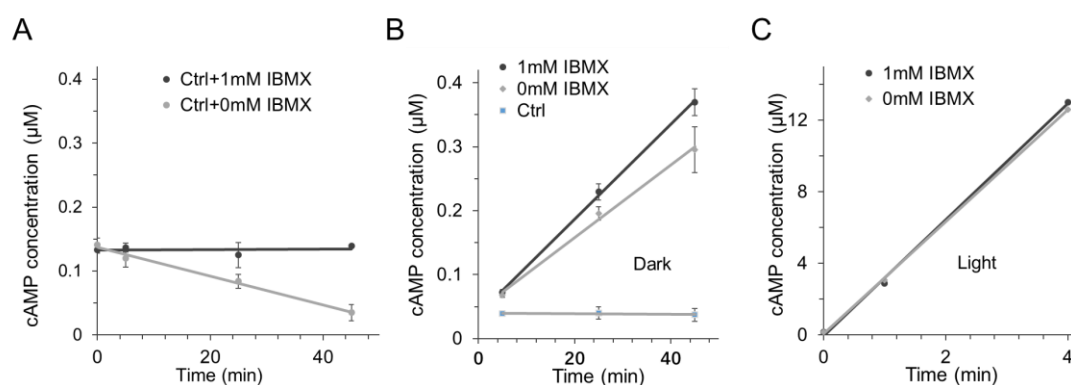


Figure 3.10 Blocking the PDEs activity in *Xenopus* oocyte intracellular fluid after dialysis.

Samples were prepared according to Method 2.7. (A) For control oocytes, the reactions were started by adding additional cAMP into the reaction buffer in the absence or presence of 1 mM IBMX. For eYFP-bPAC expressing oocytes, the reaction under dark condition (B) or blue light (473 nm, 65 $\mu\text{W}/\text{mm}^2$) illuminated condition (A) were started by adding ATP (to final concentration at 1 mM) and GTP (to final concentration at 0.2 mM) in the absence or presence of 1 mM IBMX. Data are shown as means \pm SEM, $n = 3$.

I further characterized the light sensitivity of eYFP-bPAC to blue light (473 nm) using this assay. After illumination by 473 nm light with different intensity, the half-saturated light intensity of eYFP-bPAC is determined to be 28.5 $\mu\text{W}/\text{mm}^2$ (Fig. 3.11A), very similar to bPAC without eYFP tag (26.4 $\mu\text{W}/\text{mm}^2$) (Fig. 3.11B), indicating that eYFP tag does not influence the light sensitivity of bPAC. Applying 500 ms light flash to bPAC, cAMP level continuously increases in the dark with a time-constant of 7.5 s (Fig. 3.11C).

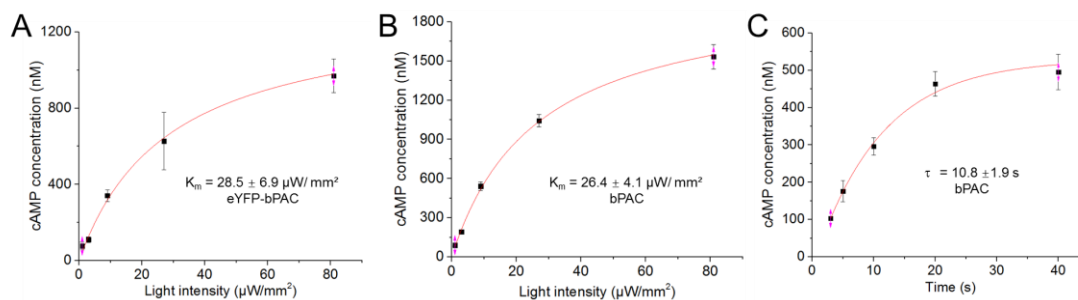


Figure 3.11 Characterization of bPACs from *Xenopus* oocyte intracellular fluid after dialysis cAMP production by eYFP-bPAC (A) or wt-bPAC (B) at different light (473 nm) intensity. Plotted are mean values with S.D. and fitted by a Michaelis-Menten curve (red) with K_m value. (C) cAMP concentrations at different time delays in the dark after 500 ms 473 nm light pulse. Plotted are mean values with SD and an exponential fitting curve (red), yielding a tau value of 10.8 s.

3.3.1.2 Comparison of different PACs

I next applied this *in-vitro* assay to quantify the activities of soluble PACs. These PACs were fused with an eYFP tag either at N- or C- terminal for quantification of protein level by the eYFP fluorescence emission value. The turnover of eYFP-bPAC in the dark is determined to be $\sim 0.057 \text{ min}^{-1}$ while in the light it is $\sim 93 \text{ min}^{-1}$ (Table 3.2). The eYFP-bPAC light activity here, 93 min^{-1} (1.6 s^{-1}), is close to the bPAC activity (2.6 s^{-1}) detected by Lindner et al. [117] and SUMO-bPAC (1.8 s^{-1}) activity detected by Stierl et al. [116]. Fusion of the eYFP tag to the C terminus of bPAC shows no obvious influence of its activity (Table 3.2). The L/D ratio (light activity/dark activity) is about ~ 1600 for both eYFP-tagged bPAC constructs (Table 3.2). The EuPAC α -eYFP displays 6 times higher dark activity than bPAC-eYFP but lower light activity, resulting in the L/D ratio at 180 (Table 3.2). The position of eYFP tag affects the EuPAC α light activity. Changing eYFP to the N terminus leads to 6 times reduction of light activity in comparison with EuPAC α -eYFP, while the dark activities are similar (Table 3.2). The L/D ratio of mPAC has been reported to be 30 [121]. Here I found mPAC shows 30 times higher dark activity, while only about half activity in light when compared to bPAC, confirming its L/D ratio. No activity of LiPAC can be detected in our system (Table 3.2). TpPAC has slightly lower dark activity than bPAC but 18 times lower light activity with a L/D ratio of 150 (Table 3.2). Overall, bPAC remains the best optogenetic tool for cAMP manipulation, for its highest L/D ratio among these tested PACs and relatively low dark activity. In addition, our assay could also be used to characterize the

bPAC guanylate cyclase mutant bPGC. The bPGC catalyzes the synthesis of cGMP in both dark and light states, with a ratio of ~200 (Table 3.3). Residual AC activity could still be detected in bPGC under light illuminated condition, but only 1/10 of the cGMP producing ability (Table 3.3).

Table 3.2 Enzymatic activity of different PACs

	Dark turnover (min ⁻¹)	Light turnover (min ⁻¹)	L/D
bPAC-eYFP	0.057 ± 0.015	93 ± 9	~ 1600
eYFP-bPAC	0.055 ± 0.01	91 ± 8	~ 1600
EuPAC α -eYFP	0.38 ± 0.06	67.6 ± 9.1	~ 180
eYFP-EuPAC α	0.35 ± 0.08	11.9 ± 1.6	~ 35
mPAC-eYFP	1.55 ± 0.4	43.3 ± 5.5	~ 30
LiPAC-eYFP	< 0.0012	< 0.0012	-
eYFP-LiPAC	< 0.0012	< 0.0012	-
TpPAC-eYFP	0.033 ± 0.006	5 ± 0.6	~ 150
eYFP-TpPAC	0.04 ± 0.007	4 ± 0.4	~ 100

Reaction buffer: 75 mM Tris-HCl, pH 7.4, 100 mM NaCl, 5 mM DTT, 5 mM MgCl₂, 1 mM ATP, 0.2 mM GTP, Data are present as mean ± SD, n = 3

Table 3.3 Enzymatic activity of different bPGCs

	cGMP turnover (min ⁻¹)			cAMP turnover (min ⁻¹)		
	Dark	Light	L/D	Dark	Light	L/D
bPGC-eYFP	0.009 ± 0.001	1.9 ± 0.29	211	Not detectable	0.18 ± 0.02	-
Gly-eYFP-bPGC	Not detectable	0.38 ± 0.046	-	Not detectable	0.46 ± 0.008	-

Reaction buffer: 75 mM Tris-HCl, pH 7.4, 100 mM NaCl, 5 mM DTT, 5 mM MgCl₂, 0.1 mM ATP, 0.1 mM GTP, Data are present as mean ± SD, n = 3

3.3.1.3 Reducing the dark activity of bPAC by mutations

Although superior to EuPAC, mPAC and TpPAC etc., bPAC still shows dark activity in optogenetic applications. Slight cAMP accumulation occurs in the absence of light [112, 113] and bPAC expressing *Dictyostelium discoideum* cells displayed delayed development in the dark [162], indicating that bPAC has nonnegligible dark

activity. Similarly, I also observed obvious cAMP accumulation in the dark when expressing bPAC in *Xenopus* oocyte (Fig. 3.12A). I therefore tried to reduce the dark activity of bPAC by introducing point mutations. Clearly, bPAC activities could be affected by mutations in the FAD binding center, the structural transition site and the catalytic center. Mutating S27 in the FAD binding center to alanine generated a spectrum red-shifted bPAC variant with 40% reduced dark activity [116]. The dimerization of bPAC is mainly mediated by the $\alpha_{3\text{BLUF}}$ helix of each chain. The C-terminal capping helices are essential for signal transduction and provide a link between the BLUF and AC. Extensive interactions between the two $\alpha_{3\text{BLUF}}$ were observed in the structure of bPAC [117], suggesting the interactions between these two helices is the prerequisite for empowering bPAC catalytic activity. Therefore, modifying the orientation between these two helices may directly affect the dark activity of bPAC. I designed mutations to alter the interactions between two helices, aiming to change the bPAC activity. L123R might strengthen the interactions, for the potential formation of a salt bridge with E124* (E124 in the other chain of the bPAC dimer). This indeed reduced the dark activity. However, it also nearly abolished the light activity (Fig. 3.12A). While L123C, which may form a disulfide bond between two mutated cysteine residues also displayed reduced dark activity [117].

Sequence alignment has revealed the catalytic residues in bPAC [110]. Conserved K197, D201 and R278 in the catalytic domain were first selected for mutagenesis. K197A and R278A mutants are still photoactivable and showed no cAMP accumulation in the dark when expressing in *Xenopus* oocytes, while the K197A/D201A double mutant abolished both the dark and light activity (Fig. 3.12A). The dark activities of K197A and R278A were determined to be 0.0066 min^{-1} and 0.0012 min^{-1} , respectively, which corresponded to 10% and 2% of the wt-bPAC dark activity (Table 3.4). However, the L/D ratio of K197A was reduced to 400 while R278A was still close to wt-bPAC (Table 3.4). Structural analysis revealed that accessibility of ATP to the binding residue K197 was affected by the residue F198*. In the dark state, the side chain of K197 interacts with the carbonyl oxygens of F198* and H266. Light stimulation would free K197 from F198* to bind the substrate ATP. Simply, mutating F198 to a residue with increased size might further block the access of ATP to K197, which would lead to reduced dark activity. As speculated, F198Y and F198W indeed reduce the dark activity of bPAC in a size-dependent manner (Fig. 3.12A). However, H266W mutant still showed cAMP accumulation in dark. T267 is another major determinant of base

specificity. Hence, point mutation should also influence activity. However, T267Y mutant abolished both the dark and light activity (Fig. 3.12A). Compared with other mutants, F198Y still preserves relatively good light activity and shows the highest L/D ratio (Table 5.3). Moreover, F198Y displays a favorable faster photocycle and thus a shorter cAMP production “spurts” in comparison with wt-bPAC (Fig. 3.11C & 3.12B), rendering F198Y the most promising mutant.

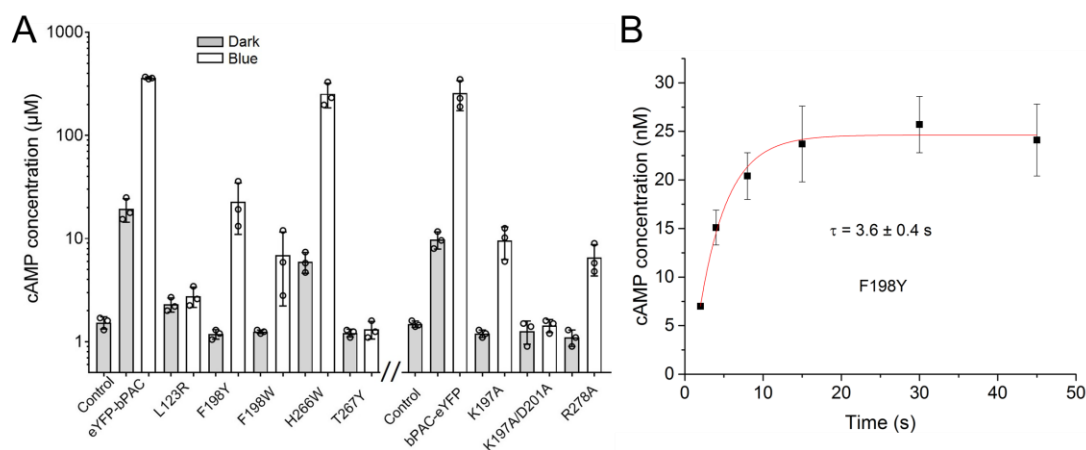


Figure 3.12 Generation and characterization of bPAC mutants with reduced dark activity. (A) Oocytes expressing different bPAC constructs were incubated in ND96 solution for 3 days in dark. Samples were either always kept in dark or illuminated with blue light (473 nm, 0.3 mW/mm²) for 30 s. All bPAC mutants were tagged with eYFP, either at the N-terminal (for L123R, F198Y, F198W, H266W and T267Y) or at the C-terminal (K197A, K197A/D201A and R278A). 30 ng cRNA (for all bPAC variants) was injected into each oocyte. cAMP concentration was quantified by Elisa assay. Data are present as mean \pm SD, n = 3. (B) cAMP concentration at different time delays in the dark after 500 ms 473 nm light pulse. Plotted are mean values with S.D. and an exponential fitting curve (red), yielding a tau value of 3.6 s. Data are present as mean \pm SD, n = 3.

3.3.1.4 Altering bPAC activity via membrane targeting

As a soluble protein, bPAC is easy to be modified for different subcellular targeting. I then tested fusing bPAC to other membrane proteins such as ArcB, BmPR, CD8, and Glycophorin A. All these constructs have an eYFP in between the membrane anchor and bPAC. Interestingly, the obtained constructs, i.e. ArcB-eYFP-bPAC, BmPR-eYFP-bPAC, CD8-eYFP-bPAC and Gly-eYFP-bPAC, showed no cAMP accumulation in dark but significant cAMP production after blue light illumination (Fig. 3.13A-B), suggesting the reduced dark activity of these membrane-bound constructs. Accurate dark and light activities were then determined by using the oocytes membrane assay (see details in Methods 2.7 and 2.8). The dark activity of the four constructs are all reduced dramatically (Table 3.4). Gly-eYFP-bPAC shows the lowest dark activity and the highest L/D ratio among the four constructs. Similarly, fusing bPGC to Glycophorin A with an eYFP in between also reduces its dark activity to non-detectable level and

light activity to 0.4 min^{-1} (Table 3.3). Fusion of the opsin domain (the first 425 aa) of BeCyclop with bPAC-eYFP also reduced the dark activity of bPAC (Table 3.2 & Fig. 3.13C-D). Interestingly, the light activity of bPAC-eYFP-BeRho-E was increased to 2 folds by the addition of ATR, suggesting the light-induced conformational change of BeRho could also influence the cyclase activity of bPAC.

Aside from fusion with type I membrane anchors, bPAC could also be targeted to different positions by fusing with short signal peptides or anchor peptides such as the membrane anchor peptide (MGCIKSKGKDS) from tyrosine kinase Lyn (Lyn11) [163]. Short membrane targeting peptides are of great value for host systems requiring AAV transfection. I tested the Lyn11-bPAC (named as bPAC-PM in [163]) construct in the *Xenopus* oocyte and found highly accumulated cAMP in dark (Fig. 3.13E). However, after insertion of eYFP protein between Lyn11 and bPAC, no obvious cAMP accumulation can be observed in dark (Fig. 3.13E). *In-vitro* membrane assay also confirmed the reduced dark activity of Lyn-eYFP-bPAC (Table 3.4). In addition, we find that an extra repeat of Lyn11 in the N terminal which generates a 2xLyn11-eYFP-bPAC increases the expression level (Fig. 3.13F) without influencing the bPAC character (Table 3.4). Similarly, direct fusing bPAC to 2xLyn11 or Glycophorin A also caused obvious cAMP accumulation in dark. Insertion of eYFP protein in between reduced the dark activity (Fig. 3.13E & Table 3.4). In conclusion, here I found that the linker region between membrane anchor and bPAC can remarkably alter its activity, in addition to its localization.

3.3.1.5 Generating membrane-anchored bPAC with no dark activity

In principle, membrane targeting and point mutation could be integrated together to further reduce the dark activity of bPAC. Indeed, a variety of constructs with different activities were generated via different combinations of membrane anchors and point mutations (Table 3.4). Particularly, combining F198Y mutation with 2xLyn11, I obtained a plasma membrane-targeted bPAC with no dark activity but still relatively good light activity (Table 3.4). The 2xLyn11-eYFP-bPAC-F198Y was named bPAC-PM 2.0 for short as developed from bPAC-PM (Lyn11-bPAC).

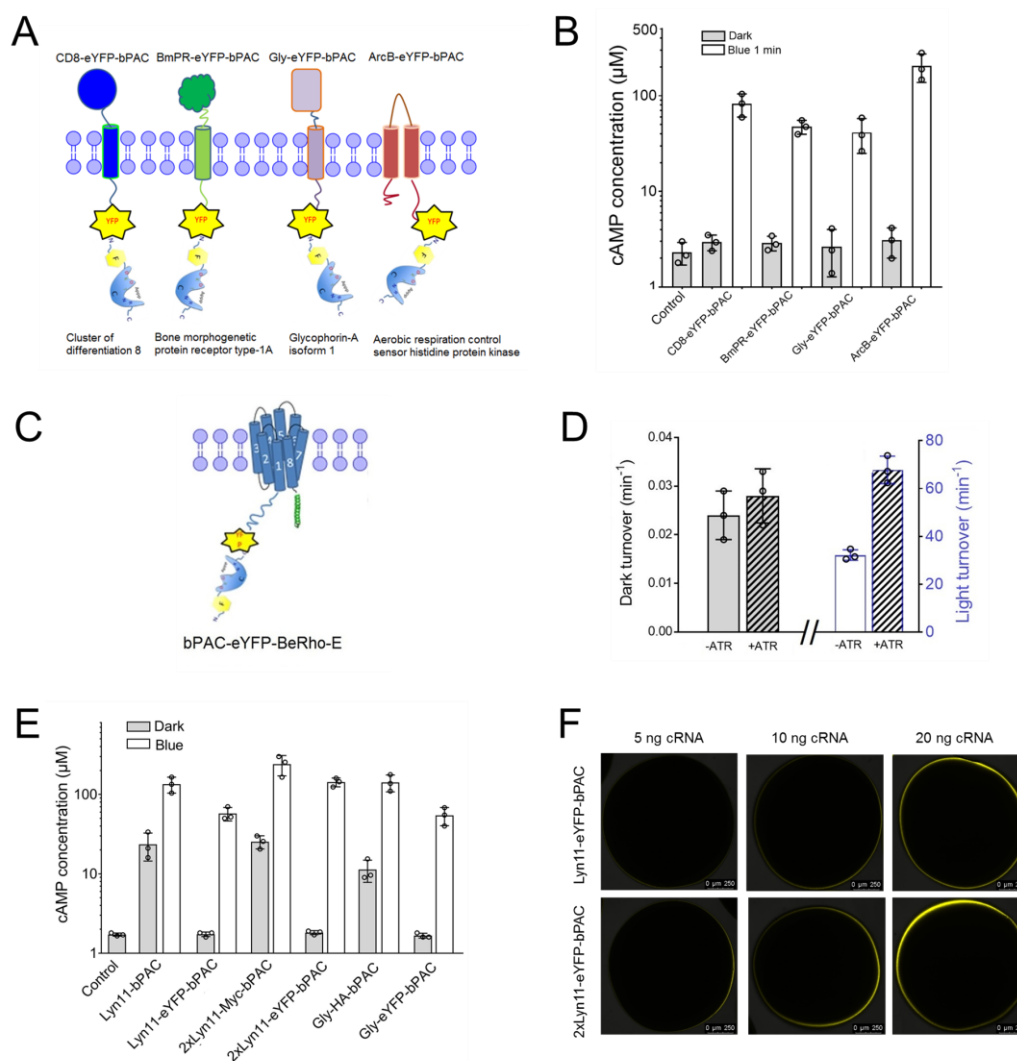


Figure 3.13 Altered activity of bPAC via membrane anchoring.

(A) Scheme of bPAC constructs fusion with different membrane anchor. (B) Membrane-bound PAC shows no cAMP accumulation in dark, and still shows light activation for cAMP production. (C) Scheme of bPAC-eYFP-Berho-E, generated by fusing bPAC-eYFP to the opsin domain of BeCyclOp at the N- terminal. (D) Adding additional ATR shows no influence on the dark bPAC-eYFP-Berho-E, but increases its light activity. (E) The linkers between bPAC and the membrane anchors alter the activity of bPAC. (F) 2Lyn11-eYFP-bPAC shows higher expression level than Lyn11-eYFP-bPAC. Images were obtained via confocal microscopy with indicated bar. All data are shown in Mean \pm SD, $n = 3$.

Table 3.4 New PACs with reduced dark activity

	Dark turnover (min^{-1})	Light turnover (min^{-1})	L/D
bPAC-eYFP-K197A	0.0066 ± 0.0006	2.6 ± 0.5	400
bPAC-eYFP-R278A	0.0012 ± 0.0003	1.6 ± 0.3	1300
eYFP-bPAC-F198Y	≤ 0.0024	17 ± 0.8	≥ 7000
ArcB-eYFP-bPAC	0.013 ± 0.005	24.2 ± 3.6	1850
BmPR-eYFP-bPAC	0.0082 ± 0.002	15.1 ± 0.5	1850

CD8-eYFP-bPAC	0.011 ± 0.0015	16.8 ± 2.0	1500
Glyco-eYFP-bPAC	0.0076 ± 0.0012	17.5 ± 3.4	2300
Lyn11-eYFP-bPAC	0.014 ± 0.003	18.2 ± 2.3	1300
2xLyn11-eYFP-bPAC	0.013 ± 0.003	16.9 ± 2.4	1300
Gly-eYFP-bPAC-S27A	0.0051 ± 0.0002	15 ± 0.6	2900
CD8-eYFP-bPAC-R278A	Not detectable	0.52 ± 0.17	-
Gly-eYFP-bPAC-R278A	Not detectable	0.51 ± 0.05	-
2xLyn11-eYFP-bPAC-F198Y	Not detectable	2 ± 0.3	-
eYFP-biPAC	0.016 ± 0.002	36 ± 8	2300
2xLyn-eYFP-biPAC	<0.012	15 ± 4.7	>1200

Reaction buffer: 75 mM Tris-HCl, pH 7.4, 100 mM NaCl, 5 mM DTT, 5 mM MgCl₂, 1 mM ATP, 0.2 mM GTP, Data were present as mean ± SD, n = 3

3.3.1.6 Neural application

bPAC-PM 2.0 was then tested in hippocampal neurons by Oana Constantin (colleague in Uni-Hamburg). The confocal images showed that bPAC-PM 2.0 mainly localized on the plasma membrane, despite formed some intracellular aggregates (Fig. 3.14A). Still, the neurons expressing bPAC-PM 2.0 seemed very healthy, judged by the normal morphology feature. Moreover, the bPAC-PM 2.0 transfected neurons remained well responses to somatic current injection, further proving the well-tolerance of bPAC-PM 2.0 in hippocampal neurons (Fig. 3.14B). The non-detectable dark activity of bPAC-PM 2.0 was also confirmed in neurons. Adding IBMX showed very tiny, if any, changes in the holding current of neurons expressing the mCNG-A2 alone (Fig. 3.14C). Significant holding current change was observed only in neurons co-expressed with bPAC, not bPAC-PM 2.0 (Fig. 3.14D-E), indicating the obvious dark activity of bPAC and the eliminated dark activity of bPAC-PM 2.0. More importantly, reliable transient photocurrent could be evoked by blue light in neurons co-expressing of bPAC and mCNG-A2 (Fig. 3.14F). Taken together, bPAC-PM 2.0 shows superior properties in neurons.

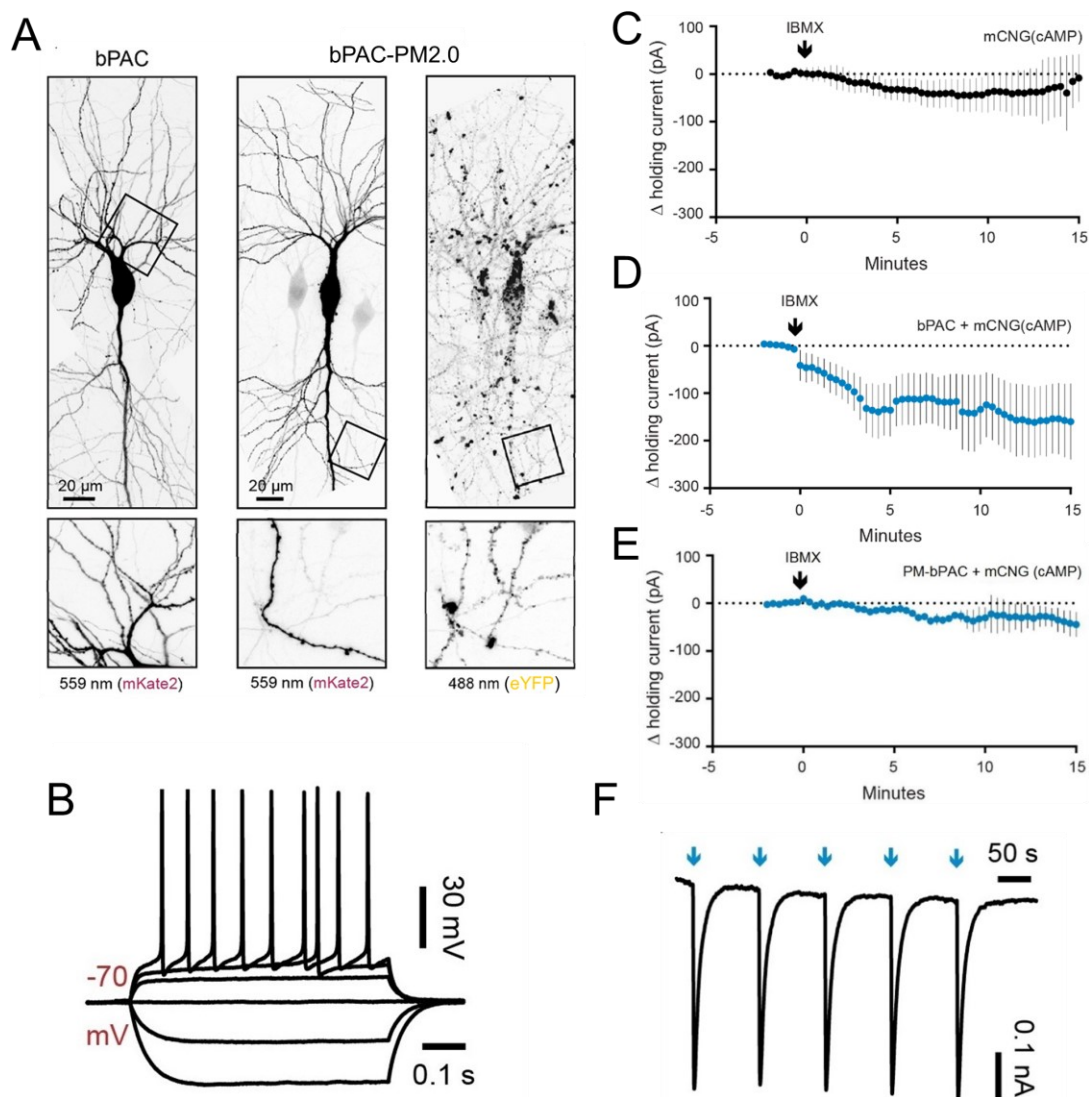


Figure 3.14 Characterization of PM-PAC2.0 in rat hippocampal neurons.

(A) Confocal images of hippocampal neurons expressing bPAC (left) or bPAC-PM 2.0 (middle), together with mKate2. Distribution of bPAC-PM 2.0 in neuron (right). (B) Whole-cell responses to somatic current injections from -400 pA to 700 pA in a bPAC-PM 2.0 expressing neuron. Changes in the holding current generated by the wash-in of IBMX of neurons expressing either the mCNG-A2(cAMP gated channel) alone (C) or together with bPAC (D) or bPAC-PM 2.0 (E). (F) Photocurrents evoked by five consecutive light flashes in a bPAC-PM 2.0 expressing neuron. Figure from Oana Constantin and Christine Gee in Hamburg.

3.3.2 New photoactivated adenylyl cyclase, biPAC

We also explored the database and found another PAC (Accession No. OQW94152) from *Beggiatoa* sp. IS2. We synthesized it and named it as biPAC. biPAC shares very high sequence identity with bPAC, including the signature motifs of BLUE domain and type III AC domain (Fig. 3.15). I then tested the AC activity of biPAC both in dark and

in light. As expected, eYFP-biPAC showed very strong light activation in synthesizing cAMP with the L/D ratio of 2300 (Table 3.4), in a similar range with bPAC. The dark activity of eYFP-biPAC is much lower (~ 30%) than eYFP-bPAC, which is a valuable feature for optogenetic application. The slightly reduced light activity can be easily compensated by prolonging the illumination time. Considering the high sequence similarity, the dark activity reducing mutations identified in bPAC could, in principle, be adopted into biPAC to further decrease its dark activity.

```

biPAC      -MKRITYISW-ANDLSPKQIQQIREVSVKNNNSYNGITGVLLCLKGLFFQILEGDGERVDK 58
bPAC      MMKRLVYISKISGHLSEELIQRIGKVSIKNNQRDNITGVLLYLQGLFFQILEGENEKVDK 60
          **:. ** . . ** ::**: * :**:**. . ***** *:*****:*. **

biPAC      LYEKILVDERHRDILCLKTELDVTEKMFDPDWGMKTINLDEQEGIILEPIKSLLFRTIAESH 118
bPAC      LYKKILVDDRHTNILCLKTEYDITDRMFPNWAMKTINLNENSELMIQPIKSLLTITQSH 120
          **:*****:** :***** *:**:*:**:*. *****:*. . :**:***** **:**

biPAC      RILEKYTQPSVINIITQGIDPLTVAPHIVEKIIFFSDIVSFSTFSEKLPVDKVVNLVNHY 178
bPAC      RVLEKYMPARVIYLINQGINPLTVEPQLVEKIIFFSDILAFSTLTEKLPVNEVVILVNR 180
          *:*** * * :*. **:*:** * :*****:*****:*****:*****:*** **:*

biPAC      LTICTEII SAHGGEVIKFIGDCVMAGFSTNQADAAISTGLEILAELKSLRELTEVNDPLH 238
bPAC      FSICTRIISAYGGEVTKFIGDCVMASFKEQGDAAIRSLDIISELKQLRHVHEATNPLH 240
          :.***. *****:***** ******. * . :*. ***** * :*:*:**. ** . * . :***

biPAC      FLYTGIGLSCGNVIEGNIGSPVKMDYTLGDAVNVASRLEALSRLPYSMILSTEVKNYC 298
bPAC      LLYTGIGLSYGHVIEGNMGSSLKMDHTLLGDAVNVAARLEALTRQLPYALFTAGVKKCC 300
          :***** * :*****:** :***:*****:*****:*****:*****: :** ** *

biPAC      CTPWSFINLGRHQMKGKQTLVEIFAINDSIVRKSSDASQIANFIAQALDMIAPKQIK 356
bPAC      QAQWTFINLGAHQVKGKQEAIEVYTVNEAQK--YYDTLQITQLIRQTLENDK----- 350
          : * :***** ** :*** * :*:*:**: * : **:*:** **:*

```

Figure 3.15 Sequence alignment of bPAC and biPAC.

The newly identified putative PAC from *Beggiatoa sp. IS2* was named to biPAC by us. biPAC shares very high sequence identity with bPAC, suggesting the photoactive property and AC activity.

3.3.3 Engineering rhodopsin-adenylyl cyclases (RhAC)

Due to the vital role of cAMP in cell signaling and the increasing demand for optogenetic tools that allow rapid spatiotemporal cAMP manipulation, I also sought to convert the substrate specificity of the enzyme rhodopsin CyclOps from GTP to ATP. Before this work, BeCyclOp was the only well-characterized enzyme rhodopsin with GC activity [125, 126]. Here I firstly characterized the CyclOp from the fungus *Catenaria anguillulae* (CaCyclOp). Both BeCyclOp and CaCyclOp were then mutated

into cAMP-specific enzyme rhodopsins, RhACs.

3.3.3.1 Characterization of CaCyclOp in oocytes

The amino acid sequence of CaCyclOp and BeCyclOp show 77% identity. The N-terminal extension (aa 71-170) ahead of the 7 TM helices between two enzyme rhodopsins are slightly different, suggesting 1 or 2 additional helices. To investigate the N-terminus location, we fused two fragments of a split YFP at the N- and C- terminal of the rhodopsin domain (aa 1–425). Emitted YFP fluorescence indicated that the N-terminus is positioned cytosolically (Fig. 3.16A). To assess the cyclase activity of CaCyclOp, the concentrations of cGMP and cAMP were determined in oocyte lysates using ELISA (Fig. 3.16B-C). In the dark condition, the concentration of cGMP CaCyclOp-expressing oocytes kept at around 0.4 μ M, whereas 1 min with green light illumination increased cGMP to 120 μ M. To facilitate future studies in host cells, such as neuronal networks, we labeled a YFP tag at either N- or C- terminus of CaCyclOp (for its even TM topologies). Interestingly, I found that N-terminal fusion of YFP showed no obvious effect on the enzymatic activity of CaCyclOp. In contrast, C-terminal YFP tagging caused obvious increase of the cGMP concentration in the dark (about 10-fold, Fig. 3.16B). For all CaCyclOp variants, cAMP concentrations remained below 2 μ M under both dark and light conditions (Fig. 3.16C), confirming the GTP selectivity of CaCyclOp [125]. To directly compare the dark and light activity of CaCyclOp variants, *in-vitro* enzymatic characterization by using membranes from oocytes expressing these YFP-tagged constructs were performed. As expected, YFP-CaCyclOp shows a much lower turnover than CaCyclOp-YFP (about 25%) in synthesizing cGMP in dark. After light irradiation, cGMP turnover increased more than 1000 folds (Table 3.5). The L/D ratio of CaCyclOp is comparable with that of BeCyclOp [125]. As for cAMP, no measurable dark or light activity is could be detected in our assay (Table 3.5).

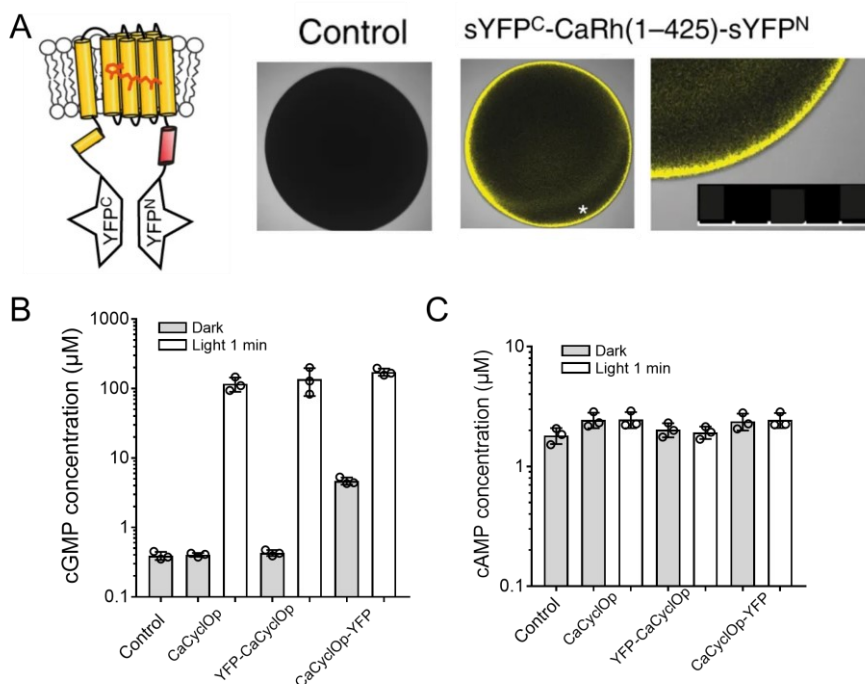


Figure 3.16 Characterization of CaCyclOp in oocytes.

(A) Single plane confocal images of a non-injected control oocyte and an oocyte expressing the first 1–425 aa (CaRh) inserted between the two halves of a split YFP (*region enlarged, scale bar = 500 μm). After 3 days expression, the YFP fluorescence is reconstituted in oocytes. ELISA-based quantification of cGMP (B) and cAMP (C) from whole oocyte lysates. Oocytes expressing untagged CaCyclOp, YFP-tagged CaCyclOp (N- or C-terminal) were kept in darkness or illuminated with green light (1 min, 532 nm 0.3 mW/mm²). Data are presented as Mean ± SD, *n* = 3 samples of 5 oocytes each. Panel A from S. Gao in our lab.

3.3.3.2 Conversion of CyclOp into RhAC

Sequence alignment of BeCyclOp and CaCyclOp to other type III nucleotidyl cyclases indicated that the E497 and C566 in the GC domains determine its GTP selectivity (Fig. 3.17A). In the ACs, these positions are occupied by a lysine and an aspartate (or threonine), which could accommodate the adenine base by interactions with the ring nitrogen N1 and the amino group N6, respectively [164]. I therefore mutated E497 to K and C566 to D similar to previous studies [165, 166] and expressed the N-terminal YFP-tagged mutants constructs in oocytes for 3 days. I used the ELISA again to quantify the cyclic nucleotide concentrations in lysates. Both mutated constructs from BeCyclOp and CaCyclOp indeed changed from GC into AC, which were named as BeRhAC and CaRhAC respectively (alternative naming: CyclOp-PACs). Similar to Trieu et al. [167], I found that BeRhAC expressing oocyte shows 5

times increase of cAMP level in comparison with non-injecting oocyte ($18.5 \pm 2.4 \mu\text{M}$ vs. $3.2 \pm 1.1 \mu\text{M}$) in the dark state. After light illumination, cAMP only increased a further 9-fold (Fig. 3.17B). In oocytes expressing CaRhAC, the dark cAMP ($7.9 \pm 2.6 \mu\text{M}$) was only 2.6 times higher than in the non-injected oocytes and cAMP increased $31\times$ after exposed to light ($150 \pm 28.2 \mu\text{M}$, Fig. 3.17B). For both RhACs, the cGMP levels were similar to non-injected oocytes, regardless of illuminated or kept in darkness (Fig. 3.17C). By using oocyte membranes *in-vitro* assay, I found that YFP-CaRhAC indeed shows lower dark activity than YFP-BeRhAC (Table 3.5), consistent with the results from oocyte lysates (Fig. 3.17B). To reduce the dark activity of RhACs, we introduced four further additional point mutations between aa 564 and 568 to mimic the nucleotide binding pocket of membrane-anchored ACs (tmAC C2) (Fig. 3.17A). The dark activity was not detected in oocytes expressing the 6-mutation containing variants BeRhAC-6 \times and CaRhAC-6 \times , but light-induced cAMP production was also reduced as well (Fig. 3.17B). Oocyte membrane assay also confirmed the reduced dark activities of YFP-RhACs-6 \times and increased L/D ratios. cGMP production was not detected by any RhAC mutants, as expected (Table 3.5).

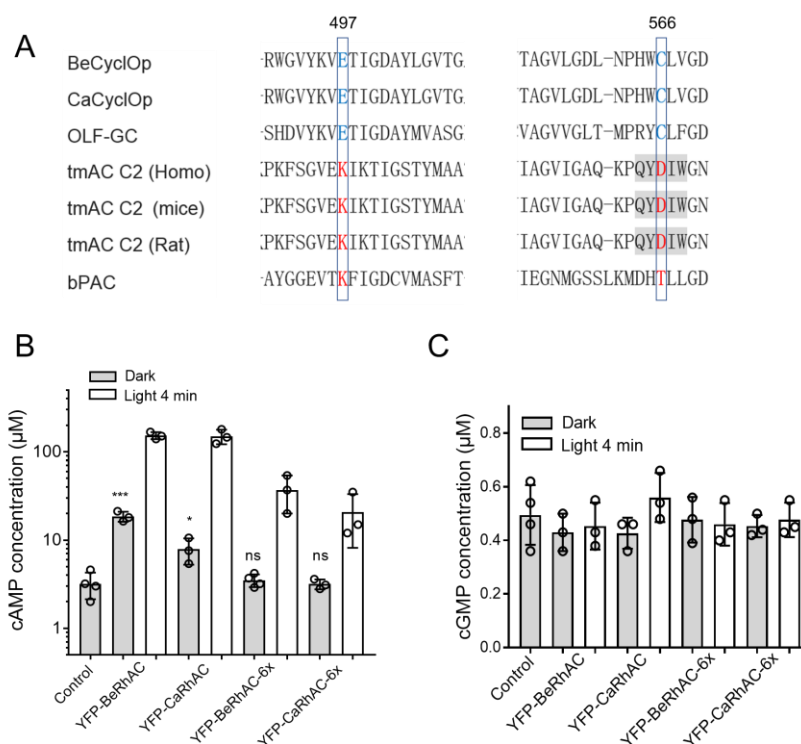


Figure 3.17 Engineering and characterization of adenylyl cyclases.

(A) Sequence alignment of GCs and ACs from various organisms showed key residues involved in

the nucleotide binding of GCs (in Blue) and ACs (in Red). Mutation of the double mutation E497K, C566D-generated Ca/BeRhACs. Four additional mutations (564-QYDIW-568) were inserted in Ca/BeRhACs-6 \times . Enzymatic specificities of the RhACs were determined by the quantifications of cAMP (B) and cGMP (C) within oocytes via ELISA. Oocytes were kept in the dark or illuminated (light 4 min, 532 nm, 0.3 mW/mm²) immediately before lysis. Data were shown as Mean \pm SD, $n = 3$ samples of 5 oocytes each, *** $p < 0.0001$, * $p = 0.02$, ns = not significant from control one-way ANOVA (dark conditions $p < 0.0001$) followed by Tukey's multiple comparisons. Control means the non-injected oocytes.

Table 3.5 In vitro quantification of cAMP and cGMP by RhACs in oocyte membranes

	cGMP turnover (min ⁻¹)			cAMP turnover (min ⁻¹)		
	Dark	Light	L/D	Dark	Light	L/D
YFP-CaCyclOp (20 °C)	0.028 \pm 0.007	71 \pm 10.7	2500	Not detectable	Not detectable	—
CaCyclOp-YFP (20 °C)	0.11 \pm 0.04	120 \pm 9.3	1100	Not detectable	Not detectable	—
YFP-BeCyclOp (20 °C)	Not detectable	Not detectable	—	0.19 \pm 0.01	42.1 \pm 0.6	220
YFP-CaCyclOp (20 °C)	Not detectable	Not detectable	—	0.14 \pm 0.01	39.4 \pm 5.6	280
YFP-BeRhAC-6 \times (20 °C)	Not detectable	Not detectable	—	<0.001	0.7 \pm 0.13	>700
YFP-BeRhAC-6 \times (37 °C)	Not detectable	Not detectable	—	<0.001	3.2 \pm 0.8	>3200
YFP-CaRhAC-6 \times (20 °C)	Not detectable	Not detectable	—	0.001 \pm 0.0001	0.74 \pm 0.08	740
YFP-CaRhAC-6 \times (37 °C)	Not detectable	Not detectable	—	0.016 \pm 0.005	1.72 \pm 0.36	108

1. Values are mean \pm SD $n = 3$.

2. RhAC:E497K C566D, RhAC-6 \times :E497K 564QYDIW568

3.4. Dual-color bi-directional control of cell activity

Optogenetics tools enable activation or inhibition of cell activity with high spatiotemporal precision and low invasiveness. Independently driving pairs of optogenetic actuators with different wavelengths light would enable the separate manipulation of different cell populations or bi-directional control of the same cell type, which will greatly facilitate dissecting the contribution of specific cell types to brain circuit function. The first dual-color optogenetic control of cell activity was conducted by coupling *NpHR* and *ChR2* [16, 17]. However, due to the “centered” action spectrum of *ChR2*, it’s difficult to achieve robust dual-color optogenetic control by using a red-shifted rhodopsin alongside *ChR2*. The natural strategy for optimization would be coupling the most spectrum separable actuators. However, nearly all red-shifted rhodopsins remain certain responses to blue light due to the fundamental property of retinal chromophore [168]. Another potential way is introducing differences in blue light sensitivity between blue and red light drivable optogenetic tools. Then a low-density blue light could trigger reliable response through activation of the blue light drivable actuator, while only inducing subthreshold responses from the red light drivable tools. By combining these two strategies, here I achieved robust dual-color bi-directional control of cell activity with negligible crosstalk by using *vf-Chrimson* and *SthK-bP* variants. Moreover, I found that optimization of the light illumination scheme could also be applied to minimize the crosstalk, in addition to adjusting light wavelength and intensity.

3.4.1 Generation and selection of optogenetic actuator for activation

Based on the action spectrums of microbial rhodopsins, *Chrimson* variants were selected as the depolarization tools for the most red-shifted action spectrum [85]. In addition, for fast inducing AP spiking in neuron cells, a variant with fast kinetics is preferred. *Vf-Chrimson* meets both two criteria [103], despite the relatively small photocurrent amplitude. To enhance the photocurrent amplitude, here I applied molecular trafficking strategies to increase the surface membrane expression. Adding a traffic signal peptide (T) and an ER export signal peptide (E) between the YFP tag at the C-terminal of *vf-Chrimson* increased the photocurrent of *vf-Chrimson*-YFP about 2 folds (Fig. 3.18). Additional N-terminal fusion of *LucyRho* (LR) signal peptide [169] further enhanced the photocurrent magnitude (Fig. 3.18). Similar to *ChR2*, *Chrimson*

also contains a long N-terminal extension. Here I compared the influences of different lengths of N-terminal truncations on the photocurrent amplitude of vf-Chrimson. Truncation of the first 29aa significantly improved the photocurrent amplitude, while N-terminal 34aa deletion resulted in the photocurrent reduction. β linker (the first 150aa of the rat gastric H^+/K^+ -ATPase β subunit) has been used for improving membrane targeting efficiency of proton pump FR (unpolished data from S. Gao) and sodium pump KR2 (own unpublished data). Photocurrent comparison showed that the LR signal peptide significantly outperformed the β linker on improving the membrane trafficking efficiency of vf-Chrimson variants. Chrimson-S169A displays 10-fold accelerated channel closing kinetics than wt-Chrimson, but much-reduced photocurrent amplitude [88]. Applying the same trafficking module and N-terminal truncation to Chrimson-S169A only increase its photocurrent to about 60% of LR-(-29aa)-vf-Chrimson-TYE. Further modifications of LR-(-29aa)-vf-Chrimson-TYE by either introducing additional membrane trafficking peptide (e.g. β linker or Cs peptide) or additional point mutation S169A, led to significant reduction of photocurrent amplitude. (Fig. 3.18). Collectively, LR-(-29aa)-vf-Chrimson-TYE was selected as the optimal tool for red light mediated activation and was renamed as vf-Chrimson 2.0.

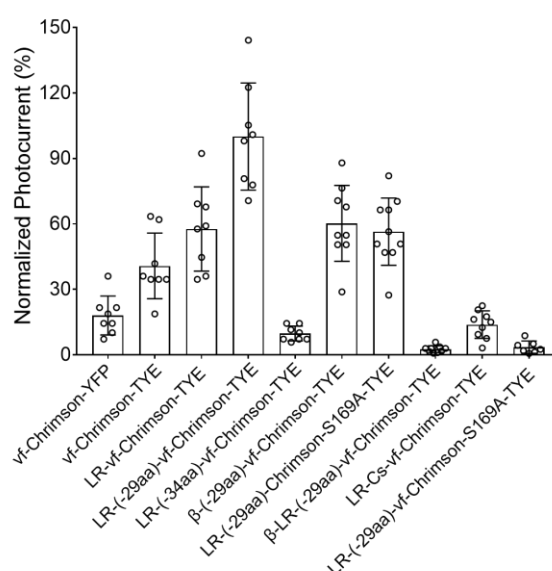


Figure 3.18 Photocurrent amplitude comparison of different Chrimson constructs.

Different constructs were generated via modifying the N- or/and C-terminal of vf-Chrimson. TYE indicates the molecule cassette comprised of traffic signal (T) from Kir2.1, YFP and ER export signal (E). LR stands for Lucyrho signal peptide identified form [169]. -29aa and -34aa means the

truncation of the first 29 and 34 amino acids of vf-Chrimson, respectively. β represents the β linker of the rat gastric H^+/K^+ -ATPase β subunit. vf-Chrimson is the triple mutant version of Chrimson (K176R/Y261F/S267M). Cs means the N terminus from CsChR. Oocytes were injected with 30 ng cRNA of each construct and incubated for 3 days in ND96 solution with 10 μ M ATR. Photocurrent was recorded in Ori-standard solution (pH 7.6). The average current of LR-(-29aa)-vf-Chrimson-TYE was taken as 100% for normalization. Holding potential at -70 mV. Light source: 635 nm laser at 3 mW/mm².

3.4.2 Comparison of light-gated potassium channels

For neural silencing, light-gated potassium channels have unrivalled advantages over pump rhodopsins or chloride conducting ChRs (see details in Introduction 1.5). Till now, three different versions of blue light activated potassium channels (SthK-bP [138], split PAC-K and fused PAC-K [139]) via combining bPAC and SthK were reported by our group and others. These three constructs differ in the strategies for combining bPAC and SthK (Fig. 3.19A). To check the expression levels, an additional YFP protein was fused to split PAC-K and fused PAC-K, generating SthK-P2A-bPAC-YFP and bPAC-L-SthK-T2A-YFP, respectively. Injection of 5 ng SthK-bP showed a similar expression level with the other two of 10 ng injection in *Xenopus* oocytes, indicating the superior expression properties of SthK-bP. Under similar protein levels, SthK-bP exhibited the highest photocurrent amplitude (Fig. 3.19B), and the lowest cAMP production in dark and light (Fig. 3.19C). For the host cells with low PDE activity, the relatively low cAMP production of SthK-bP is a very appreciated feature. Moreover, SthK-bP also displays the most favorable kinetic properties ($\tau_{on} = 6.8 \pm 1.9$ s, $\tau_{off} = 133 \pm 35$ s) among all three constructs (Fig. 3.19D-E). In conclusion, SthK-bP outperformed the other two constructs and could be adopted here as the blue light drivable hyperpolarization tool. However, wt-SthK channel shows high affinity to cAMP ($K_m = 3.68 \pm 0.55$ μ M) [170]. Endogenous cAMP may directly activate the SthK channel, independently of light-triggered cAMP. To overcome this problem, Gao and Yu-Strzelczyk designed an improved SthK-bP variant with reduced cAMP affinity. Based on the crystal structure of the C-terminal region of SthK [171], a point mutation T378V and the deletion of the last C-terminal 8 aa were introduced into SthK. This improved construct was determined to show the K_m value for cAMP at 10 μ M and was named as SthK(TV418)-bP (unpublished data from S. Gao and J. Yu-Strzelczyk).

SthK(TV418)-bP was then selected as the blue light activated inhibitory tool for dual-color optogenetics.

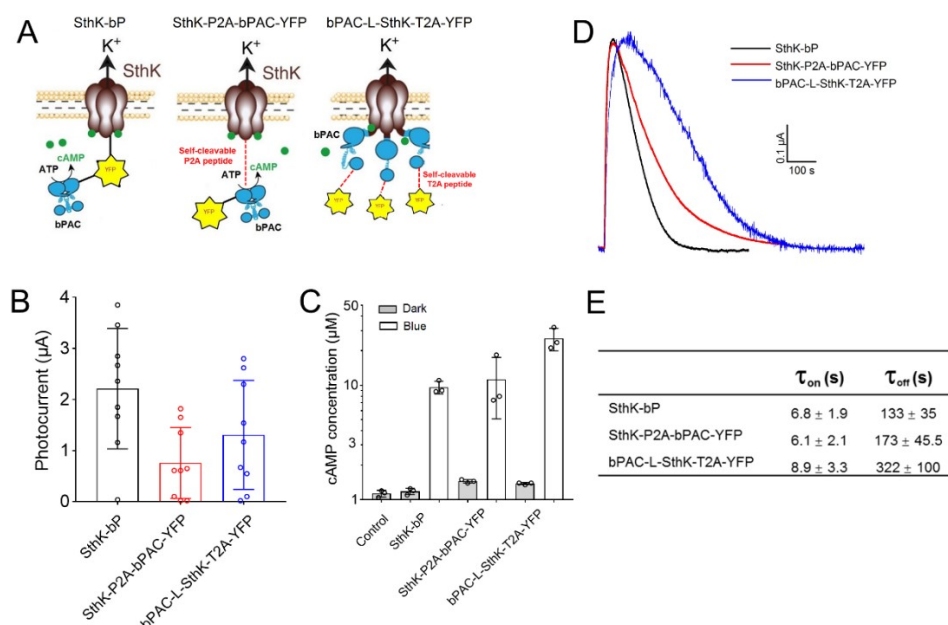


Figure 3.19 Comparison of potassium channel based inhibitory tools.

(A) Scheme of different bPAC-SthK constructs from [138] (left) and [139] (middle and right) with slight modifications. (B) Photocurrent amplitude comparison of three constructs with similar expression levels. (C) cAMP production of three constructs under dark or blue light illuminated condition (473 nm at 0.3 mW/mm² for 30 s). For (B) and (C), SthK-bP is injected with 5 ng, while the other two constructs were injected with 10 ng. (D) Sample photocurrent traces on a similar level (~0.6 μ A) of three constructs after 50 ms 473 nm light illumination. cRNA injection amount: 2 ng for SthK-bP, 5 ng for SthK-P2A-bPAC-YFP and bPAC-L-SthK-T2A-YFP. (E) Quantification of on and off kinetics of three constructs from (D). All the TEVC measurements were performed in Ori standard solution at pH 7.6, holding at -20 mV.

3.4.3 Selection of the ideal light stimuli

As vf-Chrimson-2.0 and SthK(TV418)-bP exhibit distinct action spectrums, I next tested whether these two molecules can be combined together to bi-directional manipulate the membrane potential in the same cell by two wavelengths light. Due to the relatively narrow action spectrum of bPAC, light in the red region could not activate SthK(TV418)-bP at all [110, 111], allowing activation of vf-Chrimson 2.0 by the red light at maximum intensity. On the contrary, vf-Chrimson 2.0 still displays robust responses to the blue range light [85, 88]. As two published action spectrums of Chrimson showed clear differences between 400 and 450 nm, I first compared the light sensitivity of vf-Chrimson 2.0 towards 400 nm and 450 nm [85, 88]. Surprisingly, unlike the red light induced channel fast-switching, illumination by either 400 nm or

450 nm light, vf-Chrimson-2.0 exhibited a very slow channel closing rate (Fig. 3.20A-C). Therefore, it's difficult to reliably compare the abilities of 400 nm and 450 nm light in evoking photocurrent of vf-Chrimson-2.0 in the same oocyte, as incompletely channel closure will lead to a smaller photocurrent amplitude upon the second light illumination. I then calculated the ratio of the photocurrents evoked by 400 or 450 nm light to 635 nm light (i.e. I_{400}/I_{635} vs I_{450}/I_{635}). No significant difference was observed between I_{400}/I_{635} and I_{450}/I_{635} (Fig. 3.20D), indicating vf-Chrimson 2.0 displays similar light sensitivity to 400 nm and 450 nm light. On the other hand, 450 nm light could activate bPAC much better than 400 nm, according to its absorbance spectrum [110]. 450 nm light was therefore chosen over 400 nm as the stimulus.

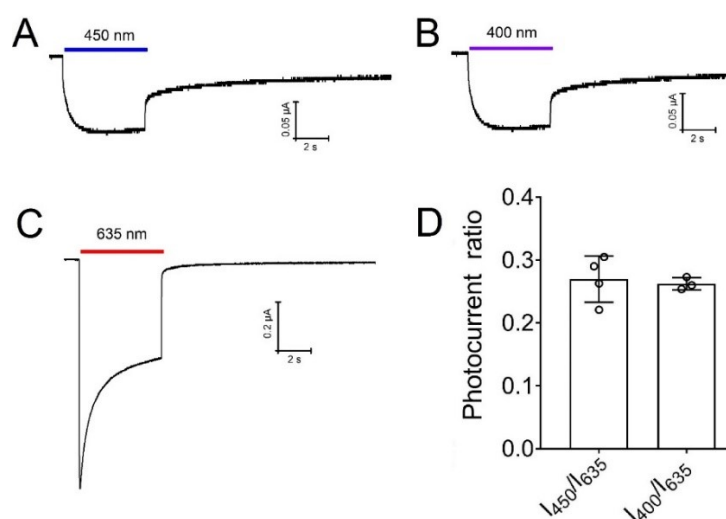


Figure 3.20 Photocurrents of vf-Chrimson 2.0 induced by different wavelengths light.

Photocurrent traces of dark adapted vf-Chrimson 2.0 induced by 450 nm light at 0.4 mW/mm² (A), 400 nm light at 0.4 mW/mm² (B), or 635 nm light at 3 mW/mm² (C). (D) 400 nm and 450 nm show similar ability in evoking photocurrent of vf-Chrimson 2.0. Oocytes expressing vf-Chrimson 2.0 were firstly illuminated with 635 nm light at 3 mW/mm² for 5 s. After 30 s delay, the second 5 s illumination by 450 nm or 400 nm light at 0.4 mW/mm² was applied. I_{635} , I_{450} and I_{400} are the photocurrents at 5 s induced by the indicated wavelength light. Similar photocurrent ratio indicates that vf-Chrimson 2.0 has similar sensitivity to 400 nm and 450 nm. Data are shown as Mean \pm SD. n = 3-4. All the TEVC measurements were performed in Ori-standard solution at pH 7.6, holding at -60 mV.

3.4.4 Implementation of dual-color optogenetics in *Xenopus* oocytes

I next co-expressed vf-Chrimson 2.0 and SthK(TV418)-bP in *Xenopus* oocytes and recorded the photocurrents induced by 635 nm and 450 nm light by using TEVC methods. When holding membrane potential close to the physiological level, the inward photocurrent is exclusively mediated by vf-Chrimson 2.0 and the outward photocurrent

is only contributed by SthK(TV418)-bP. According to the action spectrums of two constructs, the possible crosstalk only occurs upon 450 nm light illumination. The apparent photocurrent under 450 nm light illumination is jointly contributed by vf-Chrimson 2.0 mediated inward photocurrent and SthK(TV418)-bP mediated outward photocurrent. In principle, a low amount of vf-Chrimson 2.0 and a high level of SthK(TV418)-bP could reduce the crosstalk to a negligible level. High density red-light could at least partially compensate for the reduction of photocurrent of vf-Chrimson 2.0 resulting from the low protein level. Therefore, it's crucial to adjust the protein expression levels of two constructs in the cell. In oocytes, the ideal cRNA injection molar ratio of vf-Chrimson 2.0 and SthK(TV418)-bP was found to be at 1 to 2. Keeping with this ratio, upon red-light illumination, significant inward current rapidly emerged. As blue light is able to activate both vf-Chrimson 2.0 and SthK(TV418)-bP, dim light illumination is preferred. Illumination with 450 nm light at $40 \mu\text{W}/\text{mm}^2$ for 2 s, strong outward photocurrent raised up shortly with a tiny inward photocurrent at the beginning (Fig. 3.21A). Consistent with the slow photocycle of vf-Chrimson 2.0 upon blue light irradiation, light pulse stimulation resulted in smaller inward photocurrent than continuous light illumination (Fig. 3.21B). Moreover, bPAC is capable of integrating light over time. Taken together, applying light pulse illumination could minimize the crosstalk. As expected, pulsed blue light stimulation showed a remarkable reduction of the crosstalk in comparison with continuous light illumination, although the raise of the photocurrent took a slightly longer time (Fig. 3.21C).

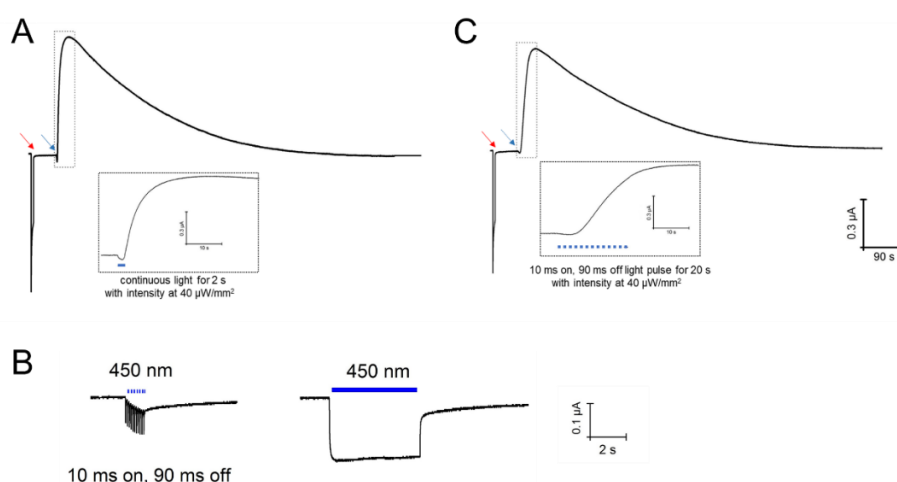


Figure 3.21 Optimized light illumination scheme minimizes the crosstalk of dual-color

optogenetics in *Xenopus* oocytes.

(A) The oocyte was first illuminated by 5 s 635 nm light (red arrow) at 3 mW/mm². A 450 nm light at intensity of 40 μ W/mm² was later applied for 2 s continuous illumination (blue arrow). (B) Photocurrent traces of vf-Chrimson 2.0 evoked by pulse light stimulation and continuous light stimulation. The intensity of 450 nm light is at 0.8 mW/mm². (C) Red arrow indicates 5 s illumination of 635 nm light at 3 mW/mm². Blue arrow means 450 nm light pulse illumination (10 ms on, 90 ms off) for 20 s at 40 μ W/mm². *Xenopus* oocytes were either injected with 20 ng cRNA mixture with the molar ratio of vf-Chrimson 2.0 to SthK-(TV418)-bP at 1 to 2 for (A) & (C); or only 20 ng vf-Chrimson 2.0 for (B). All recordings were performed in Ori-standard solution at pH 7.6. Holding at -60 mV.

Aside from the ability to integrate light over time, bPAC also shows very high light sensitivity. Therefore, it's also feasible to activate SthK(TV418)-bP by using extremely low intensity blue light with minimum activation of vf-Chrimson 2.0. Keeping the overall blue light stimulation power constant, two different light illumination protocols were compared: light pulse stimulation (10 ms on, 90 ms off light pulses for 20 s with light intensity at 40 μ W/mm²) and continuous light illumination (light intensity at 4 μ W/mm² for 20 s). As expected, prolonged low-density 450 nm light illumination induced robust outward photocurrent with ignorable initial crosstalk, which is comparable with the light pulse stimulation (Fig. 3.22A-B). In conclusion, the crosstalk can be minimized to a neglectable level by either applying light pulse stimulation or simply using very low-intensity blue light irradiance.

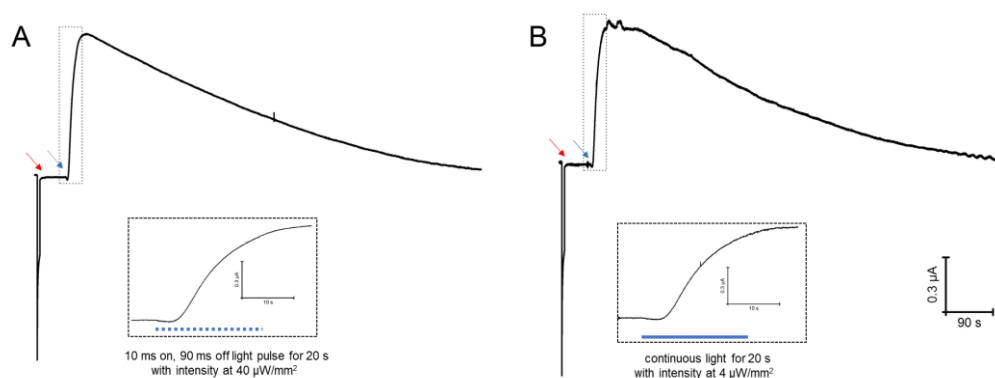


Figure 3.22 Dual-color light induced photocurrent in oocytes expressing vf-Chrimson 2.0 and SthK-(TV418)-bP.

Xenopus oocytes were injected with 20 ng cRNA mixture in total, with the molar ratio of vf-Chrimson 2.0 to SthK-(TV418)-bP at 1 to 2. Red arrow indicates 5 s illumination of 635 nm light at 3 mW/mm². Blue arrow means 20s illumination with 450 nm light, either by 10 ms on, 90 ms off pulsed stimulation at 40 μ W/mm² (A) or continuous stimulation at 4 μ W/mm² (B). Inserted box is the enlarged view. All recordings were performed in Ori-standard solution at pH 7.6. Holding at -

60 mV.

Current-clamp experiments with *Xenopus* oocytes co-expressing vf-Chrimson 2.0 and SthK(TV418)-bP were further conducted. A fast membrane depolarization by tens of millivolts was observed when applying red light illumination (Fig. 3.23A). Upon low intensity blue light (at $4 \mu\text{W}/\text{mm}^2$) stimulation, a very small membrane depolarization ($\sim 1 \text{ mV}$) firstly arose at the beginning, which is caused by the tiny crosstalk between vf-Chrimson 2.0 and SthK(TV418)-bP under blue light irradiance (Fig. 3.23B). K^+ current mediated membrane hyperpolarization was then appeared and lasted for tens of minutes (Fig. 3.23A-B). Collectively, here I provided the proof-of-principle evidence in *Xenopus* oocyte that the combination of vf-Chrimson 2.0 and SthK(TV418)-bP is suitable for dual-color excitation-inhibition experiments.

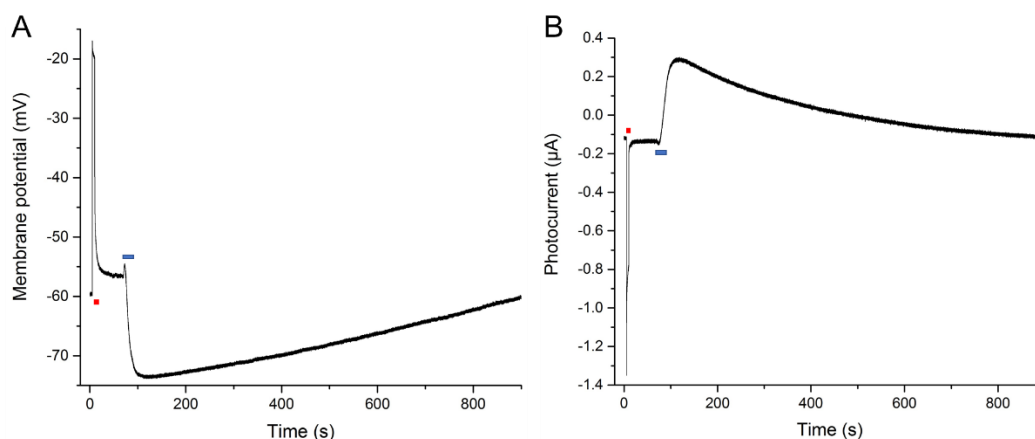


Figure 3.23 Current-clamp (A) and voltage-clamp measurements (B) of *Xenopus* oocyte expressing vf-Chrimson 2.0 and SthK(TV418)-bP.

Xenopus oocytes were injected with 20 ng cRNA mixture with the molar ratio of vf-Chrimson 2.0 to SthK-(TV418)-bP at 1 to 2. For current-clamp measurement, the initial membrane potential was biased to about -60 mV. For voltage-clamp measurement, the holding voltage is set to -60 mV. 635 nm laser and 450 nm laser were used here as light sources. All recordings were performed in Ori-standard solution at pH 7.6.

4. Discussions

4.1 Discussion for ChR2 project

4.1.1 Improved ChR2 variants expand the optogenetic application

wt-ChRs are permeable for multiple ions with the highest conductance for H⁺. Under physiological condition, the overall photocurrent of ChR2 is mainly contributed by H⁺ and Na⁺ [69, 76]. Although the nonspecific conductance is not an issue for many neuroscience studies. However, prolonged illumination of ChR2 may cause undesired cytosol acidification. Proton signaling pathway regulates many aspects of the cell activity. On the other hand, when regulation of pH is needed, high H⁺ conductive channels like Chrimson or Chronos are preferred over ChR2 [68, 85, 86]. Here engineered ChR2 variants all dramatically increased the Na⁺/K⁺ conductance, ensuring no acidification effect upon application. Moreover, the new variants also display other valuable features like high photocurrent amplitude and altered Ca²⁺ conductivity, which will greatly expand the optogenetic application scenarios.

The unitary conductance of ChR2 (about 40 fS) is about 10-10⁴ smaller compared to many neuronal ion channels [172]. To reliably trigger APs, high amount of protein will be needed when the single-channel conductance is low. However, very high expression of membrane protein (like ChIEF or ChR2) may increase the membrane capacitance [173, 174]. Increasing the single-channel conductance could reduce the necessary amount of ChRs in cell membranes for triggering a physiological response to light. Besides the impacts on membrane capacitance, ChRs with high photocurrent amplitude are preferred in various cases. High photocurrent amplitude channel enables triggering multiple spikes with very short light illumination, which would avoid or reduce the risk of phototoxicity. When chronic stimulation is needed, repetitive short light pulses could be used for persistently inducing AP firing. Moreover, for certain experiments, some weaker and more specific promoters are needed, only the channels with large photocurrent amplitude could active these genetically defined subsets of cells.

For calcium signaling manipulation, high Ca²⁺ conducted channels are still lacking. The most widely used CatCh only slightly elevates the calcium conductance of ChR2 with a factor of 1.4 [81]. Although Olf-bP shows high Ca²⁺ permeability, its very slow

kinetic properties and potential side effects from cAMP is unfavorable [138]. Here engineered H134Q/D156H mutant exhibits heretofore the highest Ca^{2+} conductance, improved photocurrent amplitude and Na^+/K^+ conductance. When illuminated with short light pulses, H134Q/D156H showed fast kinetics comparable to CatCh (Fig. 3.2), while much higher Ca^{2+} current amplitude. Prolonged irradiation further increases the photocurrent amplitude of H134Q/D156H, despite with medium channel closing time ($\tau_{\text{off}} = 1.5$ s). Accordingly, H134Q/D156H is both suitable for the precise induction of small Ca^{2+} influx and for inducing large Ca^{2+} influx when necessary. More importantly, H134Q/D156H mutant may significantly expand the optogenetic application scenarios, especially in cardiovascular electrophysiology and plant electrophysiology. The cardiac APs and AP-like electrical signals in plants are much longer and more complex in comparison with the neural AP. And they often need Ca^{2+} as an intermediary. Therefore, H134Q/D156H is particularly appreciated in these fields considering the demands of Ca^{2+} influx and high electrotonic load.

On the other hand, in some applications the Ca^{2+} influx is undesired. Considering the broad roles of calcium in cell signaling transduction, some unintended Ca^{2+} influx may lead to side effects or complicate the data analysis [149, 150]. Therefore, when Ca^{2+} should be avoided, the high Na^+/K^+ , low H^+ and Ca^{2+} conducting ChR2-5x could be selected for application. Moreover, when combining with high Ca^{2+} conducted ChRs, it's also helpful to dissect the contributions of membrane depolarization and Ca^{2+} influx to the physiological events.

4.1.2. Structural determinants of the photocurrent properties of ChR2 variants

In ChR2, the putative ion conductive pathway contains a series of negatively charged residues, ensuring only cations are permeable for ChR2. Lacking specific ion-selective filter further explains its non-selective properties. In this scenario, the affinity and size of the cation towards the ion conductive “tunnel” will dramatically influence its permeability. Indeed, the dependence of photocurrents on different cations strongly negative correlates with their atomic radius [9]. As the putative ion-permeable pathway is composed of TM helices 1, 2, 3 and 7. A number of amino acids in helices 2 and 3

were found to influence the cation selectivity, despite these modifications only slightly changed on the ion permeability. Mapping these residues onto the structure of ChR2 revealed that they all involved in the formations of the three molecular gates of ChR2. As confirmed here, systematically substitutions of the gates-formation residues could indeed significantly alter the ion selectivity of ChR2. Moreover, these modifications also dramatically influence the photocurrent amplitude of ChR2. Here selected gate residues (E83, E101, H134) were either mutated to residues with non-titratable side chain or negatively charged side chain with smaller size. Non-titratable residues would reduce the proton transfer, therefore increase the permeability of other cations. Residue with smaller side chain may enlarge the radius of the open-state constriction sites (i.e. the molecular gates) of ChR2, which leads to the overall increased conductance. In addition, here I also found that mutations in the helix 4 (D156) and the extracellular loop area (H114) also influence the photocurrent properties of ChR2. Importantly, these mutations could be combined in a synergistic manner, suggesting that long-range interaction networks in ChR2. These molecular determinants seem to distributed throughout the backbone, spanning the transmembrane domains, and the cytosolic and extracellular loops [99]. Therefore, an ion-conducting, open-state structure of ChR2 is highly demanded for interpreting the precise mechanisms of ion selectivity and conductivity.

4.1.3 Next step in ChR engineering

The photocurrent amplitude of ChRs will not be an issue now. However, if further larger photocurrent-amplitude ChR is needed, systematically mutating the gate residues to widen the radius of the gates or reduce the number of gates could be applied. Normally the channel with fewer constriction sites shows higher conductance. For example, GtACR1 only contains one molecular gate [102, 175], showing a much higher conductivity than ChR2. Enhancing the plasma membrane targeting could be adopted as an alternative strategy. In addition, here identified mutations may also be introduced into other ChR constructs. For example, Mutating H134Q into ChR2-XXL also showed increased Na^+/K^+ permeability and photocurrent amplitude (unpublished data from X.

Duan). If additional E83D and H114G are also compatible in ChR2-XXL2.0, it would further improve the channel conductivity and light sensitivity, eventually enabling the transcranial optogenetics, like ChRger2 [105].

It still remains very challenging to engineer a specific ion conducting ChR. The highly selective ion channel normally contains a symmetrical ion pathway. However, in monomeric ChRs, the ion-conducting pore is very asymmetric. Large scale screening can be a possible way to obtain a specific ion permeable ChR. For example, the yeast-based screening system could be adopted for screening the K⁺-specific ChRs. Here engineered high Na⁺/K⁺ conducting constructs can be served as starting templates for screening. In addition, machine-learning-guided protein engineering or *de novo* protein design may also be applied in ChRs engineering in the future.

4.2 Discussion for *NpHR* project

Up to now, the chloride pump *NpHR*-TYE is one of the most popular optogenetic tools for hyperpolarization of excitable cells. Like many other rhodopsin-based optogenetics tools, inactivation upon light illumination is a main obstacle hindering the application of *NpHR*-TYE [173]. Here I systematically studied the inactivation of *NpHR*-TYE caused by long time illumination in *Xenopus* oocyte. The finding in oocyte shows higher similarity with the experiment in murine hippocampal neurons [158]. The congruent findings in these two different expression systems reflect the property of the protein itself, largely eliminating the influence from possibly protein-protein interaction in the host system. Indeed, the inactivation upon long time light illumination, slow self-recovery by thermal decay in dark, as well as the accelerated recovery by blue light illumination of *NpHR*-TYE were faithfully observed in both host cells. In addition, the temporal stability of *NpHR*-TYE is improved under optimized stimulation condition, such as co-application of orange and blue light or blue light itself alone, appears in both systems.

4.2.1 Biophysical mechanism of *NpHR*-TYE inactivation and recovery

Inactivation of the homologue protein *HsHR* from the *Halobacterium salinarum* was proven to be the consequence of accumulation of an M-like intermediate from a branched photocycle with deprotonated Schiff base [156, 176-178]. Therefore, the inactivation of *NpHR* was naturally attributed to a similar mechanism without further investigation [16, 17]. To gain additional insights into the mechanism of the inactivation of *NpHR*-TYE, I characterized the effects of different light illumination and extracellular ionic conditions on the inactivation of *NpHR*-TYE. Light dose and wavelength dependences of inactivation might be due to different photochemical processes underlying different light stimuli. The proton and chloride dependences of inactivation strongly support the Schiff base deprotonation hypothesis. Unlike BR, where the positive charge of protonated Schiff base is counterbalanced by its aspartate D85, in *NpHR* this negative charge is provided by the binding of chloride ion [39]. Accordingly, a decrease of either extracellular proton or chloride concentration will

increase the chance of deprotonation of the Schiff base, although the Schiff base of *NpHR* was suggested to be never deprotonated in chloride pumping cycle [179-181]. To effectively transport chloride, the Schiff base needs to be protonated to facilitate chloride binding. Therefore, *NpHR* intermediate with deprotonated Schiff base is stable and non-pumping. Indeed, the slow kinetics of recovery from inactivation of *NpHR*-TYE is also consistent with the stable and non-pumping feature of this M-like intermediate. Collectively, my data confirms that the inactivation of *NpHR*-TYE after long-time illumination is due to formation of an M-like intermediate with deprotonated Schiff base (Fig. 3.8).

I next assessed the effects of different extracellular ionic concentration and membrane potential on the recovery of *NpHR*-TYE from inactivation. The recovery time strongly depends on the extracellular proton concentration, indicating that the proton for reprotonation of the deprotonated Schiff base comes from the extracellular site. Extracellular chloride could also affect the reprotonation of the Schiff base by regulating the pKa through binding to the binding site I [157]. Accordingly, we observed lowering extracellular chloride concentration slowed down the recovery of *NpHR*-TYE. Changing of membrane potential will always cause opposite effects on proton or chloride uptake to the Schiff base, ergo, no difference in the recovery time could be observed under different membrane potential. It's intriguing to ask what the proton source is under blue light induced recovery scenario. I argue it's also from the extracellular site, for the following three reasons: First, in the structure-related *HsHR*, proton uptake has been experimentally proven to occur from the extracellular channel upon restoration of H₄₁₀ to initial state by blue light absorption [156]. Second, in BR, its pump activity can be inhibited by additional blue light. In which, blue light absorption decays the M₄₁₂ to initial BR₅₆₈ state by reprotonation of the Schiff base from the extracellular site [26, 182, 183]. Third, a crystallography study proposed that the reprotonation of Schiff base occurs after the retinal isomerization when the cytosolic interhelical space is already closed, ergo, this proton can only be from the extracellular site [41].

4.2.2 Short-wavelength light enables optimized spatiotemporal control of *NpHR*-TYE

The inactivation of *NpHR*-TYE during continuous illumination [16, 17] limits its

utility for long-lasting (>10 s) neuronal inhibition [see also 184]. However, prolonged silencing of neuronal populations is typically a critical requirement for analyzing their involvement in network oscillations and behaviors. The protein expression levels in many transgenic models are normally low, which requires high power light illumination. Accordingly, conventional yellow light illumination will be problematic for long term inhibition. This study presented that, independent of expression system, inactivation is highly wavelength-dependent, being profoundly reduced for blue as compared to green or yellow light (Fig. 3.5). This finding may have great practical importance. Within the tissue, light power declines with increasing distance from the fiber tip [184]. Consequently, when using yellow light, cells that locate close to the light source (i.e. that are exposed to a relatively high light power) will not only show higher peak photocurrent amplitudes, but also a more pronounced to inactivation than those at longer distances. In other words, besides increasing the temporal stability of *NpHR*-TYE-mediated currents within individual cells, blue light may also minimize differences in inactivation between spatially distributed cells. In oocytes, similar photocurrents stability of *NpHR*-TYE was obtained by combining green with violet light, with higher photocurrent amplitude than pure blue light stimulation (Fig. 3.6). This may render the green-violet light combination the preferred photo-stimulation regime, if high-amplitude photocurrents are required. However, it should be noted that violet and green light exhibit a differential distance-dependent power attenuation in brain tissue, which might cause larger spatial inhomogeneities as outlined above. Therefore, when applying the green-violet light illumination, the light intensity of violet should be adjusted accordingly to overcome the poor tissue penetration problem. In addition, pure blue light stimulation requires simpler hardware solutions than the green-violet combination.

Taken together, this study provides novel approaches for long-term optogenetic silencing that are based on an optimization of light illumination pattern, rather than protein engineering. For short term optogenetic inhibition, yellow light remains the preferred choice for its capability to induce large photocurrent and its favorable tissue penetration ability. However, when prolonged inhibition is required, photo-stimulation

with blue light is advantageous due to its superior temporal stability. Besides, when higher photocurrent is needed, alternative photo-stimulation protocol (i.e. green-violet combination) could be adopted. In sum, our study provides easy-to-implement photo-stimulation approaches for the light-driven chloride pump *NpHR-TYE* that are associated with an extraordinary temporal stability of pump currents and thus render *NpHR-TYE* suitable for long-term neuronal inhibition.

4.3 Discussion for optogenetic tools for cAMP manipulation project

4.3.1 Oocyte-based *in-vitro* assay allows reliable characterization of PACs

The light-regulated cAMP productions by PACs offer superior temporal and spatial resolution compared to conventional pharmacological manipulation of cAMP [185]. when selecting ideal PAC for optical cAMP manipulation, its enzymatic activity is one of the most important parameters for reference. However, the enzymatic activity of existing PACs is either determined ambiguously or completely unknown, possibly due to the difficulties in biochemical purifications. Here I described a convenient *in-vitro* method allowing reliably characterization of light activated enzymes. Crude soluble protein extracts can be gently prepared by this *in-vitro* assay in a short time (see details in Methods 2.9), ensuring the good state of the light activated protein. Three additional reasons further make the enzymatic activity quantification reliable. (1) The PDEs activity in the crude soluble protein extracts could be fully inhibited by adding IBMX. (2) No endogenous light-activated cyclase or PDEs exists in the oocyte. (3) Protein level could be reliably quantified by the emission value of the fused eYFP protein. Indeed, the enzymatic activity quantified by this *in-vitro* assay shows remarkable similarity with previously published results by using other methods [117, 121]. Moreover, the crude soluble protein extracts could also be used for characterization of other photochemical properties of PACs, such as light sensitivity. It should be noted that the spectral properties of PACs can't be measured by this assay. Protein level quantification requires fusion with an eYFP protein, while sometimes eYFP fusion might affect the activity of PACs (like EuPAC α). Still, despite these limitations, our assay provides alternative way for characterization of light activated enzymes.

4.3.2 Molecular mechanism of reducing the dark activity of bPAC

Ideal tools for optogenetic applications require tight light regulation. The basal activity in dark is a main obstacle hindering the application of PACs. Unfortunately, most PACs show obviously dark activity, including bPAC (Table 3.2) [186]. Here I found that dark activity of bPAC could be reduced either by point mutation or membrane targeting. The possible mechanism is discussed in the following. Mutating the catalytic residues is the most straightforward way to reduce the dark activity of bPAC, if the light activity still remains after mutation, as is the case for K197A and R278A. F198Y reduced the dark activity by decreasing the accessibility of ATP to the substrate binding pocket. An alternative strategy to reduce the dark activity of bPAC is

modifying the interactions between the two $\alpha_{3\text{blue}}$ helices, as altered interactions between two helices may confer different orientations between two AC domains, which would directly regulate the AC activity, such as L123R/C. In addition, H120 and L121 could also be tested for reducing the dark activity. When anchoring bPAC to the plasma membrane, it might decrease the chance of the modified bPAC to form the functional dimer. In addition, the orientation between two chains of membrane-bound bPAC dimer may also differ with that in the soluble bPAC. These two effects may jointly contribute to the altered activity of the membrane-anchored bPACs.

4.3.3 Dark activity-reduced soluble and membrane-anchored PACs expand the optogenetic application

Dark activity is the main obstruction for the application of PACs, as continuously produced cAMP in dark might change the properties of transfected cells or tissues prior to the actual experimental interventions. Therefore, here engineered dark activity reduced PACs are highly desired. In addition, PACs with accelerated photocycle are also very appreciated. As the decay of intracellular cAMP level after light illumination was largely determined by the time constant of PACs inactivation, in addition to the endogenous PDE activity. Fast off kinetics offers higher temporal resolution for cAMP manipulation. The bPAC-F198Y mutant could be a promising tool for its reduced dark activity and accelerated photocycle.

Compartmentalization of cAMP signaling model now is increasingly popular, for accumulating evidence support that physiological relevant signal occurs within confined nanodomains, instead of bulk changes in cytosolic cAMP [187]. Indeed, activation of different subcellular localized bPAC induced distinct biochemical consequences [163, 188]. Accordingly, soluble PAC with obvious dark activity is not the ideal tool for precise manipulation of cAMP signaling in the microdomain. A step forward could be using the dark activity reduced bPAC mutants in combination with two-photon excitation laser-scanning microscopy for precise local activation. As bPAC has been shown to be well activated by two-photon excitation [139]. Still, due to the intrinsic diffusion problem of all soluble proteins, membrane-anchored bPACs would be a better choice for the intervention of the confined microdomain cAMP signaling. For example, when targeting bPAC to the pre- or post-synaptic region, cAMP related signaling role in synaptic plasticity could be investigated in unprecedented details with the help of two-photon excitation. It allows investigating whether local pre- or post-

synaptic activation is sufficient to increase the synaptic transmission. In addition, the plasma membrane-anchored bPAC variants could also better mimic the endogenous transmembrane ACs, such as the neural transmembrane ACs [184].

When targeting bPAC to the membrane, less attention was paid to the potential influence on bPAC activity after fusion with membrane anchor, but this is indeed an unneglectable fact. Here I found anchoring bPAC to the plasma membrane with different linkers can remarkably alter its activity. Therefore, when targeting bPAC to other organelle membranes, the possible changes of enzymatic activity should always be taken into consideration. In addition, bPAC could be combined with CNG channel to generate light-gated CNG channels. The transmembrane CNG channel *per se* is a membrane anchor. Therefore, the fusion strategy for combining bPAC and CNG channel should be optimized accordingly.

4.3.4 N-terminal YFP-tagged RhAC for fast control of cAMP in cell

Aside from PACs, the enzyme rhodopsin BeCyclOp and CaCyclOp could also be converted from GCs to ACs by introducing the point mutations E497K/C566D. When fusion with a YFP tag, we found that the N-terminally tagged CaCyclOp (YFP-CaCyclOp) showed lower dark activity than C-terminal tagged one (CaCyclOp-YFP) (Fig. 3.16B). Moreover, YFP-CaRhAC also showed better performance in hippocampal neurons than untagged CaRhAC [189]. The underlying mechanism is not clear, possibly due to better expression and/or better membrane-targeting of the N-terminally tagged version. In comparison to the soluble PACs, YFP-CaRhAC allows much faster control of intracellular cAMP due to its fast-kinetic (ms time-scale) property. In addition, as a transmembrane protein, it could also better mimic the endogenous transmembrane ACs [190].

4.4 Discussion for dual-color optogenetics project

4.4.1 Different kinetic properties of vf-Chrimson upon blue and red light stimulation

Red light activated ion channel is always appreciated for *in-vivo* application, for its high penetration ability and low phototoxicity. Chrimson is so far identified the most red-shifted ion channel. Despite the peaking activation at 590 nm, Chrimson still retains robust responses to the blue range light. Accelerated channel kinetic property normally accompanies reduced light sensitivity. Indeed, vf-Chrimson shows lower light sensitivity than wt-Chrimson (K_m for 594 nm light: 1.94 mW/mm² vs 0.12 mW/mm²) [103]. It would be a valuable character for dual-color optogenetics if the light sensitivity at the blue range is also reduced. However, here I found upon blue light illumination, vf-Chrimson displays slowed channel open and close rate, suggesting the possible elevated blue light sensitivity compared with wt-Chrimson. When combining with other blue light drivable actuator, a pulsed blue light illumination is helpful to reduce the crosstalk (Fig. 3.21B-C). The significant different kinetic properties of vf-Chrimson (and Chrimson-S169A, own unpublished data) induced by different wavelengths light illumination are very unusual, possibly due to different photochemical processes underlying different light stimuli. Blue/violet light may catalyze the formation of certain long-lived photo-intermediate of vf-Chrimson.

4.4.2 Two-component system for optogenetic silencing

Considering the importance of K⁺ for setting the membrane potential, light-gated K⁺ channels would allow rapid inhibition of neurons with little effect on other ion gradients. Due to the difficulties in engineering K⁺ channel from ChRs, alternative efforts were applied to generate two-component light gated potassium channels via combining bPAC and cAMP gated SthK channel. Considering the ubiquitous role of cAMP, it's crucial to optimize the synthetic channel with low cAMP production in dark and light. As shown in Fig. 3.12, soluble wt-bPAC exhibits obvious dark activity. Therefore, the split PAC-K (here SthK-P2A-bPAC-YFP) may suffer the dark activity induced problems when high protein expression is needed. On the contrary, SthK-bPAC exhibits the lowest cAMP production in dark and generates the highest photocurrent

with the lowest bulk cAMP increase after illumination (Fig. 3.19). These superior characters are contributed from two aspects: (1) the tandem structure makes the SthK close to bPAC, enabling locally activation of SthK by cAMP with very little diffusion effect. On the contrary, to generate similar outward K^+ current, split PAC-K will cause higher bulk increase of cAMP than SthK-bP due to the spatial distance of soluble bPAC and membrane-bound SthK. (2) Proper fusion of bPAC with membrane anchor (SthK) could reduce the dark activity of bPAC. In addition, anchoring bPAC to the membrane was shown to alter its activity (Fig. 3.13E). Consistent with this, here I found that SthK-bP and bPAC-L-SthK-T2A-YFP indeed displayed considerable differences in both dark and light activity. The high dark activity constrains its application in these cell types with low PDE activity. Taken together, the comparisons of three two-component light-gated K^+ channels highlighted the importance of optimization of optogenetic tools.

4.4.3 Minimalization of the crosstalk

Almost all current two-color optogenetic experiments still didn't fully achieve two-color separation. Therefore, it's important to develop experimental setups to minimize the crosstalk to a subthreshold level. The most straightforward way is to select the most action spectrum distinct tool pair. A step forward way is introducing differences in blue light sensitivity between blue and red light-drivable optogenetic tools. Then low intensity blue light could trigger reliable response through activation of blue light-drivable actuator, while only very tiny, below subthreshold response comes from the red light-drivable tools. The light sensitivity difference is mainly contributed by two parts: the protein sensitivity to blue light itself and protein level difference. Here in this study, two strategies are both adapted. First, the inhibitor tool SthK(TV418)-bP has very high blue light sensitivity *per se*. Second, when expressing proteins in oocytes, SthK(TV418)-bP is injected 2 folds higher molar amount of cRNA than vf-Chrimson 2.0. Whenever possible, SthK(TV418)-bP should be expressed under the stronger promoter to minimize vf-Chrimson-induced depolarization. The relatively low protein level of vf-Chrimson 2.0 could be compensated by using high intensity red light for activation. Moreover, here I found that the light illumination scheme could

also be exploited to minimize the crosstalk, in addition to adjusting light wavelength and intensity. As bPAC has relatively long turnover time and the ability to integrate light over time, pulsed light could be used to active bPAC. Additionally, pulsed light illumination also minimizes the activation of vf-Chrimson 2.0. Taken together, these three strategies exemplified here enables robust bidirectional control of cell activity. Aside from bidirectional control of the activity within the same cell, it's also feasible to independently bidirectional manipulate the membrane potential of these genetically distinct, but anatomically intermingled cell populations. Furthermore, when combining with advanced light delivery instruments for confined or patterned illumination, it might be possible to enable the *in-vivo* dual-color experiment by using this toolset.

5. References:

1. Deisseroth, K., et al., *Next-generation optical technologies for illuminating genetically targeted brain circuits*. J Neurosci, 2006. **26**(41): p. 10380-6.
2. Govorunova, E.G., et al., *Microbial Rhodopsins: Diversity, Mechanisms, and Optogenetic Applications*. Annu Rev Biochem, 2017. **86**: p. 845-872.
3. Crick, F.H., *Thinking about the brain*. Sci Am, 1979. **241**(3): p. 219-32.
4. Crick, F., *The impact of molecular biology on neuroscience*. Philos Trans R Soc Lond B Biol Sci, 1999. **354**(1392): p. 2021-5.
5. Zemelman, B.V., et al., *Selective photostimulation of genetically chARGed neurons*. Neuron, 2002. **33**(1): p. 15-22.
6. Banghart, M., et al., *Light-activated ion channels for remote control of neuronal firing*. Nat Neurosci, 2004. **7**(12): p. 1381-6.
7. Lima, S.Q. and G. Miesenbock, *Remote control of behavior through genetically targeted photostimulation of neurons*. Cell, 2005. **121**(1): p. 141-52.
8. Nagel, G., et al., *Channelrhodopsin-1: a light-gated proton channel in green algae*. Science, 2002. **296**(5577): p. 2395-8.
9. Nagel, G., et al., *Channelrhodopsin-2, a directly light-gated cation-selective membrane channel*. Proc Natl Acad Sci U S A, 2003. **100**(24): p. 13940-5.
10. Boyden, E.S., et al., *Millisecond-timescale, genetically targeted optical control of neural activity*. Nat Neurosci, 2005. **8**(9): p. 1263-8.
11. Ishizuka, T., et al., *Kinetic evaluation of photosensitivity in genetically engineered neurons expressing green algae light-gated channels*. Neurosci Res, 2006. **54**(2): p. 85-94.
12. Li, X., et al., *Fast noninvasive activation and inhibition of neural and network activity by vertebrate rhodopsin and green algae channelrhodopsin*. Proc Natl Acad Sci U S A, 2005. **102**(49): p. 17816-21.
13. Bi, A., et al., *Ectopic expression of a microbial-type rhodopsin restores visual responses in mice with photoreceptor degeneration*. Neuron, 2006. **50**(1): p. 23-33.
14. Nagel, G., et al., *Light activation of channelrhodopsin-2 in excitable cells of Caenorhabditis elegans triggers rapid behavioral responses*. Curr Biol, 2005. **15**(24): p. 2279-84.
15. Schroll, C., et al., *Light-induced activation of distinct modulatory neurons triggers appetitive or aversive learning in Drosophila larvae*. Curr Biol, 2006. **16**(17): p. 1741-7.
16. Zhang, F., et al., *Multimodal fast optical interrogation of neural circuitry*. Nature, 2007. **446**(7136): p. 633-9.
17. Han, X. and E.S. Boyden, *Multiple-color optical activation, silencing, and desynchronization of neural activity, with single-spike temporal resolution*. PLoS One, 2007. **2**(3): p. e299.
18. Schroder-Lang, S., et al., *Fast manipulation of cellular cAMP level by light in vivo*. Nat Methods, 2007. **4**(1): p. 39-42.
19. Airan, R.D., et al., *Temporally precise in vivo control of intracellular signalling*. Nature, 2009. **458**(7241): p. 1025-9.
20. Oesterhelt, D. and W. Stoeckenius, *Rhodopsin-like protein from the purple membrane of Halobacterium halobium*. Nat New Biol, 1971. **233**(39): p. 149-52.
21. Oesterhelt, D. and W. Stoeckenius, *Functions of a new photoreceptor membrane*. Proc Natl Acad Sci U S A, 1973. **70**(10): p. 2853-7.

22. Racker, E. and W. Stoeckenius, *Reconstitution of purple membrane vesicles catalyzing light-driven proton uptake and adenosine triphosphate formation*. J Biol Chem, 1974. **249**(2): p. 662-3.
23. Mitchell, P., *Keilin's respiratory chain concept and its chemiosmotic consequences*. Science, 1979. **206**(4423): p. 1148-59.
24. Song, Y. and M.R. Gunner, *Halorhodopsin pumps Cl⁻ and bacteriorhodopsin pumps protons by a common mechanism that uses conserved electrostatic interactions*. Proc Natl Acad Sci U S A, 2014. **111**(46): p. 16377-82.
25. Mak-Jurkauskas, M.L., et al., *Energy transformations early in the bacteriorhodopsin photocycle revealed by DNP-enhanced solid-state NMR*. Proc Natl Acad Sci U S A, 2008. **105**(3): p. 883-8.
26. Nagel, G., et al., *Functional expression of bacteriorhodopsin in oocytes allows direct measurement of voltage dependence of light induced H⁺ pumping*. FEBS Lett, 1995. **377**(2): p. 263-6.
27. Chow, B.Y., et al., *High-performance genetically targetable optical neural silencing by light-driven proton pumps*. Nature, 2010. **463**(7277): p. 98-102.
28. Matsuno-Yagi, A. and Y. Mukohata, *Two possible roles of bacteriorhodopsin; a comparative study of strains of Halobacterium halobium differing in pigmentation*. Biochem Biophys Res Commun, 1977. **78**(1): p. 237-43.
29. Mukohata, Y. and Y. Kaji, *Light-induced membrane-potential increase, ATP synthesis, and proton uptake in Halobacterium halobium, R1mR catalyzed by halorhodopsin: Effects of N,N'-dicyclohexylcarbodiimide, triphenyltin chloride, and 3,5-di-tert-butyl-4-hydroxybenzylidenemalononitrile (SF6847)*. Arch Biochem Biophys, 1981. **206**(1): p. 72-6.
30. Greene, R.V. and J.K. Lanyi, *Proton movements in response to a light-driven electrogenic pump for sodium ions in Halobacterium halobium membranes*. J Biol Chem, 1979. **254**(21): p. 10986-94.
31. MacDonald, R.E., et al., *Characterization of the light-driven sodium pump of Halobacterium halobium. Consequences of sodium efflux as the primary light-driven event*. J Biol Chem, 1979. **254**(23): p. 11831-8.
32. Schobert, B. and J.K. Lanyi, *Halorhodopsin is a light-driven chloride pump*. J Biol Chem, 1982. **257**(17): p. 10306-13.
33. Barnberg, E., P. Hegemann, and D. Oesterhelt, *The chromoprotein of halorhodopsin is the light-driven electrogenic chloride pump in halobacterium halobium*. Biochemistry, 1984. **23**(25): p. 6216-21.
34. Bivin, D.B. and W. Stoeckenius, *Photoactive retinal pigments in haloalkaliphilic bacteria*. J Gen Microbiol, 1986. **132**(8): p. 2167-77.
35. Duschl, A., J.K. Lanyi, and L. Zimanyi, *Properties and photochemistry of a halorhodopsin from the haloalkalophile, Natronobacterium pharaonis*. J Biol Chem, 1990. **265**(3): p. 1261-7.
36. Blanck, A. and D. Oesterhelt, *The halo-opsin gene. II. Sequence, primary structure of halorhodopsin and comparison with bacteriorhodopsin*. EMBO J, 1987. **6**(1): p. 265-73.
37. Lanyi, J.K., et al., *The primary structure of a halorhodopsin from Natronobacterium pharaonis. Structural, functional and evolutionary implications for bacterial rhodopsins and halorhodopsins*. J Biol Chem, 1990. **265**(3): p. 1253-60.

38. Kolbe, M., et al., *Structure of the light-driven chloride pump halorhodopsin at 1.8 Å resolution*. Science, 2000. **288**(5470): p. 1390-6.
39. Kouyama, T., et al., *Crystal structure of the light-driven chloride pump halorhodopsin from Natronomonas pharaonis*. J Mol Biol, 2010. **396**(3): p. 564-79.
40. Engelhard, C., et al., *Microbial Halorhodopsins: Light-Driven Chloride Pumps*. Chem Rev, 2018. **118**(21): p. 10629-10645.
41. Kouyama, T., et al., *Crystal structures of the L1, L2, N, and O states of pharaonis halorhodopsin*. Biophys J, 2015. **108**(11): p. 2680-90.
42. Kleinlogel, S., et al., *A gene-fusion strategy for stoichiometric and co-localized expression of light-gated membrane proteins*. Nat Methods, 2011. **8**(12): p. 1083-8.
43. Feroz, H., et al., *Light-Driven Chloride Transport Kinetics of Halorhodopsin*. Biophys J, 2018. **115**(2): p. 353-360.
44. Zhao, S., et al., *Improved expression of halorhodopsin for light-induced silencing of neuronal activity*. Brain Cell Biol, 2008. **36**(1-4): p. 141-54.
45. Gradinaru, V., K.R. Thompson, and K. Deisseroth, *eNpHR: a Natronomonas halorhodopsin enhanced for optogenetic applications*. Brain Cell Biol, 2008. **36**(1-4): p. 129-39.
46. Gradinaru, V., et al., *Molecular and cellular approaches for diversifying and extending optogenetics*. Cell, 2010. **141**(1): p. 154-165.
47. Inoue, K., et al., *A light-driven sodium ion pump in marine bacteria*. Nat Commun, 2013. **4**: p. 1678.
48. Gushchin, I., et al., *Crystal structure of a light-driven sodium pump*. Nat Struct Mol Biol, 2015. **22**(5): p. 390-5.
49. Kato, H.E., et al., *Structural basis for Na(+) transport mechanism by a light-driven Na(+) pump*. Nature, 2015. **521**(7550): p. 48-53.
50. Kovalev, K., et al., *Structure and mechanisms of sodium-pumping KR2 rhodopsin*. Sci Adv, 2019. **5**(4): p. eaav2671.
51. Grimm, C., et al., *Electrical properties, substrate specificity and optogenetic potential of the engineered light-driven sodium pump eKR2*. Sci Rep, 2018. **8**(1): p. 9316.
52. Foster, K.W. and R.D. Smyth, *Light Antennas in phototactic algae*. Microbiol Rev, 1980. **44**(4): p. 572-630.
53. Litvin, F.F., O.A. Sineshchekov, and V.A. Sineshchekov, *Photoreceptor electric potential in the phototaxis of the alga Haematococcus pluvialis*. Nature, 1978. **271**(5644): p. 476-8.
54. Foster, K.W., et al., *A rhodopsin is the functional photoreceptor for phototaxis in the unicellular eukaryote Chlamydomonas*. Nature, 1984. **311**(5988): p. 756-9.
55. Harz, H. and P. Hegemann, *Rhodopsin-Regulated Calcium Currents in Chlamydomonas*. Nature, 1991. **351**(6326): p. 489-491.
56. Braun, F.J. and P. Hegemann, *Two light-activated conductances in the eye of the green alga Volvox carteri*. Biophys J, 1999. **76**(3): p. 1668-78.
57. Sineshchekov, O.A., K.H. Jung, and J.L. Spudich, *Two rhodopsins mediate phototaxis to low- and high-intensity light in Chlamydomonas reinhardtii*. Proc Natl Acad Sci U S A, 2002. **99**(13): p. 8689-94.
58. Suzuki, T., et al., *Archaeal-type rhodopsins in Chlamydomonas: model structure and intracellular localization*. Biochem Biophys Res Commun, 2003. **301**(3): p. 711-7.
59. Hegemann, P. and G. Nagel, *From channelrhodopsins to optogenetics*. EMBO Mol Med,

2013. **5**(2): p. 173-6.
60. Muller, M., et al., *Projection structure of channelrhodopsin-2 at 6 Å resolution by electron crystallography*. J Mol Biol, 2011. **414**(1): p. 86-95.
61. Kato, H.E., et al., *Crystal structure of the channelrhodopsin light-gated cation channel*. Nature, 2012. **482**(7385): p. 369-74.
62. Inaguma, A., et al., *Chimeras of channelrhodopsin-1 and -2 from Chlamydomonas reinhardtii exhibit distinctive light-induced structural changes from channelrhodopsin-2*. J Biol Chem, 2015. **290**(18): p. 11623-34.
63. Volkov, O., et al., *Structural insights into ion conduction by channelrhodopsin 2*. Science, 2017. **358**(6366).
64. Bamann, C., et al., *Structural guidance of the photocycle of channelrhodopsin-2 by an interhelical hydrogen bond*. Biochemistry, 2010. **49**(2): p. 267-78.
65. Berndt, A., et al., *Bi-stable neural state switches*. Nat Neurosci, 2009. **12**(2): p. 229-34.
66. Dawydow, A., et al., *Channelrhodopsin-2-XXL, a powerful optogenetic tool for low-light applications*. Proc Natl Acad Sci U S A, 2014. **111**(38): p. 13972-7.
67. Scholz, N., et al., *Mechano-dependent signaling by Latrophilin/CIRL quenches cAMP in proprioceptive neurons*. Elife, 2017. **6**.
68. Duan, X.D., G. Nagel, and S.Q. Gao, *Mutated Channelrhodopsins with Increased Sodium and Calcium Permeability*. Applied Sciences-Basel, 2019. **9**(4).
69. Schneider, F., C. Grimm, and P. Hegemann, *Biophysics of Channelrhodopsin*. Annu Rev Biophys, 2015. **44**: p. 167-86.
70. Hegemann, P., S. Ehlenbeck, and D. Gradmann, *Multiple photocycles of channelrhodopsin*. Biophys J, 2005. **89**(6): p. 3911-8.
71. Nikolic, K., et al., *Photocycles of channelrhodopsin-2*. Photochem Photobiol, 2009. **85**(1): p. 400-11.
72. Stehfest, K. and P. Hegemann, *Evolution of the channelrhodopsin photocycle model*. Chemphyschem, 2010. **11**(6): p. 1120-6.
73. Kuhne, J., et al., *Unifying photocycle model for light adaptation and temporal evolution of cation conductance in channelrhodopsin-2*. Proc Natl Acad Sci U S A, 2019. **116**(19): p. 9380-9389.
74. Lorenz-Fonfria, V.A. and J. Heberle, *Channelrhodopsin unchained: structure and mechanism of a light-gated cation channel*. Biochim Biophys Acta, 2014. **1837**(5): p. 626-42.
75. Berndt, A., et al., *Two open states with progressive proton selectivities in the branched channelrhodopsin-2 photocycle*. Biophys J, 2010. **98**(5): p. 753-61.
76. Schneider, F., D. Gradmann, and P. Hegemann, *Ion selectivity and competition in channelrhodopsins*. Biophys J, 2013. **105**(1): p. 91-100.
77. Berndt, A., et al., *Structure-guided transformation of channelrhodopsin into a light-activated chloride channel*. Science, 2014. **344**(6182): p. 420-4.
78. Wietek, J., et al., *Conversion of channelrhodopsin into a light-gated chloride channel*. Science, 2014. **344**(6182): p. 409-12.
79. Wietek, J., et al., *An improved chloride-conducting channelrhodopsin for light-induced inhibition of neuronal activity in vivo*. Sci Rep, 2015. **5**: p. 14807.
80. Berndt, A., et al., *Structural foundations of optogenetics: Determinants of*

- channelrhodopsin ion selectivity*. Proc Natl Acad Sci U S A, 2016. **113**(4): p. 822-9.
81. Kleinlogel, S., et al., *Ultra light-sensitive and fast neuronal activation with the Ca(2)+-permeable channelrhodopsin CatCh*. Nat Neurosci, 2011. **14**(4): p. 513-8.
82. Gaiko, O. and R.E. Dempski, *Transmembrane domain three contributes to the ion conductance pathway of channelrhodopsin-2*. Biophys J, 2013. **104**(6): p. 1230-7.
83. Eisenhauer, K., et al., *In channelrhodopsin-2 Glu-90 is crucial for ion selectivity and is deprotonated during the photocycle*. J Biol Chem, 2012. **287**(9): p. 6904-11.
84. Richards, R. and R.E. Dempski, *Adjacent channelrhodopsin-2 residues within transmembranes 2 and 7 regulate cation selectivity and distribution of the two open states*. J Biol Chem, 2017. **292**(18): p. 7314-7326.
85. Klapoetke, N.C., et al., *Independent optical excitation of distinct neural populations*. Nat Methods, 2014. **11**(3): p. 338-46.
86. Vierock, J., et al., *Molecular determinants of proton selectivity and gating in the red-light activated channelrhodopsin Chrimson*. Sci Rep, 2017. **7**(1): p. 9928.
87. Govorunova, E.G., et al., *Characterization of a highly efficient blue-shifted channelrhodopsin from the marine alga *Platymonas subcordiformis**. J Biol Chem, 2013. **288**(41): p. 29911-22.
88. Oda, K., et al., *Crystal structure of the red light-activated channelrhodopsin Chrimson*. Nat Commun, 2018. **9**(1): p. 3949.
89. Zhang, F., et al., *Red-shifted optogenetic excitation: a tool for fast neural control derived from *Volvox carteri**. Nat Neurosci, 2008. **11**(6): p. 631-3.
90. Yizhar, O., et al., *Neocortical excitation/inhibition balance in information processing and social dysfunction*. Nature, 2011. **477**(7363): p. 171-8.
91. Lin, J.Y., et al., *ReaChR: a red-shifted variant of channelrhodopsin enables deep transcranial optogenetic excitation*. Nat Neurosci, 2013. **16**(10): p. 1499-508.
92. Prakash, R., et al., *Two-photon optogenetic toolbox for fast inhibition, excitation and bistable modulation*. Nat Methods, 2012. **9**(12): p. 1171-9.
93. Chen, S., et al., *Near-infrared deep brain stimulation via upconversion nanoparticle-mediated optogenetics*. Science, 2018. **359**(6376): p. 679-684.
94. Berndt, A., et al., *High-efficiency channelrhodopsins for fast neuronal stimulation at low light levels*. Proc Natl Acad Sci U S A, 2011. **108**(18): p. 7595-600.
95. Wen, L., et al., *Opto-current-clamp actuation of cortical neurons using a strategically designed channelrhodopsin*. PLoS One, 2010. **5**(9): p. e12893.
96. Lin, J.Y., et al., *Characterization of engineered channelrhodopsin variants with improved properties and kinetics*. Biophys J, 2009. **96**(5): p. 1803-14.
97. Gunaydin, L.A., et al., *Ultrafast optogenetic control*. Nat Neurosci, 2010. **13**(3): p. 387-92.
98. Wang, H., et al., *Molecular determinants differentiating photocurrent properties of two channelrhodopsins from *chlamydomonas**. J Biol Chem, 2009. **284**(9): p. 5685-96.
99. Cho, Y.K., et al., *Multidimensional screening yields channelrhodopsin variants having improved photocurrent and order-of-magnitude reductions in calcium and proton currents*. J Biol Chem, 2019. **294**(11): p. 3806-3821.
100. Kato, H.E., et al., *Structural mechanisms of selectivity and gating in anion channelrhodopsins*. Nature, 2018. **561**(7723): p. 349-354.
101. Govorunova, E.G., et al., *NEUROSCIENCE. Natural light-gated anion channels: A family of*

- microbial rhodopsins for advanced optogenetics*. Science, 2015. **349**(6248): p. 647-50.
102. Kim, Y.S., et al., *Crystal structure of the natural anion-conducting channelrhodopsin GtACR1*. Nature, 2018. **561**(7723): p. 343-348.
103. Mager, T., et al., *High frequency neural spiking and auditory signaling by ultrafast red-shifted optogenetics*. Nat Commun, 2018. **9**(1): p. 1750.
104. Marshel, J.H., et al., *Cortical layer-specific critical dynamics triggering perception*. Science, 2019. **365**(6453).
105. Bedbrook, C.N., et al., *Machine learning-guided channelrhodopsin engineering enables minimally-invasive optogenetics*. bioRxiv, 2019.
106. Iseki, M., et al., *A blue-light-activated adenylyl cyclase mediates photoavoidance in Euglena gracilis*. Nature, 2002. **415**(6875): p. 1047-51.
107. Looser, J., et al., *Mechanistic insights in light-induced cAMP production by photoactivated adenylyl cyclase alpha (PACalpha)*. Biol Chem, 2009. **390**(11): p. 1105-11.
108. Nagahama, T., et al., *Functional transplant of photoactivated adenylyl cyclase (PAC) into Aplysia sensory neurons*. Neuroscience Research, 2007. **59**(1): p. 81-88.
109. Weissenberger, S., et al., *PACalpha--an optogenetic tool for in vivo manipulation of cellular cAMP levels, neurotransmitter release, and behavior in Caenorhabditis elegans*. J Neurochem, 2011. **116**(4): p. 616-25.
110. Stierl, M., et al., *Light modulation of cellular cAMP by a small bacterial photoactivated adenylyl cyclase, bPAC, of the soil bacterium Beggiatoa*. J Biol Chem, 2011. **286**(2): p. 1181-8.
111. Ryu, M.H., et al., *Natural and engineered photoactivated nucleotidyl cyclases for optogenetic applications*. J Biol Chem, 2010. **285**(53): p. 41501-8.
112. Jansen, V., et al., *Controlling fertilization and cAMP signaling in sperm by optogenetics*. Elife, 2015. **4**.
113. Xiao, Y., W. Tian, and H. Lopez-Schier, *Optogenetic stimulation of neuronal repair*. Curr Biol, 2015. **25**(22): p. R1068-9.
114. Costa, W.S., et al., *Fast cAMP Modulation of Neurotransmission via Neuropeptide Signals and Vesicle Loading*. Current Biology, 2017. **27**(4): p. 495-507.
115. Zhang, K. and B.X. Cu, *Optogenetic control of intracellular signaling pathways*. Trends in Biotechnology, 2015. **33**(2): p. 92-100.
116. Stierl, M., et al., *Key residues for the light regulation of the blue light-activated adenylyl cyclase from Beggiatoa sp*. Biochemistry, 2014. **53**(31): p. 5121-30.
117. Lindner, R., et al., *Photoactivation Mechanism of a Bacterial Light-Regulated Adenylyl Cyclase*. J Mol Biol, 2017. **429**(9): p. 1336-1351.
118. Ohki, M., et al., *Structural insight into photoactivation of an adenylate cyclase from a photosynthetic cyanobacterium*. Proceedings of the National Academy of Sciences of the United States of America, 2016. **113**(24): p. 6659-6664.
119. Penzkofer, A., et al., *Photo-dynamics of the BLUF domain containing soluble adenylate cyclase (nPAC) from the amoeboflagellate Naegleria gruberi NEG-M strain*. Chemical Physics, 2011. **387**(1-3): p. 25-38.
120. Penzkofer, A., et al., *Photo-dynamics of photoactivated adenylyl cyclase TpPAC from the spirochete bacterium Turneriella parva strain H-T*. Journal of Photochemistry and Photobiology B-Biology, 2015. **153**: p. 90-102.

121. Raffelberg, S., et al., *A LOV-domain-mediated blue-light-activated adenylyl cyclase from the cyanobacterium Microcoleus chthonoplastes PCC 7420*. *Biochemical Journal*, 2013. **455**: p. 359-365.
122. Blain-Hartung, M., et al., *Cyanobacteriochrome-based photoswitchable adenylyl cyclases (cPACs) for broad spectrum light regulation of cAMP levels in cells*. *J Biol Chem*, 2018. **293**(22): p. 8473-8483.
123. Stuvén, B., et al., *Characterization and engineering of photoactivated adenylyl cyclases*. *Biol Chem*, 2019. **400**(3): p. 429-441.
124. Avelar, G.M., et al., *A rhodopsin-guanylyl cyclase gene fusion functions in visual perception in a fungus*. *Curr Biol*, 2014. **24**(11): p. 1234-40.
125. Gao, S., et al., *Optogenetic manipulation of cGMP in cells and animals by the tightly light-regulated guanylyl-cyclase opsin CyclOp*. *Nat Commun*, 2015. **6**: p. 8046.
126. Scheib, U., et al., *The rhodopsin-guanylyl cyclase of the aquatic fungus Blastocladiella emersonii enables fast optical control of cGMP signaling*. *Sci Signal*, 2015. **8**(389): p. rs8.
127. Yoshida, K., et al., *A unique choanoflagellate enzyme rhodopsin exhibits light-dependent cyclic nucleotide phosphodiesterase activity*. *J Biol Chem*, 2017. **292**(18): p. 7531-7541.
128. Lamarche, L.B., et al., *Purification and Characterization of RhoPDE, a Retinylidene/Phosphodiesterase Fusion Protein and Potential Optogenetic Tool from the Choanoflagellate Salpingoeca rosetta*. *Biochemistry*, 2017. **56**(43): p. 5812-5822.
129. Tian, Y., et al., *A novel rhodopsin phosphodiesterase from Salpingoeca rosetta shows light-enhanced substrate affinity*. *Biochem J*, 2018. **475**(6): p. 1121-1128.
130. Brunet, T., et al., *Light-regulated collective contractility in a multicellular choanoflagellate*. *Science*, 2019. **366**(6463): p. 326-334.
131. Tian, Y., et al., *Two-component cyclase opsins of green algae are ATP-dependent and light-inhibited guanylyl cyclases*. *BMC Biol*, 2018. **16**(1): p. 144.
132. Raimondo, J.V., et al., *Optogenetic silencing strategies differ in their effects on inhibitory synaptic transmission*. *Nat Neurosci*, 2012. **15**(8): p. 1102-4.
133. Alfonso, H., et al., *The contribution of raised intraneuronal chloride to epileptic network activity*. *J Neurosci*, 2015. **35**(20): p. 7715-26.
134. Mahn, M., et al., *Biophysical constraints of optogenetic inhibition at presynaptic terminals*. *Nat Neurosci*, 2016. **19**(4): p. 554-6.
135. Sorensen, A.T., et al., *Altered Chloride Homeostasis Decreases the Action Potential Threshold and Increases Hyperexcitability in Hippocampal Neurons*. *eNeuro*, 2017. **4**(6).
136. Wiegert, J.S. and T.G. Oertner, *How (not) to silence long-range projections with light*. *Nat Neurosci*, 2016. **19**(4): p. 527-8.
137. Cosentino, C., et al., *Optogenetics. Engineering of a light-gated potassium channel*. *Science*, 2015. **348**(6235): p. 707-10.
138. Beck, S., et al., *Synthetic Light-Activated Ion Channels for Optogenetic Activation and Inhibition*. *Front Neurosci*, 2018. **12**: p. 643.
139. Bernal Sierra, Y.A., et al., *Potassium channel-based optogenetic silencing*. *Nat Commun*, 2018. **9**(1): p. 4611.
140. Gasser, C., et al., *Engineering of a red-light-activated human cAMP/cGMP-specific phosphodiesterase*. *Proc Natl Acad Sci U S A*, 2014. **111**(24): p. 8803-8.
141. Bedbrook, C.N., et al., *Machine learning to design integral membrane channelrhodopsins*

- for efficient eukaryotic expression and plasma membrane localization. *PLoS Comput Biol*, 2017. **13**(10): p. e1005786.
142. Tkatch, T., et al., *Optogenetic control of mitochondrial metabolism and Ca(2+) signaling by mitochondria-targeted opsins*. *Proc Natl Acad Sci U S A*, 2017. **114**(26): p. E5167-E5176.
143. Mahn, M., et al., *High-efficiency optogenetic silencing with soma-targeted anion-conducting channelrhodopsins*. *Nat Commun*, 2018. **9**(1): p. 4125.
144. Brown, J., et al., *Expanding the Optogenetics Toolkit by Topological Inversion of Rhodopsins*. *Cell*, 2018. **175**(4): p. 1131-1140 e11.
145. Cole, K.S. and H.J. Curtis, *Electric Impedance of the Squid Giant Axon during Activity*. *J Gen Physiol*, 1939. **22**(5): p. 649-70.
146. Guan, B., X. Chen, and H. Zhang, *Two-electrode voltage clamp*. *Methods Mol Biol*, 2013. **998**: p. 79-89.
147. Beppu, K., et al., *Optogenetic countering of glial acidosis suppresses glial glutamate release and ischemic brain damage*. *Neuron*, 2014. **81**(2): p. 314-20.
148. Watanabe, H.C., et al., *Structural model of channelrhodopsin*. *J Biol Chem*, 2012. **287**(10): p. 7456-66.
149. Figueiredo, M., et al., *Comparative analysis of optogenetic actuators in cultured astrocytes*. *Cell Calcium*, 2014. **56**(3): p. 208-14.
150. Perea, G., et al., *Optogenetic astrocyte activation modulates response selectivity of visual cortex neurons in vivo*. *Nat Commun*, 2014. **5**: p. 3262.
151. Masseck, O.A., et al., *Vertebrate cone opsins enable sustained and highly sensitive rapid control of Gi/o signaling in anxiety circuitry*. *Neuron*, 2014. **81**(6): p. 1263-1273.
152. Siuda, E.R., et al., *Optodynamic simulation of beta-adrenergic receptor signalling*. *Nat Commun*, 2015. **6**: p. 8480.
153. Chuong, A.S., et al., *Noninvasive optical inhibition with a red-shifted microbial rhodopsin*. *Nat Neurosci*, 2014. **17**(8): p. 1123-9.
154. Szabadics, J., et al., *Excitatory effect of GABAergic axo-axonic cells in cortical microcircuits*. *Science*, 2006. **311**(5758): p. 233-5.
155. Price, G.D. and L.O. Trussell, *Estimate of the chloride concentration in a central glutamatergic terminal: a gramicidin perforated-patch study on the calyx of Held*. *J Neurosci*, 2006. **26**(44): p. 11432-6.
156. Bamberg, E., J. Tittor, and D. Oesterhelt, *Light-driven proton or chloride pumping by halorhodopsin*. *Proc Natl Acad Sci U S A*, 1993. **90**(2): p. 639-43.
157. Kanada, S., et al., *Crystal structures of an O-like blue form and an anion-free yellow form of pharaonis halorhodopsin*. *J Mol Biol*, 2011. **413**(1): p. 162-76.
158. Zhang, C., et al., *Optimized photo-stimulation of halorhodopsin for long-term neuronal inhibition*. *BMC Biol*, 2019. **17**(1): p. 95.
159. Bos, J.L., *Epac: a new cAMP target and new avenues in cAMP research*. *Nature Reviews Molecular Cell Biology*, 2003. **4**(9): p. 733-738.
160. Montminy, M.R. and L.M. Bilezikjian, *Binding of a Nuclear-Protein to the Cyclic-Amp Response Element of the Somatostatin Gene*. *Nature*, 1987. **328**(6126): p. 175-178.
161. Lefkimmiatis, K. and M. Zaccolo, *cAMP signaling in subcellular compartments*. *Pharmacol Ther*, 2014. **143**(3): p. 295-304.

162. Tanwar, M., et al., *Modulation of cyclic nucleotide-mediated cellular signaling and gene expression using photoactivated adenylyl cyclase as an optogenetic tool*. Scientific Reports, 2017. **7**.
163. Tsvetanova, N.G. and M. von Zastrow, *Spatial encoding of cyclic AMP signaling specificity by GPCR endocytosis*. Nat Chem Biol, 2014. **10**(12): p. 1061-5.
164. Steegborn, C., *Structure, mechanism, and regulation of soluble adenylyl cyclases - similarities and differences to transmembrane adenylyl cyclases*. Biochim Biophys Acta, 2014. **1842**(12 Pt B): p. 2535-47.
165. Sunahara, R.K., et al., *Exchange of substrate and inhibitor specificities between adenylyl and guanylyl cyclases*. J Biol Chem, 1998. **273**(26): p. 16332-8.
166. Linder, J.U., *Substrate selection by class III adenylyl cyclases and guanylyl cyclases*. IUBMB Life, 2005. **57**(12): p. 797-803.
167. Trieu, M.M., et al., *Expression, purification, and spectral tuning of RhoGC, a retinylidene/guanylyl cyclase fusion protein and optogenetics tool from the aquatic fungus *Blastocladiella emersonii**. J Biol Chem, 2017. **292**(25): p. 10379-10389.
168. Zhang, F., et al., *The microbial opsin family of optogenetic tools*. Cell, 2011. **147**(7): p. 1446-57.
169. Shepard, B.D., et al., *A cleavable N-terminal signal peptide promotes widespread olfactory receptor surface expression in HEK293T cells*. PLoS One, 2013. **8**(7): p. e68758.
170. Brams, M., et al., *Family of prokaryote cyclic nucleotide-modulated ion channels*. Proc Natl Acad Sci U S A, 2014. **111**(21): p. 7855-60.
171. Kesters, D., et al., *Structure of the SthK carboxy-terminal region reveals a gating mechanism for cyclic nucleotide-modulated ion channels*. PLoS One, 2015. **10**(1): p. e0116369.
172. Feldbauer, K., et al., *Channelrhodopsin-2 is a leaky proton pump*. Proc Natl Acad Sci U S A, 2009. **106**(30): p. 12317-22.
173. Mattis, J., et al., *Principles for applying optogenetic tools derived from direct comparative analysis of microbial opsins*. Nat Methods, 2011. **9**(2): p. 159-72.
174. Zimmermann, D., et al., *Effects on capacitance by overexpression of membrane proteins*. Biochem Biophys Res Commun, 2008. **369**(4): p. 1022-6.
175. Li, H., et al., *Crystal structure of a natural light-gated anion channelrhodopsin*. Elife, 2019. **8**.
176. Hegemann, P., D. Oesterbelt, and M. Steiner, *The photocycle of the chloride pump halorhodopsin. I: Azide-catalyzed deprotonation of the chromophore is a side reaction of photocycle intermediates inactivating the pump*. EMBO J, 1985. **4**(9): p. 2347-50.
177. Lanyi, J.K., *Mechanism of base-catalyzed Schiff base deprotonation in halorhodopsin*. Biochemistry, 1986. **25**(21): p. 6706-11.
178. Steiner, M. and D. Oesterhelt, *Isolation and properties of the native chromoprotein halorhodopsin*. EMBO J, 1983. **2**(8): p. 1379-85.
179. Varo, G., et al., *Light-driven chloride ion transport by halorhodopsin from *Natronobacterium pharaonis*. 1. The photochemical cycle*. Biochemistry, 1995. **34**(44): p. 14490-9.
180. Chizhov, I. and M. Engelhard, *Temperature and halide dependence of the photocycle of halorhodopsin from *Natronobacterium pharaonis**. Biophys J, 2001. **81**(3): p. 1600-12.

181. Mevorat-Kaplan, K., et al., *Effect of anions on the photocycle of halorhodopsin. Substitution of chloride with formate anion*. *Biochemistry*, 2005. **44**(43): p. 14231-7.
182. Oesterhelt, D. and B. Hess, *Reversible photolysis of the purple complex in the purple membrane of Halobacterium halobium*. *Eur J Biochem*, 1973. **37**(2): p. 316-26.
183. Ormos, P., Z. Dancshazy, and B. Karvaly, *Mechanism of generation and regulation of photopotential by bacteriorhodopsin in bimolecular lipid membrane*. *Biochim Biophys Acta*, 1978. **503**(2): p. 304-15.
184. Wiegert, J.S., et al., *Silencing Neurons: Tools, Applications, and Experimental Constraints*. *Neuron*, 2017. **95**(3): p. 504-529.
185. Zhang, K. and B. Cui, *Optogenetic control of intracellular signaling pathways*. *Trends Biotechnol*, 2015. **33**(2): p. 92-100.
186. Rost, B.R., et al., *Optogenetic Tools for Subcellular Applications in Neuroscience*. *Neuron*, 2017. **96**(3): p. 572-603.
187. Musheshe, N., M. Schmidt, and M. Zaccolo, *cAMP: From Long-Range Second Messenger to Nanodomain Signalling*. *Trends Pharmacol Sci*, 2018. **39**(2): p. 209-222.
188. O'Banion, C.P., et al., *Compartmentalized cAMP Generation by Engineered Photoactivated Adenylyl Cyclases*. *Cell Chem Biol*, 2019. **26**(10): p. 1393-1406 e7.
189. Scheib, U., et al., *Rhodopsin-cyclases for photocontrol of cGMP/cAMP and 2.3 A structure of the adenylyl cyclase domain*. *Nat Commun*, 2018. **9**(1): p. 2046.
190. Halls, M.L. and D.M.F. Cooper, *Adenylyl cyclase signalling complexes - Pharmacological challenges and opportunities*. *Pharmacol Ther*, 2017. **172**: p. 171-180.

6. Appendix

6.1 List of primers used in this study

ChR2-E83D-qcF	TGGGAGGACATCTATGTGTGCGCT A
ChR2-E83D-qcR	CATAGATGTCCTCCAGCCGCAGGTT
ChR2-E83N-qcF	TGGGAGAACATCTATGTGTGCGCTA
ChR2-E83N-qcR	CATAGATGTTCTCCAGCCGCAGGTT
ChR2-E83S-qcF	CTGGGAGTCGATCTATGTGTGCGCTA
ChR2-E83S-qcR	CATAGATCGACTCCCAGCCGCAGGTTG
ChR2-E101S-qcF	GAGTTCTTCTTCTCGTTTAAGAACC
ChR2-E101S-qcR	CGAGAAGAAGAACTCGAGAATCACC
ChR2-E101N-qcF	GAGTTCTTCTTCAACTTTAAGAACC
ChR2-E101N-qcR	GTTGAAGAAGAACTCGAGAATCACC
ChR2-E101D-qcF	GAGTTCTTCTTTCGACTTTAAGAACC
ChR2-E101D-qcR	GTCGAAGAAGAACTCGAGAATCACC
ChR2-H114G-qcF	CTAGCCACAGGCGGTCGCGTCCAGTG
ChR2-H114G-qcR	ACCGCCTGTGGCTAGATACAGCATG
ChR2-H134Q-qcF	CATTCTCATTCACTGTCAAACCTG
ChR2-H134Q-qcR	GACAGCTGAATGAGAATGACCGGGC
ChR2309stop-Hd-3R	GGGAAGCTTATACCGCGCCAGCCTC
<i>Np</i> HR-BgBh5F	CGAGAAGATCTGGATCCATG
<i>Np</i> HR-Xh3R	GTCTCCGCTCGAGATCATCA
<i>Np</i> HR-BhKz5F	CGGGATCCGCCACCATGACTGAGACATTG
<i>Np</i> HR- Bgl5F	GAGAAGATCTATGACTGAGACATTG
bPAC-XbMK5F	GCTCTAGAAAGATGAAGCGGCTGGTG
bPAC-XhHA5F	GCCGCTCGAGTATCCATATGATGTTCCAGATTATGCTAAGA TGAAGCGGCTGGTGTAC
bPAC-StopSpHd3R	GCCCAAGCTTAACTAGTCTACAGGTCCTCCTCCGAGATCA
Glycophorin-A-KpKz5F	GGGGTACCGCCACCATGTACGGCA
bPAC-S27A-qcF	CGGATCGGCAAGGTGGCCATCAAGAACAAC
bPAC-S27A-qcR	CCACCTTGCCGATCCGCTGGATCTCTT
bPAC-L123R-qcF	CACCGGGTGCGGGAAAAGTACATGC
bPAC-L123R-qcR	TCCCGCACCCGGTGGCTCTGGGTGAT
bPAC-K197R-qcF	CGAAGTGACCCGGTTCATCGGCGAC
bPAC-K197R-qcR	GAACCGGGTCACTTCGCCGCCGTAG
bPAC-F198Y-qcF	GACCAAATATATTGGCGATTGCGTG
bPAC-F198Y-qcR	GACCAAATATATTGGCGATTGCGTG
bPAC-F198W-qcF	AGTGACCAAGTGGATCGGCGACTGCG

bPAC-F198W-qcR	GATCCACTTGGTCACTTCGCCGCCG
bPAC-H266W-qcF	CTGAAGATGGACTGGACCCTGCTGG
bPAC-H266W-qcR	CAGGGTCCAGTCCATCTTCAGGCTGCTG
bPAC-T267Y-qcF	TGAAGATGGACCACTACCTGCTGGG
bPAC-T267Y-qcR	GCAGGTAGTGGTCCATCTTCAGGCTGCT
EuPAC α -Sal5F	ACGCGTCGACATGTACATCCTTGTTTGGAAAGA
EuPAC α -XbStop3R	CTAGTCTAGACTATTAATGTTTCATATTTGTGCGAACCCCT
EuPAC β -Sal5F	ACGCGTCGACATGTACATTCTTGCTGGAAGAAG
EuPAC β -XbStop3R	CTAGTCTAGACTATCAGCGGACTTGGATGCTGCGC
YFP-Sal5F	ACGCGTCGACATGGTGAGCAAGGGCGAGGAG
EuPAC α -BgKz5F	GAAGATCTGCCACCATGTACATCCTTGTTTGGAAAGA
EuPAC α -Sal3R	ACGCGTCGACATGTTTCATATTTGTGCGAACCCCT
EuPAC β -910F	CCGGGCCATGCTGTGCAA
EuPAC α -910F	CGGTTCGAGCTTTGCTGTG
ArcB-Xh5F	CCGCTCGAGATGAAGCAGATCAGACTGCT
ArcB-Hd3R	CCCAAGCTTACAGCTGGATCTGGGTTTCCCT
ArcB-Kp5F	CGGGGTACCATGAAGCAGATCAGACTGCT
YFP-Kp3R	CGGGGTACCCTTGACAGCTCGTCCATGCCGAGA
CD8-BH5F	CGGGATCCGCCACCATGGCCTCACCGTTGAC
CD8-Xh3R	GCCGCTCGAGGGGGCCTCCGCCTCCGGA
bPAC-Kp5F	GGGGTACCAAGATGAAGCGGCTGGTGTAC
YFP-Xb3R	GCTCTAGATTACTTGTACAGCTCGTCCATG
YFP-MkBh5F	CGGGATCCAAGGTGAGCAAGGGCGAGGA
bPAC-BH5F	CGGGATCCGCCACCATGATGAAGCGGCTGGTGTAC
bPAC-XhHd3R	GCCCAAGCTTACTCGAGCAGGTCCTCCTCCGAGATCA
bPAC-Hd3R	GCCCAAGCTTACAGGTCCTCCTCCGAGATCA
bPAC-Lyn11+11-Nc5F	CATGCCATGGGATGTATAAAATCAAAGGGAAAGACAGC GCGGGAGCAGGAGTGCAGGTGGAACAGGCCTAAGCG GCTGGTGTACATCA
bPAC-NoMyc-RealEnd- SpHd3R	GCCCAAGCTTAACTAGTCTACTTGTGTTTTCCAGGGTCT
YFP-Lyn11-MkNc5F	CATGCCATGGGCTGTATTAAGTCCAAAGGGAAAGATTCTG CCAAGGTGAGCAAGGGCGAGGAGCT
bPAC-Lyn11-MkNc5F	CATGCCATGGGCTGTATTAAGTCCAAAGGGAAAGATTCTG CCAAGATGAAGCGGCTGGTG
BeCyClOP-BH-E-5F:	CGGGATCCGCCACCATGTTTTGCTATGAAAATGAAGTTAA GGACAAGGACAACAAC

BeCylOP-425-NcoI-3R	CATGCCATGGAACTTCATTTTCATAGCAAAGAGGATGG CGTCGCAGTT
BeCyClOP-Xb-E-5F	CTAGTCTAGAATGTTTTGCTATGAAAATGAAGTTAAGGAC AAGGACAACAAC
BeCylOP-425-E-Hd- stop-3R	CCCAAGCTTAACTTCATTTTCATAGCAAAGAGGATGGC GTCGCAGTT
BHKz-2Xflag-MKbPAC	CGGGATCCGCCACCATGGATTACAAGGATGACGACGATAA GGATTACAAGGATGACGACGATAAGAAGATGAAGCGGCT GGTGTAC
BeCyclOp-QYDIW-qcF	CAGTACGACATCTGGGGCGACACCGTGAACA
BeCyclOp-QYDIW-qcR	CCAGATGTCGTA CTGAGGGTTCAGGTCGCC
CaCyclOp-KpNoATG5F	CGGGGTACCGATAAGGATAACAATCTCCGTGGA
CaCyclOp425-Xh3R	CCGCTCGAGGATGGCATCACAGTT
CaCyclOp-Xh5F	GCCGCTCGAGAAGAAGGATAAGGATAACAATCTCCGT
CaCyclOp-Hd3R	GCCCAAGCTTACTACTTTCGGGCTGTGACCCA
CaCyclOp-BhKzATG5F	CGGGATCCGCCACCATGAAGGATAAGGATAACAATCTCC GT
CaCyclOp-Xh3R	GCCGCTCGAGCTTTCGGGCTGTGACCCA
CaCyclOp-Xh5F	GCCGCTCGAGAAGAAGGATAAGGATAACAATCTCCGT
CaCyclOp-Hd3R	GCCCAAGCTTACTACTTTCGGGCTGTGACCCA
CaCyclOp-1400SpeR	ATCTTTTGTACTAGTTCGCGACGAGATCACTGT
CaCyclOp-1400SpeF	TCGCGAACTAGTACAAAAGATATGATGGCCACA
CaCyclOp-BhKzATG5F	CGGGATCCGCCACCATGAAGGATAAGGATAACAATCTCCG T
CaCyclOp-Xh3R	GCCGCTCGAGCTTTCGGGCTGTGACCCA
vfChrimson-29-SalBh5F	ACGCGTCGACGGATCCATGGGCTGTGGAGGAATGA
vfChrimson-34-Bh5F	CGGGATCCATGACACCTACAGGCGAGTG
vfChrimson-XhHd3R	CCCAAGCTTATCACTCGAGCACTGTGTCTCGTCCTCCTC CTCCACGA
Chrimson-Xh3R	CCGCTCGAGCACGGTGTCT
Chrimson-XhHd 3R	CCCAAGCTTATCACTCGAGCACGGTGTCT
CsChrimson-Bg5F	CAGAAGATCTCTGGTCGCCGCTTCTTGGCT
ChrimsonHS-S169A-qcF	CGAGTGGCTGCTGGCCTGTCCCCTG
ChrimsonHS-S169A-qcR	GGCCAGCAGCCACTCGAAGTACCGC

6.2 Abbreviation

AA	amino acid
AC	adenylyl cyclase
AP	action potential
Arch	archaerhodopsin-3
ArcB	Aerobic respiration control sensor histidine protein kinase
ATP	adenosine 5'-triphosphate
ATR	all-trans retinal
BAPTA	1,2-bis(o-aminophenoxy)ethane-N,N,N',N'-tetraacetic acid
BiFC	Bimolecular Fluorescence Complementation
BLUF	blue light receptor using flavin
Bmpr	bone morphogenetic protein receptor type-1A
BR	bacteriorhodopsin
BSA	bovine serum albumin
CACC	calcium-activated chloride channel
cAMP	cyclic adenosine monophosphate
CatCh	calcium translocating Channelrhodopsin
CD8	Cluster of differentiation 8
CFTR	cystic fibrosis transmembrane conductance regulator
cGMP	cyclic guanosine monophosphate
ChR	channelrhodopsin
ChloC	chloride conducting ChR
ChRger	ChR Gaussian process-engineered recombinant opsin
CNG channel	Cyclic nucleotide-gated ion channel
cRNA	complementary RNA
cryo-EM	cryogenic electron microscopy
CyclOp	Cyclase Opsin
2c-CyclOp	Two-component cyclase opsins
DC pair	D156-C128 pair

dNTP	desoxynucleoside triphosphate
DTT	dithiothreitol
E	endoplasmic reticulum export signal
ER	endoplasmic reticulum
EST	expressed sequence tags
FTIR	Fourier-transform infrared
GC	guanylyl cyclase
Gly	glycophorin-A isoform 1
HR	halorhodopsin
I_{late}	late current
I_p or I_{peak}	peak current
I_s	stationary current
LB	lysogeny broth
LED	light emitting diode
LSM	laser scanning microscope
L/D	light activity/dark activity
NMG	N-Methyl-(D)-Glucamine
RNA	ribonucleic acid
RNase	ribonuclease
PAC	photoactivated adenylyl cyclase
PDE	phosphodiesterase
PCR	polymerase chain reaction
RhAC	rhodopsin-adenylyl cyclase
RhGC	rhodopsin-guanylyl cyclase
RhoPDE	rhodopsin phosphodiesterase
T	trafficking signal
TEVC	two-electrode voltage-clamp
TM	transmembrane
Δt	time delay

V_m	membrane potential
V_r	reversal voltage/potential
wt	wild-type
YFP	yellow fluorescent protein

Acknowledgement

First I would like to thank my supervisor Prof. Dr. Georg Nagel. Georg provides me great opportunities to participate in a variety of interesting projects. I am especially grateful for the stimulating environment he creates. He gives me freedom to explore the projects that interest me and the opportunities to argue with him. His great supervision, discussion and support shaped this thesis. I am thankful for my thesis committee: Prof. Dr. Tobias Langenhan and Prof. Dr. Robert J. Kittel for their kind supports and helpful suggestions on my thesis projects.

Thanks to Dr. Shiqiang Gao for his substantial help and instructions. Shiqiang gives tremendous help in designing experiments, analyzing data and writing manuscripts during my whole PhD study. Outside of the lab, He also offers various helps in my life in Würzburg.

My thanks also go to our collaborators: Dr. Knut Kirmse and Dr. Chuanqiang Zhang in Jena, Dr. Christine Gee and Oana Constantin in Hamburg, as well as Prof. Dr. Peter Hegemann and Dr. Ulrike Scheib in Berlin.

I would also like to extend my thanks to my colleagues, especially the members of the Nagel group, Dr. Yuehui Tian, Jing Yu-Strzelczyk, Dr. Xiaodong Duan, Dr. Sebastian Beck, Ruijing Tang, Yang Zhou, Maximilian Pitsch, Eike Jöst, Elfriede Reisberg and Julia Köber for creating the enjoyable working atmosphere and offering help whenever needed. Thanks to all of my friends for their help and support in my life.

Finally and most importantly, I would like to thank my parents, Qing'en Yang and Shuling Chen, for their unconditional love, support, tolerance and confidence in me.

Thanks for the funding support form DFG TR166/A3 and DAAD.

Affidavit

I hereby declare that my thesis entitled: **“Characterization and engineering of photoreceptors with improved properties for optogenetic application”** is the result of my own work. I did not receive any help or support from commercial consultants. All sources and / or materials applied are listed and specified in the thesis.

Furthermore I verify that the thesis has not been submitted as part of another examination process neither in identical nor in similar form.

Besides I declare that if I do not hold the copyright for figures and paragraphs, I obtained it from the rights holder and that paragraphs and figures have been marked according to law or for figures taken from the internet the hyperlink has been added accordingly.

Würzburg, den _____

Signature PhD-student

Curriculum Vitae

Personal information

Name: Shang Yang

Gender: Male

Nationality: Chinese

Email: shang.yang@uni-wuerzburg.de and yangsh1129@163.com

Current address: Martin-Luther-Str. 1, 97072 Würzburg, Germany

Education and training

2007.09-2011.07: Bachelor study in China Agricultural University, Beijing, China

2011.09-2014.07: Master study in Institute of Biophysics, Chinese Academy of Sciences (Supervisor: Prof. Chih-Chen Wang), Beijing, China

2014.09-2015.08: Research Assistant in Tsinghua University (Supervisor: Prof. Xu Tan), Beijing, China

2015.09-Now: PhD study in University of Würzburg (Supervisor: Prof. Georg Nagel), Würzburg, Germany

Funding support and fellowship

2015-2019: DFG funded PhD position (TRR166/A03 to G.N.)

2019-2020: DAAD fellowship

Publications

1. **Yang S**, Wang X, Cui L, Ding X, Niu L, Yang F, Wang C, Wang CC, Lou J. Compact conformations of human protein disulfide isomerase. *PLoS ONE*. 2014 Aug 1;9(8):e103472.
2. Lin Z*, Li S*, Feng C*, **Yang S**, Wang H, Ma D, Zhang J, Gou M, Bu D, Zhang T, Kong X, Wang X, Sarig O, Ren Y, Dai L, Liu H, Zhang J, Li F, Hu Y, Padalon-Brauch G, Vodo D, Zhou F, Chen T, Deng H, Sprecher E, Yang Y#, Tan X#. Stabilizing mutations of KLHL24 ubiquitin ligase cause loss of keratin 14 and human skin fragility. *Nature Genetics* (2016) 48(12): 1508-1516
3. Tian Y, Gao S, **Yang S**, Nagel G. (2018) A novel rhodopsin phosphodiesterase from *Salpingoeca rosetta* shows light-enhanced substrate affinity. *Biochem J*. 475(6):1121-1128. doi: 10.1042/BCJ20180010.
4. Scheib U, Broser M, Constantin O M, **Yang S**, Gao S, Mukherjee S, Stehfest K, Nagel G, Gee C E, Hegemann P. (2018) Rhodopsin-cyclases for photocontrol of cGMP/cAMP and 2.3 Å structure of the adenylyl cyclase domain. *Nature Communications* 9(1):2046. doi: 10.1038/s41467-018-04428-w.
5. **Shang Yang**, Oana M. Constantin, Shiqiang Gao, Thomas G. Oertner, Christine E. Gee, Georg Nagel. Engineering of bacterial photoactivated adenylyl cyclases for optogenetic cAMP manipulation. (Manuscript in preparation)
6. Zhang, C.*, **Yang, S.***, Flossmann, T.* Gao. S., Witte. O., Nagel, G., Holthoff. K., Kirmse. K#. Optimized photo-stimulation of halorhodopsin for long-term neuronal inhibition. *BMC Biol* 17, 95 (2019). doi:10.1186/s12915-019-0717-6 (co-first author)

Conferences and presentations

1. The 4th Symposium of Chinese Protein Society. Hefei, China. Oct. 2013. (Poster presentations: Molecular dynamics study of human protein disulfide isomerase).
2. OPTOGEN 2016: 3rd International Workshop on Technologies for Optogenetics. Freiberg, Germany. Dec. 2016. (Poster presentation: Engineering and characterization of photoactivated adenylyl cyclases).
3. Gordon research seminar: Spectroscopy, Signaling and Optogenetics: Past, Present and Future. Lucca, Italy. Mar. 2018. (Poster presentation: The rhodopsin phosphodiesterase from *Salpingoeca rosetta* is light-activated via a light-sensitive Michaelis constant).
4. Gordon research conference: How Light Controls Behavior of Molecules, Cells, Organisms and Ecosystems over Time Scales of Femtoseconds to Eons. Lucca, Italy. Mar. 2018. (Poster Presentation: The rhodopsin phosphodiesterase from *Salpingoeca rosetta* is light-activated via a light-sensitive Michaelis constant).
5. EMBO/EMBL symposium: Probing Neural Dynamics with Behavioural Genetics. Heidelberg, Germany, Apr. 2019. (Poster presentation: Engineering of bacterial photoactivated adenylyl cyclases for optogenetic cAMP manipulation).
6. Receptorlight symposium 2019. Jena, Germany, Jun. 2019. (Poster presentation: Improved optogenetics tools for biological research. & Flash talk: Engineering of bacterial photoactivated adenylyl cyclases for optogenetic cAMP manipulation).